

POLITECNICO DI TORINO

**MASTER's Degree in NANOTECHNOLOGIES FOR
ICTs**



MASTER's Degree Thesis

**SIMULATION OF ULTRAFAST
FIELD-EMISSION PLASMONIC
NANOANTENNAS FOR PHz
PROCESSING OF OPTICAL
WAVEFORMS**

Supervisors

Prof. FABRIZIO GIORGIS

Dr. PHILLIP D. KEATHLEY

Candidate

DARIO CATTOZZO MOR

OCTOBER 23, 2020

Summary

This thesis project is focused on studying and simulating petahertz-electronic devices for optical field waveform detection. In particular, it studies the behaviour of ultrafast nanoscale plasmonic electron emitting antennas in free-space and it focuses on the design and optimization of coupling to waveguide modes for potential operation within an integrated photonics platform. The main aim of the devices is to detect and process incident ultrafast optical waveforms.

The project is divided in two main parts, which analyse two different applications of the antennas. The first studied device is optimized for low-energy, near-infrared waveforms field sampling, which is used for characterization of optical waveforms. The second one is a carrier-envelope phase (CEP) detector. The CEP is a feature of optical pulses or waveforms and is the offset between the peak of the electric field carrier wave and the peak of the pulse envelope.

These devices are useful for several reasons. As a first feature, they help improve the understanding of ultrafast light-matter interactions in solids and are important tools for the time-domain attosecond metrology. Concerning the field sampler, it can lead to important applications such as precise attosecond metrology, studies on strong-field light-matter interaction and time-domain spectroscopy of molecular fingerprints. The devices studied in this work are on-chip and can study low energy, near-infrared arbitrary pulses in ambient conditions. Concerning the CEP detector, CEP defines the exact optical waveform of a pulse and is then fundamental for strong-field light-matter interactions. Furthermore, it is important for frequency-comb optical sources, optical frequency synthesis and attosecond pulse generation. As a future application, ultrafast information processing can be enabled, thanks to lightwave-based petahertz electronic. The device studied in this work is a compact and integrable solid state detector working in ambient conditions.

The electron emitters consist of a series of electrically interconnected 20-nm-thick Au antennas, shaped as isosceles nanotriangles, that can be arranged in two different configurations, one for the field sampler and one for the CEP detector. The field

sampler has the sharpest tip of the nanotriangle facing a perpendicular collector nanowire, at a few tens of nm distance. The CEP detector has the sharpest tip of the nanotriangles facing another nanotriangle.

In both the field sampler and the CEP detector configurations, the optical waveform that is to be analysed is delivered to the devices as a free-space wave. Since pulse sources are going towards being completely integrated, a need for waveguide-integrated CEP detectors and field samplers for potential operation within integrated photonics platforms arose. In the last chapter of the thesis the antennas will be integrated on top of a waveguide and coupled to waveguide modes.

The device working principle is as follows: plasmonic and geometric enhancement effects convey electric field at the sharpest tip of the nanotriangles, when the material is illuminated. The enhanced field bends the potential barrier at the tip surface and drive optical-field photoemission toward the collector wire or triangle. The emission can be approximated by a quasi-static tunnelling rate and is then calculated by a quasi-static Fowler-Nordheim (FN) emission model. This process helps study the incident field waveform.

In the first Chapter, the device electromagnetic field response is simulated in the frequency domain. This is important in order to quantitatively estimate the field behavior at the antennas tip. Indeed, in the field sampling process, it is fundamental to control the field value at the antennas tip, in order to study the possible emitted photocurrent. In particular, the excitation of plasmonic resonances is analysed through power transmission and extinction studies and the field enhancement at the device tip is sampled as a function of frequency.

Throughout the second Chapter, the nanoantennas are placed on top of a rectangular waveguide core and the device is studied with both a frequency-domain and a time-domain analysis. In particular, the field distribution in the device as a function of frequency is analysed and particularly interesting is the field enhancement at the tips of the antennas. The field distribution gives information about the behaviour of the device, whereas the field enhancement at the tips of the antennas is important for understanding the evolution of an optical waveform at the antennas tips. Indeed, different frequency components of the waveform will be enhanced according to field enhancement at tips. A time-domain approach studies this transformation of pulses at the antennas and it results in the evaluation of CEP at each antenna. The device is then studied for its losses and power transmission, in order to better engineer the design and signal collection. As a last step, the electron emission from the illuminated antennas is evaluated, according to Fowler-Nordheim tunnelling theory.

Acknowledgements

This thesis project was carried out at Massachusetts Institute of Technology (MIT), at the Research Laboratory of Electronics (RLE) in the Quantum Nanostructures and Nanofabrication group (QNN), under the supervision of Research Scientist and Group Leader Phillip D. Keathley, Prof. Karl K. Berggren, Research Assistant Yujia Yang, Felix Ritzkowsky¹ and Neetesh Kumar¹. K. K. Berggren is the QNN group leader. P. D. Keathley, together with the group, suggested the project and thoroughly assisted the author of the thesis. Y. Yang provided the author with technical simulation advice and theoretical counseling. F. Ritzkowsky and N. Kumar assisted in the development of the project and gave guidance on important project goals. N. Kumar provided technical details on the considered optical sources.

¹Deutsches Elektronen Synchrotron (DESY) & Center for Free-Electron Laser Science, Notkestraße 85, 22607 Hamburg, Germany.

Table of Contents

List of Tables	IX
List of Figures	XI
Acronyms	XXII
1 Introduction and theory	1
1.1 Introduction	1
1.2 Background and theory	3
1.2.1 Light pulse theory	3
1.2.2 Plasmonic nanoantennas and photoemission theory	5
1.2.3 Waveguide theoretical analysis	8
2 Ultrafast electromagnetic pulse interactions with rectified nanoantennas for optical-field sampling	10
2.1 Model setup	13
2.2 Results	15
2.2.1 Initial geometry	15
2.2.2 Geometry adjustments	23
2.2.3 Numerical/experimental results comparison	35
2.3 Conclusions	40
3 Waveguide-integrated bow-tie nanonantennas for CEP detection	47
3.1 Waveguide numerical simulation vs. analytical method	49
3.1.1 Materials, geometry and model setup	49
3.1.2 Results	50
3.2 Waveguide-integrated bow-tie nanoantennas	53
3.2.1 Device structure and simulation setup	56
3.2.2 Type of analyses	57
3.3 Simulation results	57
3.3.1 Frequency-domain analysis	57

3.3.2	Time-domain analysis	71
3.3.3	Power transmission and losses	77
3.3.4	Fowler-Nordheim emission	81
3.4	Conclusions	94
4	Conclusions	98
4.1	Summary and discussion	98
4.2	Future work	100
A	Scripts	102
	Bibliography	106

List of Tables

2.1	Features dimensions for the 3 considered geometries. The listed values are obtained by measuring 3 devices for each geometry in the SEM images and averaging them. The triangle heights and bases are reported without taking into account the rounding of the tips, so the actual dimensions will be shorter in the simulated geometry.	14
2.2	The data in the table corresponds to the wavelengths at which the peaks occur in the extinction plots of the fabricated devices, as in Figure 2.30."	23
2.3	Features dimensions for the 3 considered geometries. The listed values are obtained by a single measure on one device for each geometry in the SEM images. The triangle heights and bases are reported without taking into account the rounding of the tips, so the actual dimensions will be shorter in the simulated geometry. The simulation domain dimensions are forcefully set to 800nm × 400 nm, because are the ones that were set in the fabrication process.	28
2.4	The data in the table corresponds to the wavelengths at which the peaks occur in the extinction plots in Figures 2.31 and 2.30.	28
2.5	The data in the table corresponds to the wavelengths at which the peaks occur in the extinction plots for all of the considered geometries, for different values of the parameter " <i>wire_x</i> ".	30
2.6	The data in the table corresponds to the wavelengths at which the peaks occur in the field enhancement plots for all of the considered geometries, for different values of the parameter " <i>wire_x</i> ".	31
2.7	The data in the table corresponds to the wavelengths at which the peaks occur in the extinction plots for the 280 nm geometry as listed in Table 2.3, for different values of the parameter " <i>wire_x</i> " and of the height of the triangle.	31
2.8	The data in the table corresponds to the wavelengths at which the peaks occur in the extinction plots for all of the considered geometries, for different values of the parameter " <i>wire_x</i> ".	35

2.9	The data in the table corresponds to the wavelengths at which the peaks occur in the field enhancement plots for all of the considered geometries, for different values of the parameter " <i>wire_x</i> ".	36
2.10	Final considered geometries dimensions. The reported data corresponds to corrections to the values in Table 2.1.	36
3.1	Features of the input field waveform at the waveguide port. The considered device has 3 antennas and antennas spacing $4.5 \mu\text{m}$	81
3.2	The quantities in the table are: CEP-sensitive charge density from left-side nanotriangles $ J_{1,L} $, mean charge density from left-side nanotriangles $J_{0,L}$, CEP-sensitive charge density from right-side nanotriangles $ J_{1,R} $, mean charge density from right-side nanotriangles $J_{0,R}$, CEP sensitivity for the left-side nanotriangle $ J_{1,L} /J_{0,L}$, CEP sensitivity for the right-side nanotriangle $ J_{1,R} /J_{0,R}$, total CEP-sensitive current density $ J_{cep} $ and residual average total current density $J_{0,detected}$. These quantities are studied for all of the considered antennas.	87
3.3	Features of the incident field waveform for the fabricated devices reported in ref. [23].	90
3.4	See Table 3.2 for the listed quantities definitions. These values are given by the free-space bow-tie nanoantennas.	91
3.5	Total emitted CEP-sensitive photocurrent per each bow-tie antenna of the waveguide-integrated device.	92

List of Figures

1.1	Representation of the rectified nanoantennas, as in ref. [24]. No scale is present but the triangle height is ~ 280 nm.	3
1.2	Representation of the bow-tie nanoantennas, as in ref. [23]. No scale is present but the triangle height is 200 nm.	3
1.3	(top): ultrafast train pulse, as a function of time; $\Delta\phi_{\text{CE}}$ is the carrier-envelope phase (CEP) and f_{rep} is the repetition rate of the pulse train; (bottom): pulse train spectrum; f_0 is the carrier-envelope offset frequency (also f_{CEO}). Image from ref. [25].	4
2.1	SEM image of the rectified nanoantennas, fabricated by the QNN group, ref. [24]. No scale is present but the triangle height is ~ 280 nm	11
2.2	3D COMSOL Multiphysics model for the rectified nanoantennas. The array disposition of the antennas is obtained in the simulation by setting the lateral boundary conditions as "periodic". The 20 nm Au nanostructures are represented in yellow, the 2 nm Cr adhesion layer is black and the BK7 substrate is glass-like transparent. The device is immersed in air.	12
2.3	Representation of field sampling process with rectified nanoantennas, as in ref. [24]. No scale is present but the triangle height is ~ 280 nm.	12
2.4	SEM image of the rectified nanoantennas, with nanotriangles with height ~ 200 nm, fabricated by the QNN group, ref. [24].	13
2.5	SEM image of the rectified nanoantennas, with nanotriangles with height ~ 240 nm, fabricated by the QNN group, ref. [24].	13
2.6	SEM image of the rectified nanoantennas, with nanotriangles with height ~ 280 nm, fabricated by the QNN group, ref. [24].	14
2.7	3D COMSOL Multiphysics model for the rectified nanoantennas. No scale is present but the triangle height is ~ 280 nm. In blue is highlighted the tip surface over which the field average operation is carried out	16

2.8	3D COMSOL Multiphysics model for the rectified nanoantennas. No scale is present but the triangle height is ~ 280 nm. In blue is highlighted the tip surface over which the field average operation is carried out	16
2.9	Extinction plot for the 240 nm geometry, as listed in Table 2.1. . . .	16
2.10	Power transmission plot for the 240 nm geometry, as listed in Table 2.1.	17
2.11	Power transmission T_0 calculated without the nanoantenna structure but still with the BK7 substrate.	17
2.12	Field distribution at the wavelength corresponding to the tip-mode in the extinction plot for the 240 nm geometry, as listed in Table 2.1.	18
2.13	Field distribution at the wavelength corresponding to the wire-mode in the extinction plot for the 240 nm geometry, as listed in Table 2.1.	18
2.14	Field enhancement plot for the 240 nm geometry, as listed in Table 2.1.	18
2.15	Field distribution at the wavelength corresponding to the main peak in the field enhancement plot for the 240 nm geometry, as listed in Table 2.1.	19
2.16	Field distribution at the wavelength corresponding to the secondary peak in the field enhancement plot for the 240 nm geometry, as listed in Table 2.1.	19
2.17	Extinction plot for the 280 nm geometry, as listed in Table 2.1. . .	20
2.18	Power transmission plot for the 280 nm geometry, as listed in Table 2.1.	21
2.19	Field distribution at the wavelength corresponding to the tip-mode in the extinction plot for the 280 nm geometry, as listed in Table 2.1.	21
2.20	Field distribution at the wavelength corresponding to the wire-mode in the extinction plot for the 280 nm geometry, as listed in Table 2.1.	21
2.21	Field enhancement plot for the 280 nm geometry, as listed in Table 2.1.	22
2.22	Field distribution at the wavelength corresponding to the main peak in the field enhancement plot for the 280 nm geometry, as listed in Table 2.1.	22
2.23	Field distribution at the wavelength corresponding to the secondary peak in the field enhancement plot for the 280 nm geometry, as listed in Table 2.1.	22
2.24	Extinction plot for the 200 nm geometry, as listed in Table 2.1. . .	23
2.25	Power transmission plot for the 200 nm geometry, as listed in Table 2.1.	24
2.26	Field distribution at the wavelength corresponding to the tip-mode in the extinction plot for the 200 nm geometry, as listed in Table 2.1.	24

2.27	Field distribution at the wavelength corresponding to the wire-mode in the extinction plot for the 200 nm geometry, as listed in Table 2.1.	24
2.28	Field enhancement plot for the 200 nm geometry, as listed in Table 2.1.	25
2.29	Field distribution at the wavelength corresponding to the main peak in the field enhancement plot for the 200 nm geometry, as listed in Table 2.1.	26
2.30	Experimental extinction plot for the devices fabricated by the QNN group and that are shown in the SEM images in Figures 2.4, 2.5 and 2.6.	27
2.31	Extinction plots for all the considered geometries, as listed in Table 2.3. The yellow curve corresponds to the 280nm geometry, the red one to the 240 nm geometry and the blue one to the 200 nm geometry.	29
2.32	SEM image of the bow-tie nanoantennas, fabricated by the QNN Group, as in ref. [23]. In particular, the image shows the bow-tie antennas before and after being illuminated, in order to highlight the presence of laser-induced reshaping.	32
2.33	An example of how the process of tip shrinking is replicated in the simulation geometries. In particular, this figure shows a -20 nm decrease in the tip length for a 280 nm geometry.	33
2.34	Extinction plot for the 200 nm geometry, as listed in Table 2.1, for different values of tip shrinking.	33
2.35	Field enhancement plot for the 200 nm geometry, as listed in Table 2.1, for different values of tip shrinking.	33
2.36	Extinction plot for the 240 nm geometry, as listed in Table 2.1, for different values of tip shrinking.	34
2.37	Field enhancement plot for the 240 nm geometry, as listed in Table 2.1, for different values of tip shrinking.	34
2.38	Extinction plot for the 280 nm geometry, as listed in Table 2.1, for different values of tip shrinking.	34
2.39	Field enhancement plot for the 280 nm geometry, as listed in Table 2.1, for different values of tip shrinking.	34
2.40	Extinction plot for the 240 nm geometry, as listed in Table 2.10.	37
2.41	Field distribution at the wavelength corresponding to the tip-mode in the extinction plot for the 240 nm geometry, as listed in Table 2.10.	37
2.42	Field distribution at the wavelength corresponding to the wire-mode in the extinction plot for the 240 nm geometry, as listed in Table 2.10.	37
2.43	Field enhancement plot for the 240 nm geometry, as listed in Table 2.10.	38

2.44	Field distribution at the wavelength corresponding to the main peak in the field enhancement plot for the 240 nm geometry, as listed in Table 2.10.	38
2.45	Field distribution at the wavelength corresponding to the secondary peak in the field enhancement plot for the 240 nm geometry, as listed in Table 2.10.	38
2.46	Extinction plot for the 280 nm geometry, as listed in Table 2.10.	39
2.47	Field distribution at the wavelength corresponding to the tip-mode in the extinction plot for the 280 nm geometry, as listed in Table 2.10.	39
2.48	Field distribution at the wavelength corresponding to the wire-mode in the extinction plot for the 280 nm geometry, as listed in Table 2.10.	39
2.49	Field enhancement plot for the 280 nm geometry, as listed in Table 2.10.	40
2.50	Field distribution at the wavelength corresponding to the secondary peak in the field enhancement plot for the 280 nm geometry, as listed in Table 2.10.	41
2.51	Extinction plot for the 200 nm geometry, as listed in Table 2.10.	42
2.52	Field distribution at the wavelength corresponding to the tip-mode in the extinction plot for the 200 nm geometry, as listed in Table 2.10.	42
2.53	Field distribution at the wavelength corresponding to the wire-mode in the extinction plot for the 200 nm geometry, as listed in Table 2.10.	43
2.54	Field distribution at the wavelength corresponding to the wire-mode in the extinction plot for the 200 nm geometry, as listed in Table 2.10.	43
2.55	Field enhancement plot for the 200 nm geometry, as listed in Table 2.10.	43
2.56	Field distribution at the wavelength corresponding to the main peak in the field enhancement plot for the 200 nm geometry, as listed in Table 2.10.	44
2.57	Experimental extinction plot for the devices fabricated by the QNN group and that are shown in the SEM images in Figures 2.4, 2.5 and 2.6. The vertical coloured lines serve the purpose of indicating the peaks wavelengths.	45
2.58	Extinction plots for all the considered geometries, as listed in Table 2.10.	46

3.1	Bow-tie antennas configuration. No scale is present but the triangle height is 200 nm. The 20 nm Au nanostructures are represented in yellow, the 2 nm Cr adhesion layer is black and the SiN waveguide core is light blue / white. The waveguide SiO ₂ cladding is not represented in this figure.	48
3.2	Dispersion relation. Comparison between numerical and analytical results for a rectangular waveguide.	50
3.3	Phase velocity. Comparison between numerical and analytical results for a rectangular waveguide.	51
3.4	Group velocity. Comparison between numerical and analytical results for a rectangular waveguide.	51
3.5	Effective refractive index. Comparison between numerical and analytical results for a rectangular waveguide.	52
3.6	CEP shift per μm travelled in the waveguide. Comparison between numerical and analytical results for a rectangular waveguide.	52
3.7	Distance in the waveguide after which CEP shifts of 2π . Comparison between numerical and analytical results for a rectangular waveguide.	52
3.8	Dispersion relation. Comparison between numerical and analytical results for a slab waveguide.	53
3.9	Phase velocity. Comparison between numerical and analytical results for a slab waveguide.	53
3.10	Group velocity. Comparison between numerical and analytical results for a slab waveguide.	54
3.11	Effective refractive index. Comparison between numerical and analytical results for a slab waveguide.	54
3.12	CEP shift per μm travelled in the waveguide. Comparison between numerical and analytical results for a slab waveguide.	54
3.13	Distance in the waveguide after which CEP shifts of 2π . Comparison between numerical and analytical results for a slab waveguide.	54
3.14	3D COMSOL Multiphysics model for the waveguide-integrated bow-tie nanoantennas. No scale is present but the waveguide core height is 800 nm. The 20 nm Au nanostructures are represented in yellow, the 2 nm Cr adhesion layer is black and the SiN waveguide core is light blue / white. The waveguide SiO ₂ cladding is not represented in this figure.	55
3.15	Top-view of the simulated model for the waveguide-integrated bow-tie nanoantennas. No scale is present but the triangles height is 200 nm.	55

3.16	Bow-tie antennas configuration. No scale is present but the triangle height is 200 nm. The 20 nm Au nanostructures are represented in yellow, the 2 nm Cr adhesion layer is black and the SiN waveguide core is light blue / white. The waveguide SiO ₂ cladding is not represented in this figure.	56
3.17	Average CEP difference between one antenna and the next as a function of antennas spacing.	58
3.18	Average CEP difference between one antenna and the next as a function of antennas spacing.	59
3.19	Average CEP difference between one antenna and the next as a function of antennas spacing.	59
3.20	Field distribution in the core of the waveguide, for $\lambda = 1500$ nm, studied along a XY cut-plane, with coordinate $z = 0$, which is the middle of the core height (reference to axis orientation in Figures 3.14 and 3.16). The considered device has 3 antennas and antennas spacing $4.5 \mu\text{m}$	59
3.21	Field distribution in the core of the waveguide, for $\lambda = 1500$ nm, studied along a XY cut-plane, with coordinate z such that it is at $3/4$ of the core height (reference to axis orientation in Figures 3.14 and 3.16). The considered device has 3 antennas and antennas spacing $4.5 \mu\text{m}$	60
3.22	Field distribution at the antennas, for $\lambda = 1500$ nm, studied along a XY cut-plane, with coordinate z such that it is at the center of the gold layer. The considered device has 3 antennas and antennas spacing $4.5 \mu\text{m}$	60
3.23	Field distribution at the antennas, for $\lambda = 1500$ nm, studied along a XY cut-plane, with coordinate z such that it is at the center of the gold layer.	61
3.24	Field distribution at the antennas, for $\lambda = 1500$ nm, studied along a XY cut-plane, with coordinate z such that it is at the center of the gold layer. Colour scale is saturated, in order to enhance and analyze the behaviour of the field in the region surrounding the antennas. The considered device has 3 antennas and antennas spacing $4.5 \mu\text{m}$. The inset on the left shows the particular of the field oscillation around the connection wires. The inset on the right shows the concentration of field at the wires.	61
3.25	Field distribution at a waveguide section, at the input port, for $\lambda = 1500$ nm.	62
3.26	Field distribution at a waveguide section, at ~ 600 nm from the input port, for $\lambda = 1500$ nm.	62
3.27	62

3.28	Field distribution at a waveguide section, at $\sim 1.2 \mu\text{m}$ from the input port, for $\lambda = 1500 \text{ nm}$	63
3.29	Field distribution at a waveguide section, at $\sim 3.6 \mu\text{m}$ from the input port, for $\lambda = 1500 \text{ nm}$	63
3.30	63
3.31	Field distribution at a waveguide section, $\sim 300 \text{ nm}$ before the first antenna, for $\lambda = 1500 \text{ nm}$	63
3.32	Field distribution at a waveguide section, at the first antenna, for $\lambda = 1500 \text{ nm}$. The color scale is saturated, in order to show the fact that some field is still confined in the center of the core. Indeed, the field at the antennas is $\sim 10\times$ the maximum colour scale value. . .	63
3.33	63
3.34	Top-view of the simulated model for the waveguide-integrated bow-tie nanoantennas, with no connection wires. No scale is present but the triangles height is 200 nm	64
3.35	Field distribution in the core of the waveguide, for $\lambda = 1500 \text{ nm}$, studied along a XY cut-plane, with coordinate $z = 0$, which is the middle of the core height (reference to axis orientation in Figures 3.14 and 3.16). The considered device has 3 antennas and antennas spacing $2 \mu\text{m}$	65
3.36	Field distribution at the antennas, for $\lambda = 1500 \text{ nm}$, studied along a XY cut-plane, with coordinate z such that it is at the center of the gold layer.. The considered device has 3 antennas and antennas spacing $2 \mu\text{m}$. Colour scale is saturated, in order to enhance and analyze the behaviour of the field in the region surrounding the antennas.	65
3.37	Field distribution at a waveguide section, at the first antenna, for $\lambda = 1500 \text{ nm}$. The color scale is saturated, in order to show the fact that some field is still confined in the center of the core. Indeed, the field at the antennas is $\sim 10\times$ the maximum colour scale value. . .	66
3.38	Top-view of the simulated model for the waveguide-integrated bow-tie nanoantennas, with no bow-tie antennas and only the connection wires. No scale is present but the waveguide width is $1 \mu\text{m}$	67
3.39	Field distribution at the gold layer, for $\lambda = 1500 \text{ nm}$, studied along a XY cut-plane, with coordinate z such that it is at the center of the gold layer. Colour scale is saturated.	67
3.40	Field distribution at a waveguide section, at the middle point of the waveguide, for $\lambda = 1500 \text{ nm}$	67

3.41	Waveguide section at the input port. In red is represented the parametric surface over which the field average operation is carried out in order to obtain the E_0 value. No scale is present but the waveguide core height is 800 nm.	68
3.42	Reference value E_0 at the waveguide input port as a function of wavelength λ	68
3.43	Field enhancement at the antennas tips as a function of wavelength λ , for the three bow-tie antennas along the waveguide. The considered device has 3 antennas and antennas spacing $4.5 \mu\text{m}$	69
3.44	Field enhancement at the antennas tips as a function of wavelength λ , for the first bow-tie antenna along the waveguide. The considered device has 3 antennas and antennas spacing $4.5 \mu\text{m}$	69
3.45	Field enhancement at the antennas tips as a function of wavelength λ , for the second bow-tie antenna along the waveguide. The considered device has 3 antennas and antennas spacing $4.5 \mu\text{m}$	70
3.46	Field enhancement at the antennas tips as a function of wavelength λ , for the third bow-tie antenna along the waveguide. The considered device has 3 antennas and antennas spacing $4.5 \mu\text{m}$	70
3.47	Field distribution in the core of the waveguide, for $\lambda = 1500 \text{ nm}$, studied along a XY cut-plane, with coordinate $z = 0$, which is the middle of the core height (reference to axis orientation in Figures 3.14 and 3.16). The considered device has 1 antenna and antennas spacing $2 \mu\text{m}$	71
3.48	Field enhancement at the antenna tips as a function of wavelength λ . The considered device has 1 antenna and antennas spacing $2 \mu\text{m}$	72
3.49	Field distribution in the core of the waveguide, for $\lambda = 1500 \text{ nm}$, studied along a XY cut-plane, with coordinate $z = 0$, which is the middle of the core height (reference to axis orientation in Figures 3.14 and 3.16). The considered device has 5 antennas and antennas spacing $2 \mu\text{m}$	72
3.50	Field enhancement at the antennas tips as a function of wavelength λ . The considered device has 5 antennas and antennas spacing $2 \mu\text{m}$	73
3.51	Field enhancement at the antenna tips as a function of antennas spacing, at $\lambda = 1475 \text{ nm}$. The considered device has 3 antennas.	73
3.52	Normalized incident pulse field as a function of time, at the input port of the waveguide. The considered device has 3 antennas and antennas spacing $4.5 \mu\text{m}$	74
3.53	Normalized enhanced pulse at the first antenna as a function of time. The considered device has 3 antennas and antennas spacing $4.5 \mu\text{m}$	74

3.54	Normalized enhanced pulse at the second antenna as a function of time. The considered device has 3 antennas and antennas spacing $4.5 \mu\text{m}$	74
3.55	Normalized enhanced pulse at the third antenna as a function of time. The considered device has 3 antennas and antennas spacing $4.5 \mu\text{m}$	74
3.56	Input pulse and enhanced pulses at the antennas. Arbitrary field units. The considered device has 3 antennas and antennas spacing $4.5 \mu\text{m}$	75
3.57	Normalized spectra of the studied pulses. The considered device has 3 antennas and antennas spacing $4.5 \mu\text{m}$	76
3.58	CEP value, calculated at the three considered antennas. The considered device has 3 antennas and antennas spacing $4.5 \mu\text{m}$	76
3.59	Input pulse and enhanced pulses at the antennas. Arbitrary field units. The considered device has 3 antennas and antennas spacing $2 \mu\text{m}$	77
3.60	CEP value, calculated at the three considered antennas. The considered device has 3 antennas and antennas spacing $2 \mu\text{m}$	78
3.61	S_{21}^2 parameter as a function of wavelength. The considered device has 3 antennas and antennas spacing $4.5 \mu\text{m}$	78
3.62	Power transmission at output port of the waveguide as a function of wavelength. In particular, the contribution of power crossing the core or the cladding of the waveguide is shown. The considered device has 3 antennas and antennas spacing $4.5 \mu\text{m}$	79
3.63	Total power losses as a function of wavelength. In particular, the contributions of power absorption at the metal nanostructures and in the waveguide material and power scattering at the antennas are shown. The considered device has 3 antennas and antennas spacing $4.5 \mu\text{m}$	80
3.64	Power transmission at output port as a function of number of antennas coupled to the waveguide, for $\lambda = 1500 \text{ nm}$. The considered devices have antennas spacing $2 \mu\text{m}$	81
3.65	Power losses from one antenna to the next along the waveguide, for $\lambda = 1500 \text{ nm}$. The considered devices have antennas spacing $2 \mu\text{m}$	81
3.66	Field waveform of the enhanced pulse at the first antenna and instantaneous emitted current density as a function of time. The CEP value for the input pulse is set to zero.	84
3.67	Emitted charge density as a function of CEP value of the input pulse, from the left and right tip of the bow-tie antennas.	85
3.68	Total emitted charge density as a function of CEP value of the input pulse.	86

3.69	CEP-sensitive photocurrent as a function of the pulse peak intensity. The images focuses on the so-called "vanishing points".	88
3.70	CEP-sensitive photocurrent density at the considered antennas, for different pulse peak field values.	89
3.71	Representation of the devices studied in ref. [23] and of the CEP value for an ultrashort pulse.	90
3.72	Field waveform of the enhanced pulse at the free-space bow-tie antennas and instantaneous emitted current density as a function of time. The CEP value for the input pulse is set to zero.	91
3.73	CEP-sensitive current density as a function of pulse duration.	93
3.74	CEP sensitivity as a function of pulse duration.	93
3.75	CEP-sensitive current density as a function of pulse peak field.	94
3.76	CEP sensitivity as a function of pulse peak field.	95

Acronyms

CEP

carrier-envelope phase

FE

field enhancement

FN

Fowler-Nordheim

Chapter 1

Introduction and theory

1.1 Introduction

This thesis project is focused on studying and simulating petahertz-electronic devices for optical field waveform detection. In particular, it studies the behaviour of ultrafast nanoscale plasmonic electron emitting antennas in free-space and it focuses on the design and optimization of coupling to waveguide modes for potential operation within an integrated photonics platform. The main aim of the device is to detect and process incident ultrafast optical waveforms.

The project is divided in two main parts, which analyse two different applications of the antennas. The first studied device is optimized for low-energy, near-infrared waveforms field sampling, which is used for characterization of optical waveforms. The second one is a carrier-envelope phase (CEP) detector. The CEP is a feature of optical pulses or waveforms that describes the offset between the peak of the electric field carrier wave and the peak of the pulse envelope.

These devices are useful for several reasons. As a first feature, they help improve the understanding of ultrafast light-matter interactions in solids and are important tools for the time-domain attosecond metrology. Concerning the field sampler, it can lead to important applications such as precise attosecond metrology, studies on strong-field light-matter interaction and time-domain spectroscopy of molecular fingerprints, see ref. [1] and [2]. Direct optical-field sampling in the time-domain has already been explored, ref. [3], [4], [5], [6] and [7], but these devices often require large pulse energies, bulky apparatuses and vacuum environments. The devices studied in this work are on-chip (so compact and integrated) and can study low energy, near-infrared arbitrary pulses in ambient conditions. Concerning the CEP detector, CEP defines the exact optical waveform of a pulse and is then

fundamental for strong-field light–matter interactions, since in this regime the interactions depend on the instantaneous electric field value rather than on the intensity envelope of the pulse. Furthermore, in frequency-comb optical sources, ref. [8], it is fundamental to stabilize the carrier-envelope offset frequency (f_{CEO}), that is the frequency at which the CEP changes from one generated peak to the next and it is important for applications like optical frequency synthesis, ref. [9] and [10] and attosecond pulse generation, ref. [11]. As a future application, precisely controlled CEP can lead to ultrafast information processing, thanks to lightwave-based petahertz electronics, ref [12]. Indeed, carrier dynamics manipulation due to ultrafast field waveforms occurs at subfemtosecond time scales and is dominated by the CEP value. Finally, CEP is important in the attosecond metrology for microscopy, ref. [13], [14] and [15]. In the past, CEP detection is achieved with both frequency-domain interferometric techniques, see ref. [10], [16] and [17], and time-domain photoelectron emission, see ref. [18], [19] and [20]. These techniques require either interferometry within complex optical systems or vacuum apparatuses and high energy pulses, whereas the device studied in this work is a compact and integrable solid state detector working in ambient conditions. Time-domain CEP detection in solid state devices is demonstrated in several papers, as shown in ref. [21], [22] and [23], which make the basis of this work.

In both the field sampler and the CEP detector configurations, the optical waveform that is to be analysed is delivered to the devices as a free-space wave. Since pulse sources are going towards being completely integrated and optical signals are mainly delivered by waveguides, a need for waveguide-integrated CEP detectors and field samplers for potential operation within integrated photonics platforms arose. Furthermore fully integrated devices have a smaller foot-print. For these reasons, in the last chapter of this thesis the antennas will be integrated on top of a waveguide and coupled to waveguide modes. In particular, the design is optimized for CEP detection, but can be easily corrected for field sampling.

The electron emitters consist of a series of electrically interconnected 20-nm-thick Au antennas, shaped as isosceles nanotriangles, that can be arranged in two different configurations, one for the field sampler and one for the CEP detector. The field sampler has the sharpest tip of the nanotriangle facing a perpendicular collector nanowire, at a few tens of nm distance, as in Figure 1.1; this configuration is called "rectified". The CEP detector has the sharpest tip of the nanotriangles facing another nanotriangle, as in Figure 1.2; this configuration is called "bow-tie". These opto-electronic detectors rely on two physical phenomena: the excitation of plasmonic resonances and the photoelectron emission by strong-field optical field tunnelling. The plasmonic and geometric enhancement effects convey electric field at the sharpest tip of the nanotriangles, when the material is illuminated.

The enhanced field bends the potential barrier at the tip surface and drive optical-field photoemission toward the collector wire or triangle. The emission can be approximated by a quasi-static tunnelling rate and is then calculated by a quasi-static Fowler-Nordheim (FN) emission model.

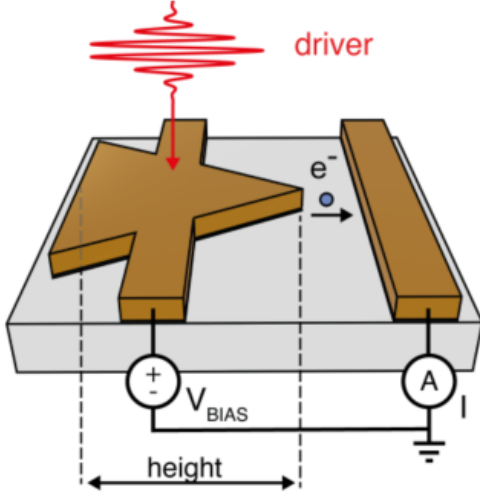


Figure 1.1: Representation of the rectified nanoantennas, as in ref. [24]. No scale is present but the triangle height is ~ 280 nm.

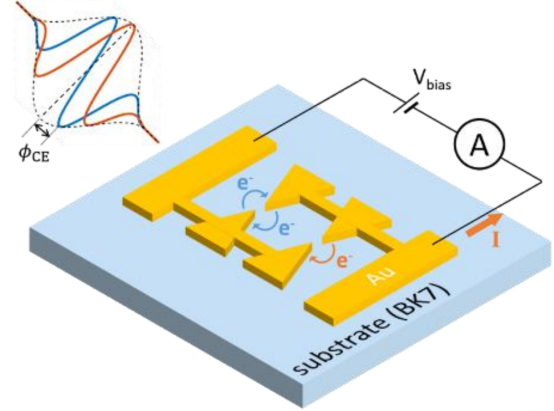


Figure 1.2: Representation of the bow-tie nanoantennas, as in ref. [23]. No scale is present but the triangle height is 200 nm.

The analysed optical waveform that illuminates the antennas is an ultrashort laser pulse. The oscillation of the electric field in the wave leads to a photoemission signal that can reach petahertz-level switching speeds and hence can allow for future on-chip petahertz electronics, see ref. [23].

1.2 Background and theory

This section provides a theoretical background and overview of key concepts that will be used throughout the chapters of the thesis. A knowledgeable reader can skip this section.

1.2.1 Light pulse theory

An optical pulse is a short burst of electromagnetic energy. It can be characterized by two main features: its spectrum of frequencies and its waveform, which is the

shape and amplitude of its electromagnetic fields as a function of time. Ultrashort pulses, in particular, have time duration of the order of pico- or femtoseconds; an example of a train of pulses is shown in Figure 1.3. They have broadband spectrum and high peak intensities. They can be generated by many methods, one example is by mode-locked oscillators.

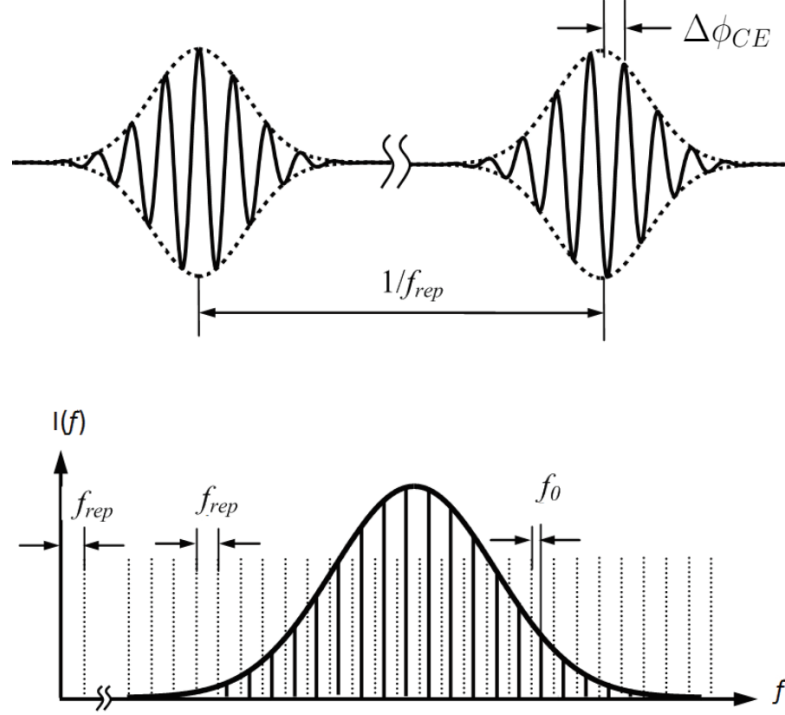


Figure 1.3: (top): ultrafast train pulse, as a function of time; $\Delta\phi_{CE}$ is the carrier-envelope phase (CEP) and f_{rep} is the repetition rate of the pulse train; (bottom): pulse train spectrum; f_0 is the carrier-envelope offset frequency (also f_{CEO}). Image from ref. [25].

The pulse duration is defined as the time range at full width at half-maximum (FWHM) of the optical power versus time. The CEP (carrier-envelope phase) is defined as the the phase between the maximum of the carrier wave and the maximum of the intensity envelope, as shown in the top-side image in Figure 1.3. In general, group and phase velocity can differ inside a material, hence CEP evolves when propagating through materials following Equation 1.1.

$$\Delta\phi_{CE} = 2\pi\omega_c \cdot l \cdot \left(\frac{1}{v_g} - \frac{1}{v_p} \right) \quad (1.1)$$

where v_g and v_p are group and phase velocities, respectively, and l is the travelled

distance in the material. The electric field of a laser pulse can be described as in Equation 1.2:

$$E(t) = A(t) \cos(\omega_c t + \phi_{CE}) \quad (1.2)$$

where $A(t)$ is the envelope function of the pulse, ω_c is the central frequency of the pulse and ϕ_{CE} is the CEP. In a train of pulses, with a repetition rate of f_{rep} , the CEP may change from pulse to pulse; this variation is called the carrier-envelope offset frequency (f_{CEO}) and it can be appreciated in the pulse spectrum as f_0 . The spectrum of a train of pulses is shown in Figure 1.3.

1.2.2 Plasmonic nanoantennas and photoemission theory

When an optical wave impinges on a material, the electrons at its surface interact with its electric field. In particular, for a metallic/dielectric interface, the incident field can lead to collective oscillations of the structure's conduction electrons. These oscillations are called surface plasmons, ref. [26], and are able to focus very strong fields to the interface. These surface plasmons can propagate along the interface or can be localized. Propagating surface plasmons are called *surface plasmon polaritons* and are evanescently confined to the interface. If the plasmonic resonance is confined to nanoparticles, it is called *localized surface plasmon* and it is usually given by an interaction with metal nanoparticles or nanostructures, so that the oscillation is confined and cannot propagate. The two types of collective oscillations are represented in Figure 1.4.

These confined resonances convey strong fields at the sharp features of a nanostructure and can lead to very strong field enhancement, as in ref. [28] and [29]. This phenomenon occurs also for geometrical effects (if the tip is very sharp), but with less intensity with respect to the plasmonic effects. In particular, the plasmonic resonance can be excited only at certain frequencies, according to geometry and materials characteristics. This leads to different field enhancement values for different frequencies. Because of this, an optical pulse that illuminates the nanostructure is enhanced and different frequency components are enhanced of different amounts. This enhancement is studied as a pulse filter function, where the time-domain response was obtained by an inverse Fourier transform of the frequency-domain response. This function is reported in a MATLAB code, developed by Y. Yang¹ and presented in ref. [23], [30] and [22]; it is reported in Appendix A, as "pulsefilter.m".

¹Research Assistant of QNN Group at MIT

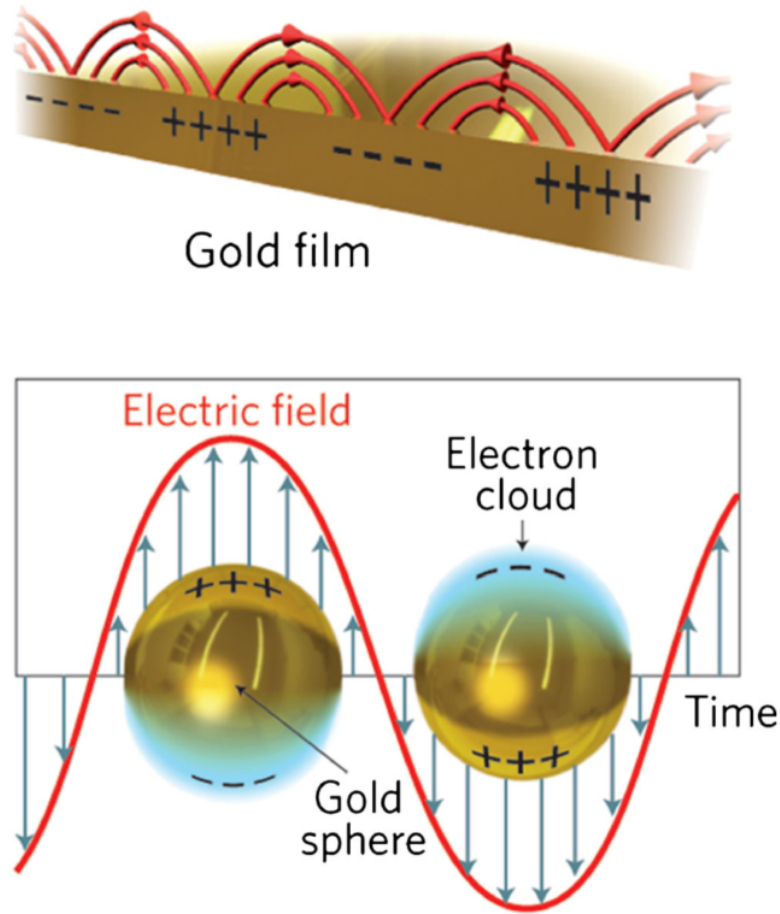


Figure 1.4: Surface plasmons representation. (top): surface plasmon polaritons representation; (bottom): localized surface plasmon representation. Image from ref. [27].

Fowler-Nordheim photoemission theory

High intensity fields can lead to photoemission of electrons from the antennas surface. In particular, at strong-field regimes, light-matter interactions are dominated by the electric field of the incident light, whereas at low intensities they are photon-driven, i.e. driven by the pulse's photon energy and flux. At high intensities, photoemission behaves like field-controlled tunnelling: the electric field deflects the potential barrier at the the metal surface and helps the electrons exit the material. That's why the electric field of the carrier wave of the pulse dominates photoemission and hence the CEP value becomes of great influence. In particular, field enhancement at nanotips can drive strong-field processes, as shown in ref. [31],

[32], [33], [34], [35], [36] and [37]. This emission can be approximated by a quasi-static tunnelling rate and is calculated by a quasi-static Fowler-Nordheim (FN) emission model, ref. [38]. As explained in ref. [39], "Fowler-Nordheim tunneling is electric-field induced electron tunneling through a roughly triangular (in practice, always rounded) potential-energy barrier". Indeed, in strong-field regime, the potential barrier is deflected and the tunnelling distance that the electrons have to travel is shortened. This process is shown in Figure 1.5. The considered triangular potential barrier is considered rounded in the FN theory.

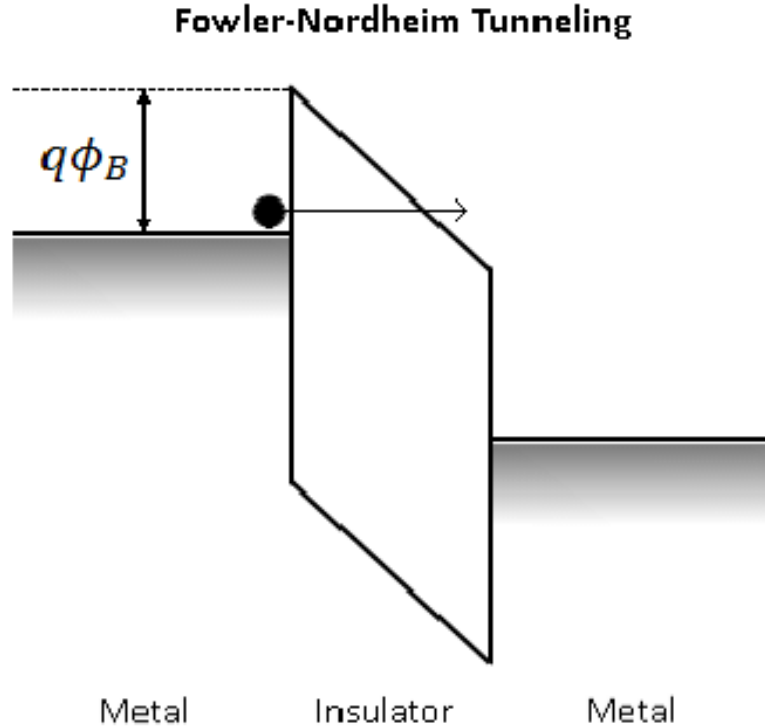


Figure 1.5: Fowler-Nordheim tunnelling. In the image is reported the triangular potential-energy barrier considered in Fowler-Nordheim tunnelling model. The barrier tip is always rounded in this model. Image from ref. [40].

The process to obtain FN tunnelling formula is to follow these steps: first, the "escape probability" of an electron through a rounded barrier; then, it is integrated over all of the electron states; finally, it is integrated to obtain the emitted current density as a function of field and work function, as in Equation 1.3, from ref. [41].

$$J = \frac{e^3 F^2}{8\pi h \phi t(y)} \exp \left[-\frac{8\pi(2m)^{\frac{1}{2}} \phi^{\frac{3}{2}}}{3heF} v(y) \right] \quad (1.3)$$

One can notice that the parameters that can increase tunnelling current are

the electric field F and the work function ϕ . In general, Fowler-Nordheim-type equations are utilized, that are approximate versions that express current density J as a function of electric field F , as studied in Section 3.3.4.

1.2.3 Waveguide theoretical analysis

Finally, the light pulse that is incident on the antennas can be delivered through a waveguide, instead of through vacuum or air. The waveguide material, though, can introduce chromatic dispersion, given the different frequency components, and causes a difference in phase and group velocity, which leads to CEP shifts along the waveguide. This can be predicted by analytically studying the waveguide dimensions and materials. The following analysis is reported in ref. [42]. A rectangular optical waveguide is shown in Figure 1.6.

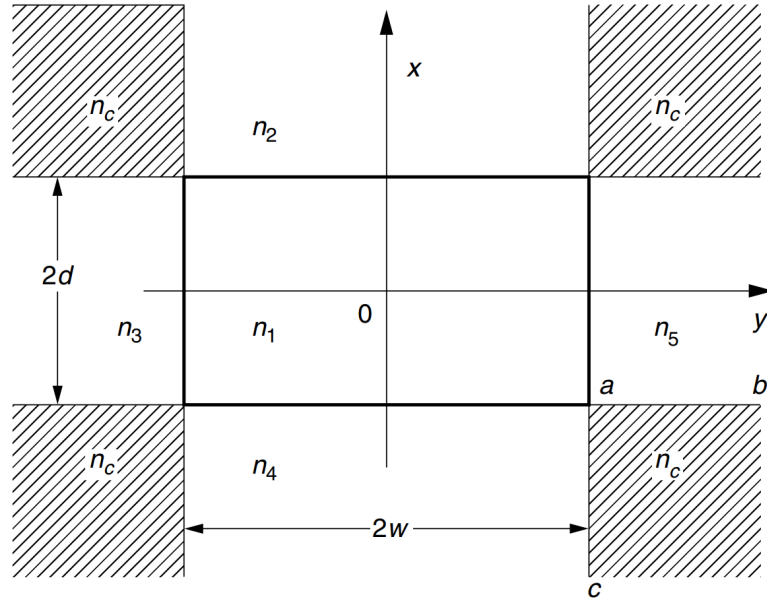


Figure 1.6: Representation of the section of a rectangular waveguide. The material tagged by the n_1 refractive index is the core material, whereas n_2, n_3, n_4, n_5 stand for the cladding materials. In the n_c regions, the analytical model is not defined. $2w$ is the core width and $2d$ is the core height. Image from ref. [42]

The waveguide working principle is the total internal reflection at the interface between core and cladding. This phenomenon makes the light confined in the core of the device and very little optical power exits to the cladding. The thickness is $2d$ and the width is $2w$. The refractive indexes n_2, n_3, n_4 and n_5 of the cladding are the same in the considered case and have to be smaller than n_1 of the core, in order to obtain total internal reflection. As one can see, in a rectangular waveguide, light

is confined in 2 directions (x,y), whereas in the third direction the field theoretically extends indefinitely.

In this section, the considered input wave is a transverse magnetic (TM) plane wave, which has only transverse and no longitudinal magnetic field, so $H_z = 0$. The most used mathematical approach to this configuration is called the "wave optics approach" and it is carried out for both the confined directions (x,y). It consists in evaluating the wave equation for the TM mode wave, both in the core of the waveguide and in the cladding. This differential equation leads to two kinds of solutions: trigonometric oscillating solutions, such as $\cos(Kx)$ and $\sin(Kx)$, for the core and exponential solutions $e^{\gamma x}$ and $e^{-\gamma x}$ for the cladding. Thus, confined oscillating solutions are found in the core and exponentially decaying solutions for the cladding. Then, boundary conditions and continuity of the electric field components are applied, to obtain the *characteristic equations* for the TM modes, in order to find the values for the two parameters K and γ , which are useful to obtain all the possible modes for a waveguide. Depending on the characteristics of the guide, the allowed modes are selected.

The propagation constant β of the fundamental mode is considered for both confined directions. From the mode propagation constant as a function of input frequency, many important quantities can be derived. Indeed, phase velocity is defined as $v_p = \omega/\beta$ and the mode effective refractive index is defined as $n_{eff} = \beta/k_0$, where k_0 is the free-space propagation constant. Furthermore, the group velocity is defined as $v_g = \frac{\partial \omega}{\partial \beta}$. From these quantities, the CEP shift given for a travelled distance l in the waveguide can be calculated as:

$$\Delta\phi_{CE} = 2\pi\omega \cdot l \cdot \left(\frac{1}{v_g} - \frac{1}{v_p} \right) \quad (1.4)$$

Chapter 2

Ultrafast electromagnetic pulse interactions with rectified nanoantennas for optical-field sampling

The first device configuration that is simulated and analysed in this thesis is the field sampler. As explained in the Introduction, it is used for low-energy, near-infrared waveforms field sampling. It can lead to important applications such as precise attosecond metrology, studies on strong-field light-matter interaction and time-domain spectroscopy of molecular fingerprints, see ref. [1] and [2]. Direct optical-field sampling in the time-domain has already been explored, ref. [3], [4], [5], [6] and [7], but these devices often require large pulse energies, bulky apparatuses and vacuum environments. The devices studied in this work are on-chip (so compact and integrated) and can study low energy, near-infrared arbitrary pulses in ambient conditions.

The device was thought, designed and fabricated by the QNN group (Quantum Nanostructures and Nanofabrication) at MIT (Massachusetts Institute of Technology) and its report is currently in the publication process, see ref. [24] for the arXiv publication. The author of this thesis worked with the group for the frequency-domain simulation of the device in order to understand how the nanoantennas interact with light waveforms to control the optical-field sampling process.

The device consists of an array of plasmonic nanoantennas shaped as single

nanotriangles, which are electrically interconnected by means of a connecting wire and have a collection nanowire in front of the tip of the antennas, as shown in Figure 2.1. The simulation cell used to analyse the device is shown in Figure 2.2; the lateral boundary conditions are set as "periodic" in order to replicate the array disposition. The nanotriangle is the electron source (cathode) and the nanowire collects the electrons (anode). The considered materials are: a borosilicate glass (BK7) substrate placed in air, a 2 nm Chromium adhesion layer between substrate and nanostructures and the 20 nm gold nanostructures.

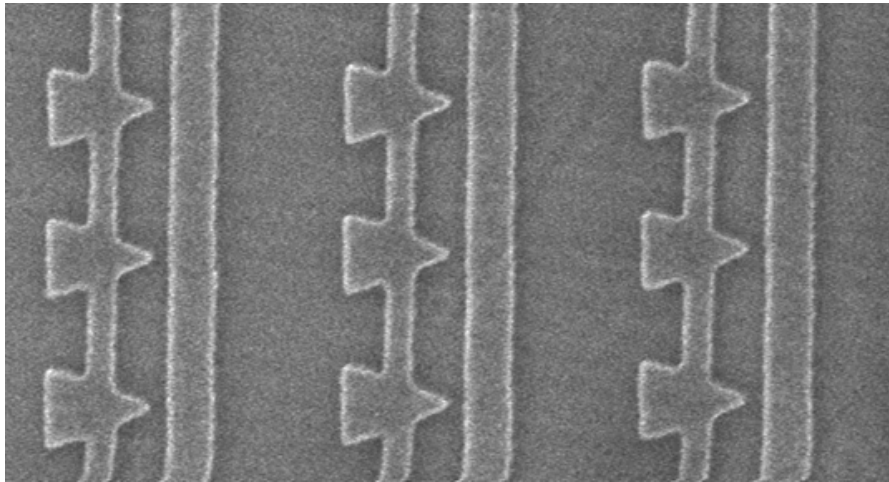


Figure 2.1: SEM image of the rectified nanoantennas, fabricated by the QNN group, ref. [24]. No scale is present but the triangle height is $\sim 280\text{nm}$

The field sampling working principle is represented in Figure 2.3 and it is as follows: an optical oscillating waveform in free-space impinges perpendicularly to the array of antennas. The polarization of light must be such that the electric field is parallel to the main altitude of the isosceles triangle. The field is enhanced by plasmonic resonance at the tips of the antennas and, according to Fowler-Nordheim tunnelling theory, electrons are extracted from the antennas tip and are collected to the nanowire in front of it. This process is repeated every cycle of the waveform, when the field is strong enough and only for the field component of the waveform that goes from the nanotriangle to the nanowire and not viceversa; this results in electrons photoemission spikes at the metal-vacuum interface once every cycle. This is why the nanoantennas that are studied in this Chapter are called "rectified"; indeed, only half of the impinging waveform contributes to the emitted electric signal. The fabricated devices are placed as arrays of nanoantennas, in order to increase the output electric signal. Indeed, several antennas are illuminated at the same time and the signal is collected from all of the illuminated ones.

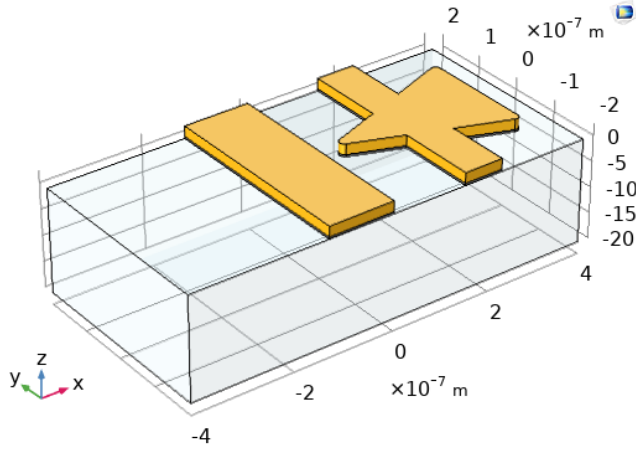


Figure 2.2: 3D COMSOL Multiphysics model for the rectified nanoantennas. The array disposition of the antennas is obtained in the simulation by setting the lateral boundary conditions as "periodic". The 20 nm Au nanostructures are represented in yellow, the 2 nm Cr adhesion layer is black and the BK7 substrate is glass-like transparent. The device is immersed in air.

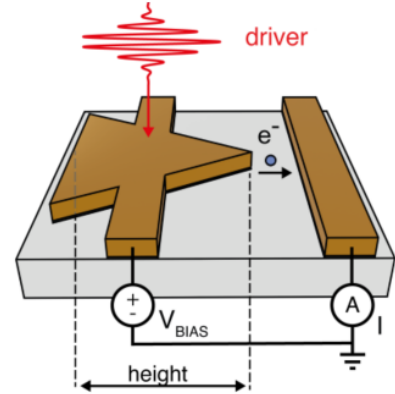


Figure 2.3: Representation of field sampling process with rectified nanoantennas, as in ref. [24]. No scale is present but the triangle height is ~ 280 nm.

Throughout this Chapter, the device electromagnetic field response is simulated in the frequency domain. This is important in order to quantitatively estimate the field behavior at the antennas tip. Indeed, in the field sampling process, it is fundamental to control the field value at the antennas tip, in order to study the possible emitted photocurrent. In particular, the excitation of plasmonic resonances is analysed through power transmission and extinction studies and the field enhancement at the device tip is sampled as a function of frequency. Since the devices are already fabricated and studied by the QNN group, extinction plots and field enhancement plots are compared to the experimental ones. In order to obtain consistent results with respect to the experimental data, the geometry of the simulated device is gradually adjusted. This is done in order to predict the effects of a reshaping phenomenon that the device undergoes during illumination.

2.1 Model setup

The device geometry is taken from SEM images of the nanostructures that were previously fabricated by the QNN group, ref. [24], as shown in Figures 2.4, 2.5 and 2.6.

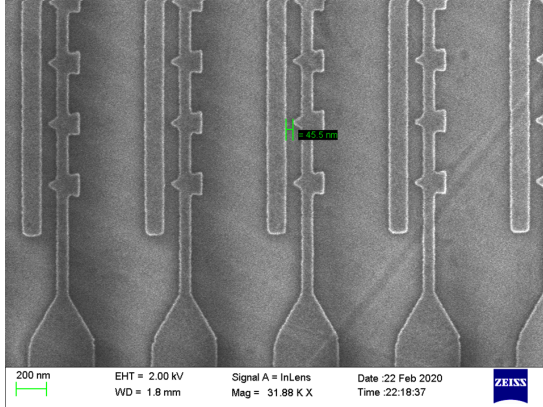


Figure 2.4: SEM image of the rectified nanoantennas, with nanotriangles with height $\sim 200\text{nm}$, fabricated by the QNN group, ref. [24].

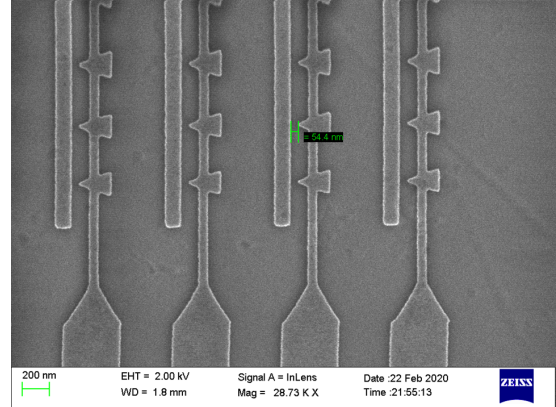


Figure 2.5: SEM image of the rectified nanoantennas, with nanotriangles with height $\sim 240\text{nm}$, fabricated by the QNN group, ref. [24].

As can be seen from the SEM images, 3 different geometries are considered according to the triangle height: $\sim 200\text{ nm}$, $\sim 240\text{ nm}$ and $\sim 280\text{ nm}$. These values are the ones that were set in the layout for the fabrication and can vary in the actual fabricated device, due to several factors that will be described later.

The simulator is a finite element method electromagnetic solver (COMSOL Multiphysics); in order to replicate the array disposition, the simulation cell lateral boundary conditions are set to "periodic". The input electric field amplitude E_0 is set to 1V/m and it is polarized along the main height of the nanotriangle. The optical properties of Au and Cr are taken from ref. [43]. The BK7 refractive index is fixed to 1.5 as its variation is negligible in the considered frequency range.

The considered geometries are listed in Table 2.1; the values are obtained by measuring 3 devices for each geometry in the SEM images and averaging them.

The fabricated devices undergo illumination, which causes a laser-induced reshaping of the triangles and the change of the relative position between the wires and the nanotriangles, as a result of reshaping, as it is explained in ref. [23]. The

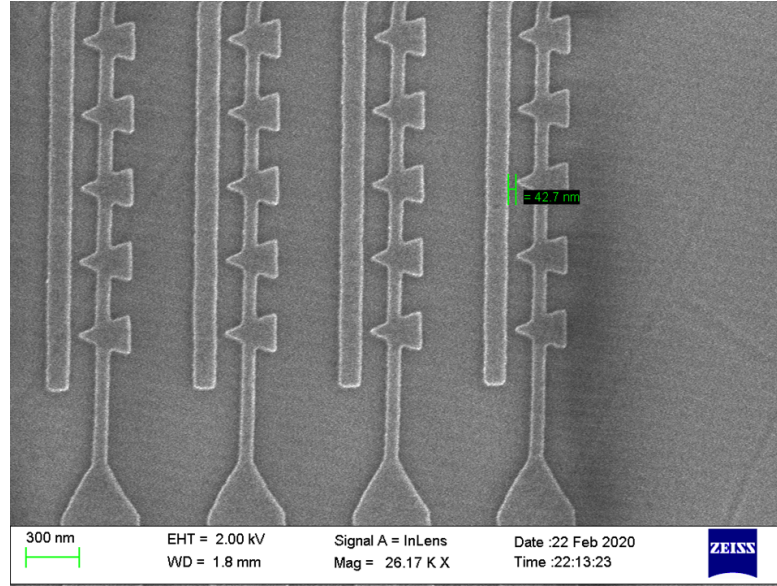


Figure 2.6: SEM image of the rectified nanoantennas, with nanotriangles with height $\sim 280\text{nm}$, fabricated by the QNN group, ref. [24].

Geometry features (in nm)	200 nm	240 nm	280 nm
- "Rectifying" wire width	125.9	118.3	129.3
- Connecting wire width	75.5	67.2	76.7
- Triangle base	170.8	198.7	234.3
- Triangle height	232.8	260.1	314.3
- Distance between wires ($wire_x$)	100.3	132	147
- Distance from the right border of the "rectifying" wire to the triangle base	250.6	294.5	338.6
- Simulation domain, horizontal dimension	801.7	805.6	820.2
- Simulation domain, vertical dimension	410.7	446.4	409.1
- Radius of curvature of the triangle vertices	14.5	11.1	9.8

Table 2.1: Features dimensions for the 3 considered geometries. The listed values are obtained by measuring 3 devices for each geometry in the SEM images and averaging them. The triangle heights and bases are reported without taking into account the rounding of the tips, so the actual dimensions will be shorter in the simulated geometry.

SEM images in Figures 2.4, 2.5 and 2.6 do not take into account the reshaping, so this effect is not taken into account in the initial study of the device. After this

reshaping, the geometry settles to permanent dimensions; throughout this thesis discussion, the simulated geometries will be tweaked and changed in order to match the reshaped ones.

2.2 Results

Frequency-domain analysis

The frequency sweep range in which the devices are studied is [800 nm, 2000 nm]. This is chosen since the fabricated devices show relevant features in this range. The devices are analysed with the help of 2 main graphs: the extinction plot and the field enhancement at the tip plot. The extinction plot is obtained by formula (2.1):

$$-10 \cdot \log_{10}(T/T_0) \quad (2.1)$$

where T is a function of ω and is the power transmission of the whole device and T_0 is a function of ω and is the power transmission calculated without the nanoantenna structure but still with the BK7 substrate. This plot shows at which frequencies the most power is absorbed, hence it indicates at which frequencies plasmonic resonances occur. Indeed, plasmonic resonances focus large quantities of field to a very narrow region of space, which is likely absorbed by the metal structure. The field enhancement at the tip of the device (sometimes expressed as FE) is defined as the field norm averaged over the tip's surface, divided by a field reference value. The reference value is in this case the input field E_0 . The tip surface over which the average operation is carried out is the one showed in Figures 2.7 and 2.8.

This plot shows at which frequency the field reaches maximum values at the triangle tip. This is helpful in order to understand the interaction of a pulse with the plasmonic nanoantennas; indeed, the frequency components of the pulse will be enhanced according to field enhancement at tips.

2.2.1 Initial geometry

The first considered geometries are the ones reported in Table 2.1.

240nm geometry

The resulting extinction plot is shown in Figure 2.9.

This plot is obtained by applying the extinction formula (2.1) to the power transmission T plot showing in Figure 2.10 and to the plot of T_0 as in Figure 2.11.

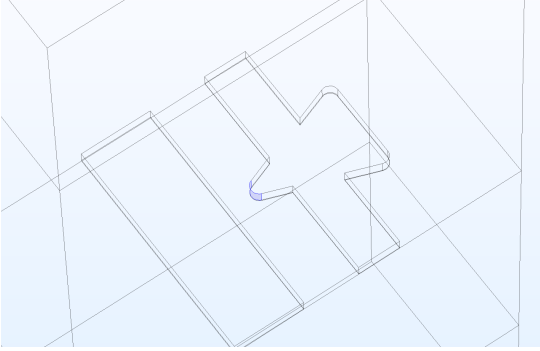


Figure 2.7: 3D COMSOL Multiphysics model for the rectified nanoantennas. No scale is present but the triangle height is ~ 280 nm. In blue is highlighted the tip surface over which the field average operation is carried out

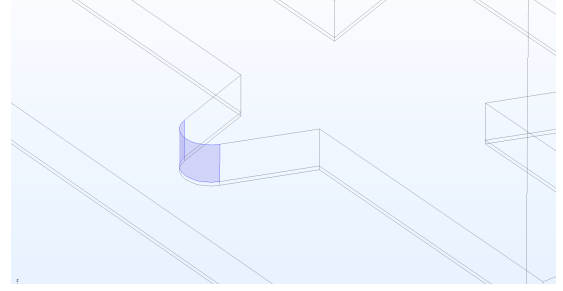


Figure 2.8: 3D COMSOL Multiphysics model for the rectified nanoantennas. No scale is present but the triangle height is ~ 280 nm. In blue is highlighted the tip surface over which the field average operation is carried out

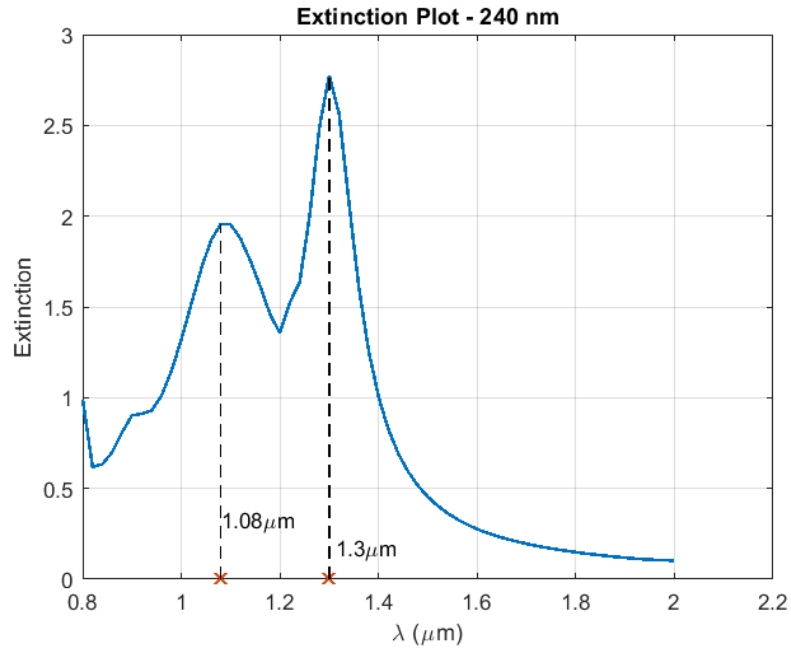


Figure 2.9: Extinction plot for the 240 nm geometry, as listed in Table 2.1.

As one can see from the power transmission T_0 without the metal structure, in Figure 2.11, almost all of the power is transmitted through the BK7 substrate, for

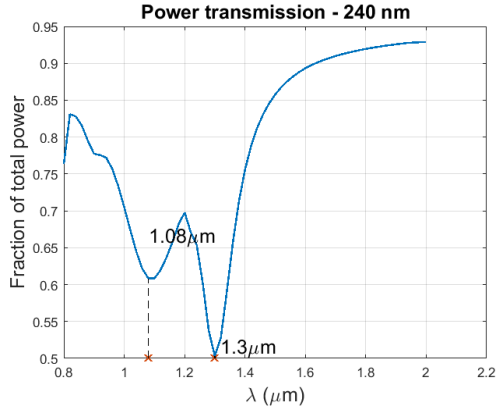


Figure 2.10: Power transmission plot for the 240 nm geometry, as listed in Table 2.1.

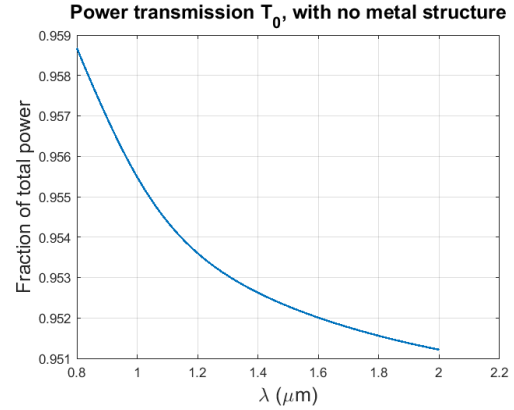


Figure 2.11: Power transmission T_0 calculated without the nanoantenna structure but still with the BK7 substrate.

any frequency. Whereas, as in Figure 2.10, for some frequencies power is partially not transmitted to the output port, creating dips in the power transmission plot. This is reflected in the extinction plot in Figure 2.9, where for $\lambda = 1.08 \mu\text{m}$ and for $\lambda = 1.3 \mu\text{m}$ two peaks are present. The two peaks are due to plasmonic resonance and geometric enhancement of the field at the tip. This can be seen by looking at the field distribution in the device for the two frequencies. It is shown in Figures 2.12 and 2.13, respectively.

As one can see in figure 2.12, a maximum for the electric field E at the tip that's closest to the "rectifying" nanowire is observable. The corresponding peak in the extinction plot is called "tip-mode", since it shows an excitation to the tip of the antenna. Whereas in Figure 2.13, a maximum for the electric field E at the other two tips of the antenna and at the border of the connection wire is observable. The corresponding peak in the extinction plot is called "wire-mode", since it shows an excitation to the wire and to the external tips of the antenna. In most cases, the peak of the extinction plot corresponding to the wire-mode is higher, since the wire and the external tips of the antenna possess more surface and absorb more power than the tip of the antenna, so less power is transmitted when the wire-mode is excited. The field enhancement plot is showed in Figure 2.14.

In the field enhancement figure, one can see a main peak for $\lambda = 1.12 \mu\text{m}$ and a small peak for $\lambda = 1.42 \mu\text{m}$. The field distribution for these two wavelengths are shown in Figures 2.15 and 2.16.

The main peak shows a very high field enhancement of ~ 18 , which shows the effects of plasmonic resonance and enhancement. The main peak is at around the same wavelength of the tip-mode extinction peak. The fact that they are not at

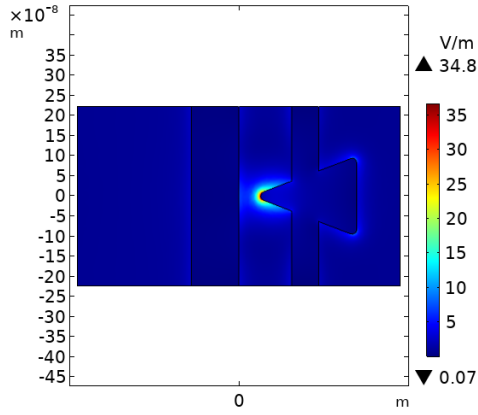


Figure 2.12: Field distribution at the wavelength corresponding to the tip-mode in the extinction plot for the 240 nm geometry, as listed in Table 2.1.

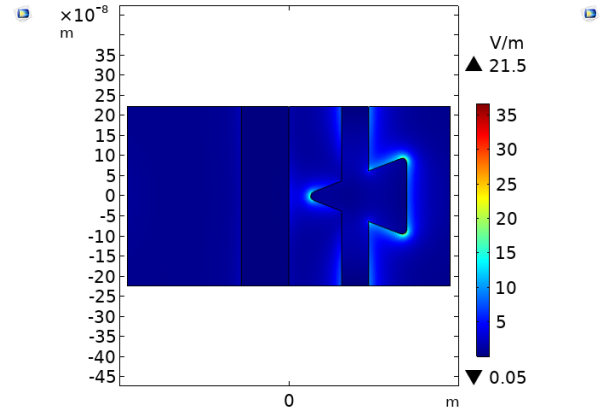


Figure 2.13: Field distribution at the wavelength corresponding to the wire-mode in the extinction plot for the 240 nm geometry, as listed in Table 2.1.

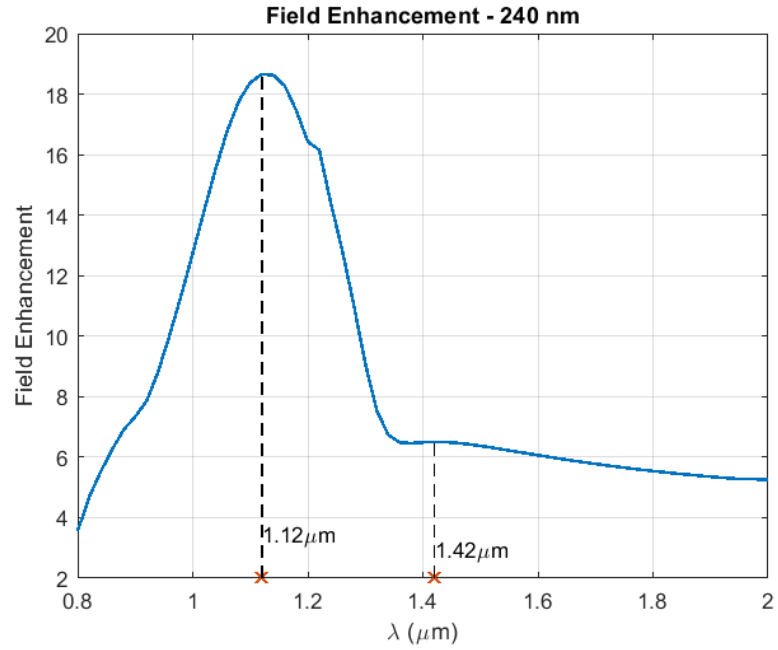


Figure 2.14: Field enhancement plot for the 240 nm geometry, as listed in Table 2.1.

the exact same wavelength may be due to the fact that a peak in extinction shows where the most power is absorbed by the tip (and its surroundings) and this can

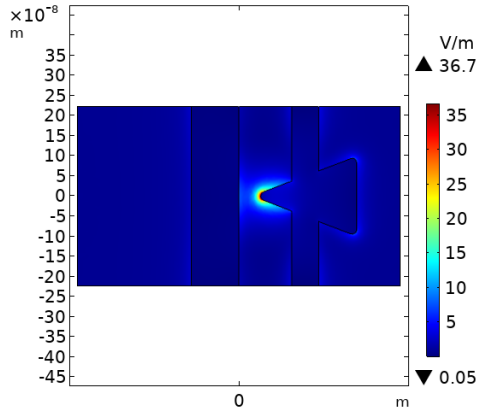


Figure 2.15: Field distribution at the wavelength corresponding to the main peak in the field enhancement plot for the 240 nm geometry, as listed in Table 2.1.

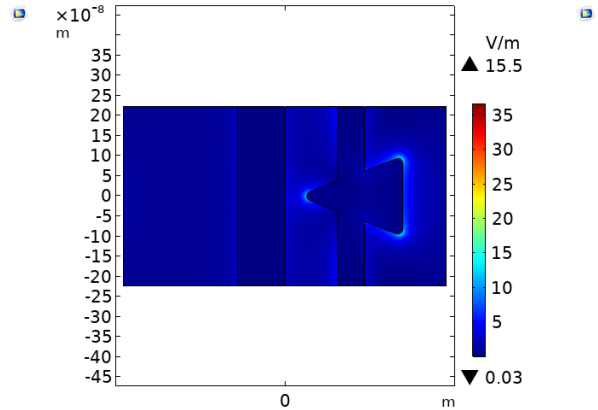


Figure 2.16: Field distribution at the wavelength corresponding to the secondary peak in the field enhancement plot for the 240 nm geometry, as listed in Table 2.1.

be at a different λ with respect to the maximum field at the tip. For example, for $\lambda = 1.12 \mu\text{m}$ the field is strongly confined to the tip, but not so much power is absorbed by the whole tip structure; on the other hand, for $\lambda = 1.08 \mu\text{m}$, the field is not as concentrated at the tip surface, but it is confined in the portion of the triangle that's close to the tip and a great amount of power is absorbed by that volume of the structure. The small peak in FE may be due to a light excitation of the whole structure, as can be seen by Figure 2.16, which leads to a light enhancement all around the triangle. The same reasoning can be applied to the other two structures (280 nm and 200 nm geometries).

280nm geometry

The resulting extinction plot is shown in Figure 2.17.

This plot is obtained by applying formula (2.1) to the power transmission T plot showing in Figure 2.18 and to the plot of T_0 as in Figure 2.11.

The extinction plot in Figure 2.17 shows a tip-mode peak for $\lambda = 1.2 \mu\text{m}$ and a wire-mode peak at $\lambda = 1.28 \mu\text{m}$. This can be seen by looking at the field distribution in the device for the two frequencies, which is shown in Figures 2.19 and 2.20, respectively.

The field enhancement plot is showed in Figure 2.21.

In the field enhancement figure, one can see a main peak for $\lambda = 1.18 \mu\text{m}$ and a small peak for $\lambda = 1.34 \mu\text{m}$. The field distribution for these two wavelengths are

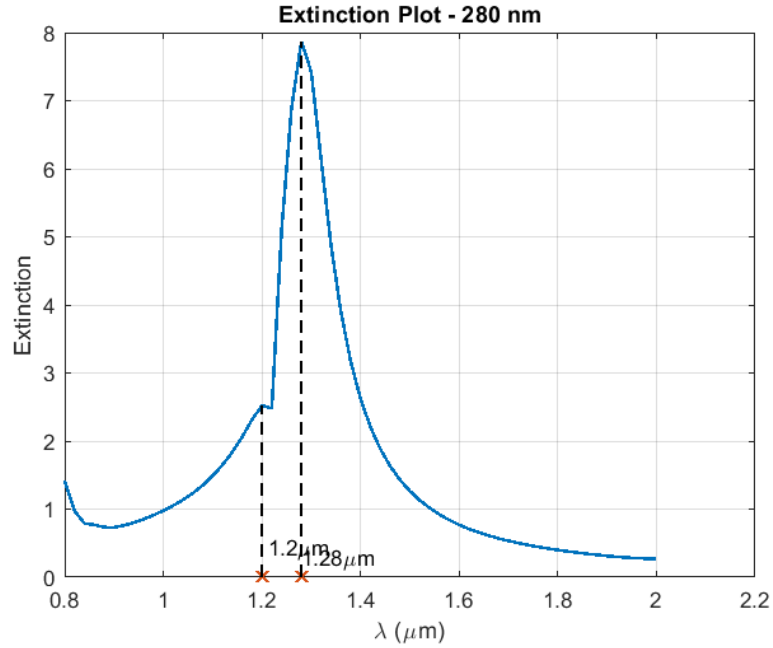


Figure 2.17: Extinction plot for the 280 nm geometry, as listed in Table 2.1.

shown in Figures 2.22 and 2.23.

200nm geometry

The resulting extinction plot is shown in Figure 2.24.

This plot is obtained by applying formula (2.1) to the power transmission T plot showing in Figure 2.25 and to the plot of T_0 as in Figure 2.11.

The extinction plot in Figure 2.24 shows a tip-mode peak for $\lambda = 0.96 \mu\text{m}$ and a wire-mode peak at $\lambda = 1.2 \mu\text{m}$ and a small peak at $\lambda = 0.84 \mu\text{m}$. This can be seen by looking at the field distribution in the device for the two main peaks. It is shown in Figures 2.26 and 2.27, respectively. The small peak is just a slight increase in the power absorption.

The field enhancement plot is showed in Figure 2.28.

In the field enhancement figure, one can see a main peak for $\lambda = 0.98 \mu\text{m}$ and a small peak for $\lambda = 1.2 \mu\text{m}$.

The field distribution for these two wavelengths are shown in Figures 2.29 and 2.27.

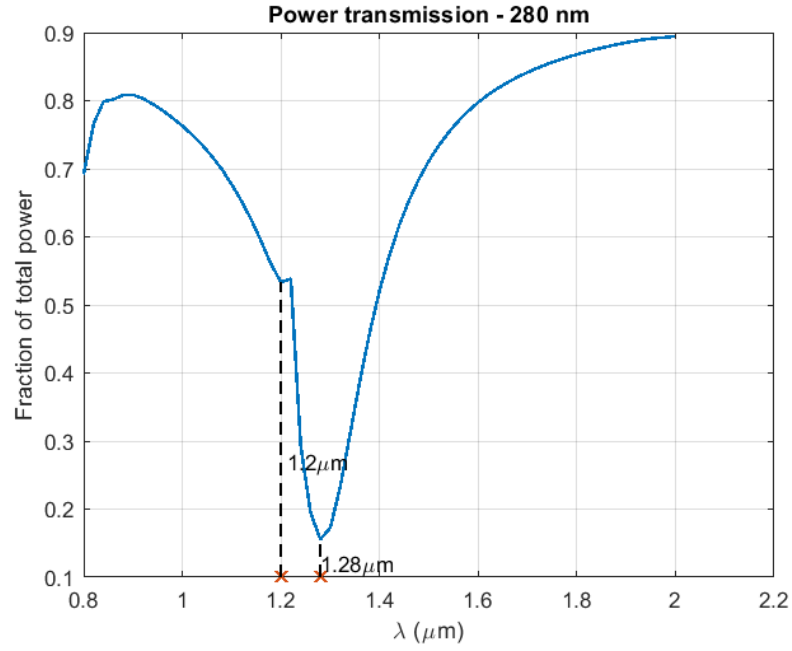


Figure 2.18: Power transmission plot for the 280 nm geometry, as listed in Table 2.1.

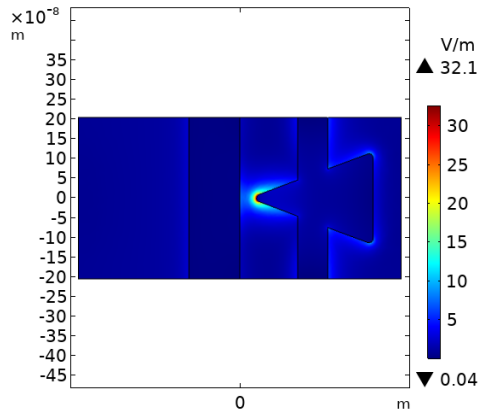


Figure 2.19: Field distribution at the wavelength corresponding to the tip-mode in the extinction plot for the 280 nm geometry, as listed in Table 2.1.

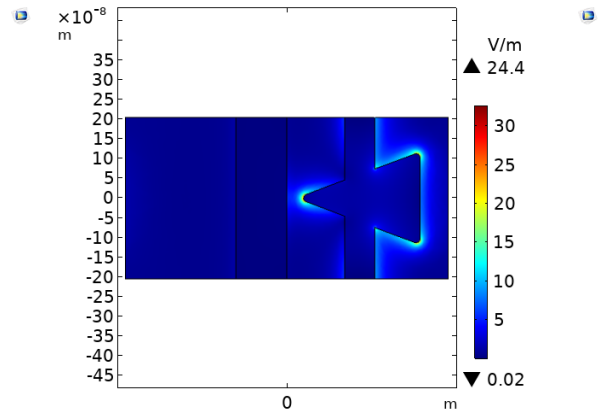


Figure 2.20: Field distribution at the wavelength corresponding to the wire-mode in the extinction plot for the 280 nm geometry, as listed in Table 2.1.

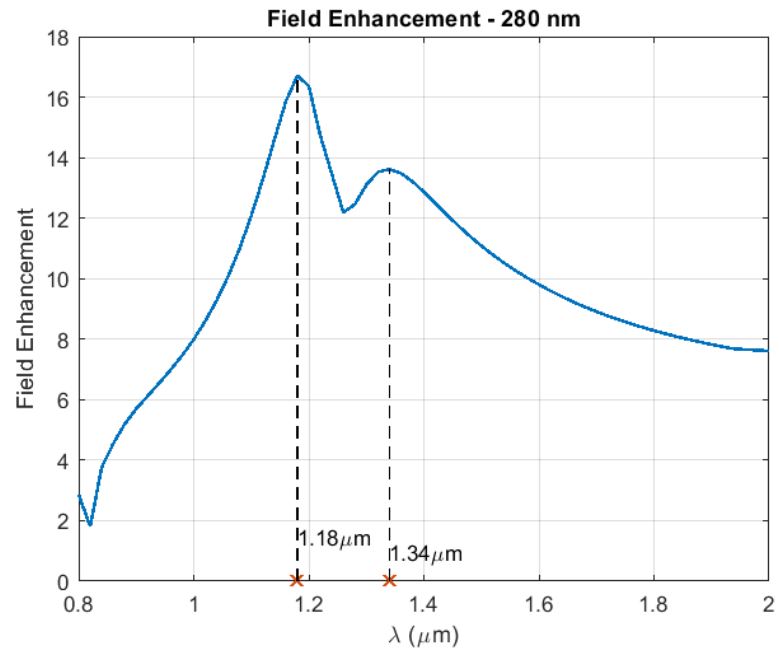


Figure 2.21: Field enhancement plot for the 280 nm geometry, as listed in Table 2.1.

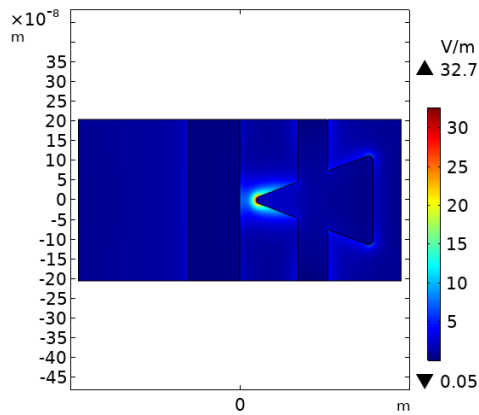


Figure 2.22: Field distribution at the wavelength corresponding to the main peak in the field enhancement plot for the 280 nm geometry, as listed in Table 2.1.

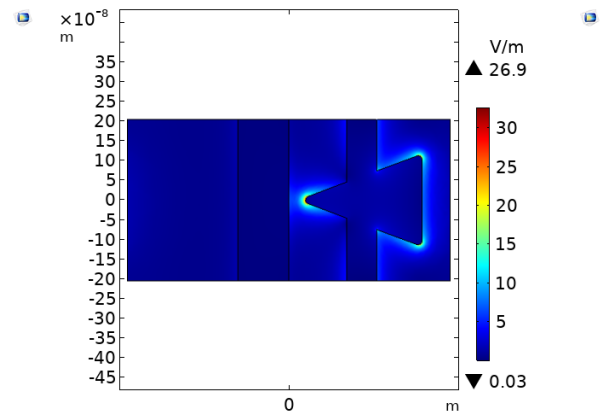


Figure 2.23: Field distribution at the wavelength corresponding to the secondary peak in the field enhancement plot for the 280 nm geometry, as listed in Table 2.1.

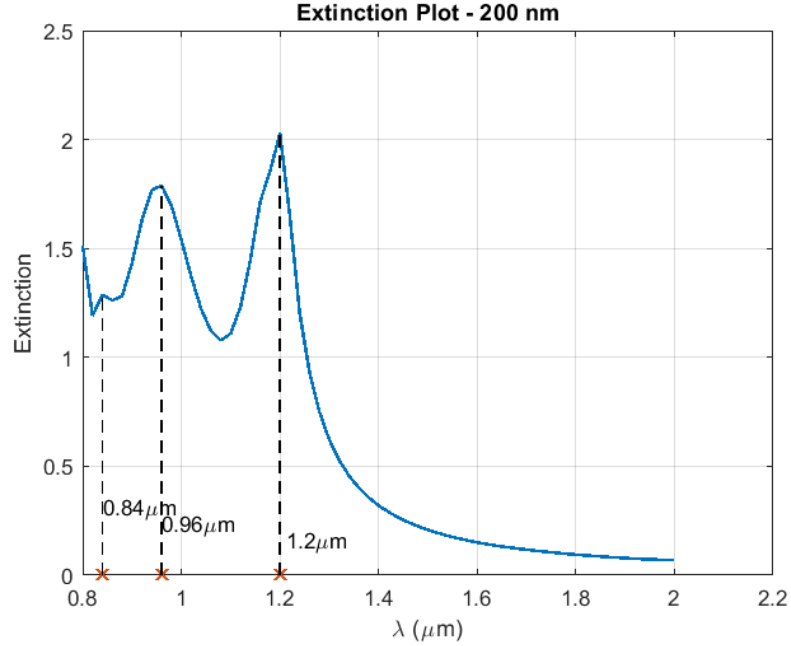


Figure 2.24: Extinction plot for the 200 nm geometry, as listed in Table 2.1.

2.2.2 Geometry adjustments

As explained in Section 2.1, the device geometry in the simulation needs to be tuned, in order to replicate the fabricated devices behaviour. Indeed, experimental extinction plot is obtained after the device being reshaped due to laser illumination. The experimental extinction plot is reported in Figure 2.30.

As might be seen, the experimental peaks wavelengths for the different geometries, are as in Table 2.2.

Geometries	tip-mode peak	wire-mode peak	other peaks
200 nm	$\sim 0.98 \mu\text{m}$	$\sim 1.12 \mu\text{m}$	$\sim 1.09 \mu\text{m}$
240 nm	$\sim 1.03 \mu\text{m}$	$\sim 1.15 \mu\text{m}$	—
280 nm	$\sim 1.01 \mu\text{m}$	$\sim 1.19 \mu\text{m}$	—

Table 2.2: The data in the table corresponds to the wavelengths at which the peaks occur in the extinction plots of the fabricated devices, as in Figure 2.30."

The process of tweaking the geometry consists in understanding which geometry feature can affect the position of extinction plot peaks and find their correct combination, in order to replicate the behaviour of the fabricated devices. The main relevant features are already studied by the authors of ref. [23] for a slightly

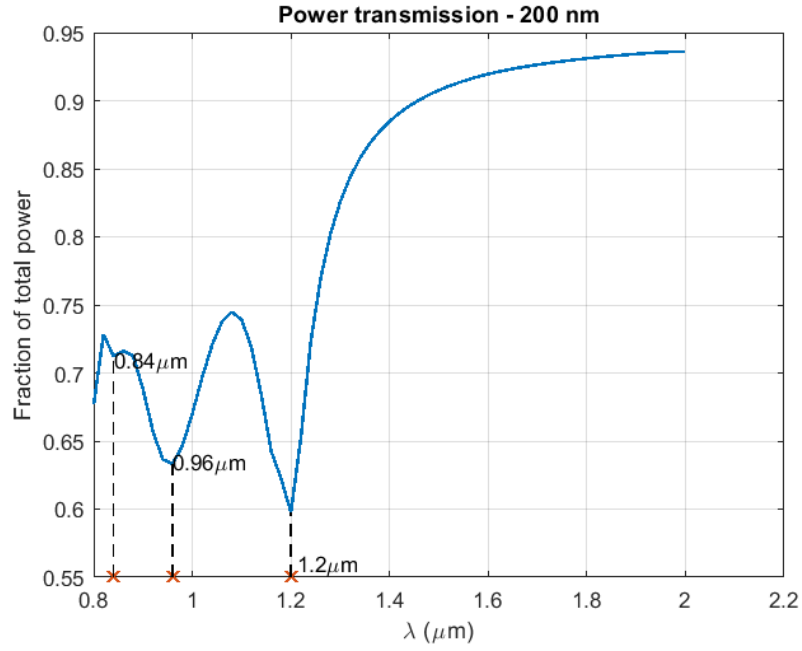


Figure 2.25: Power transmission plot for the 200 nm geometry, as listed in Table 2.1.

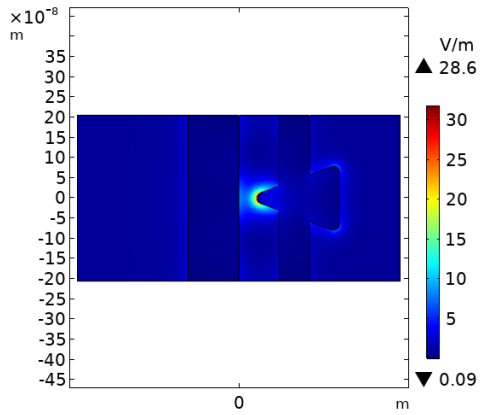


Figure 2.26: Field distribution at the wavelength corresponding to the tip-mode in the extinction plot for the 200 nm geometry, as listed in Table 2.1.

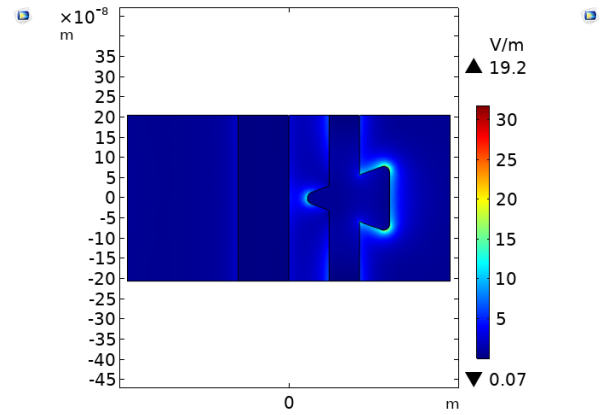


Figure 2.27: Field distribution at the wavelength corresponding to the wire-mode in the extinction plot for the 200 nm geometry, as listed in Table 2.1.

different device; they found out that the main feature is the portion of tip that exits from the connecting wire. This can be tuned by means of the connecting

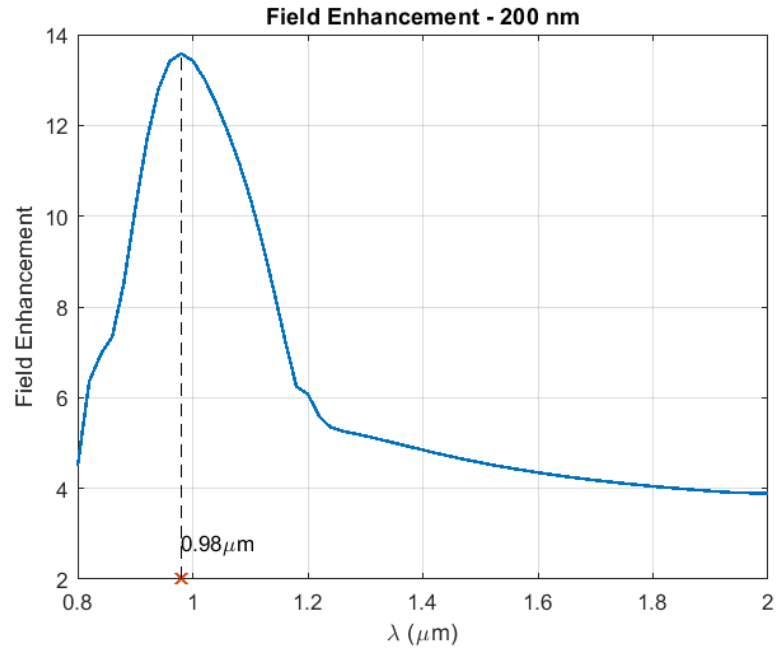


Figure 2.28: Field enhancement plot for the 200 nm geometry, as listed in Table 2.1.

wire position ("distance from the "rectifying" nanowire", in Table 2.3), the triangle height, the tip radius of curvature and, in general, the dimension of this portion of device itself. Despite the device illustrated in Table 2.1, which is a consistent measure of the SEM images of the devices (the values are obtained by averaging over multiple measures), in the following section of the work is reported the author's effort chronologically, in order to show the influence of each device's feature singularly.

Direct measure on SEM images

The first devices geometries that are analysed are obtained by a single measure of the same SEM images as in in Figures 2.4, 2.5 and 2.6, without any average operation. The obtained dimensions are reported in Table 2.3.

The resulting extinction plots are reported in Figure 2.31 and the wavelengths at which the main peaks occur are reported in Table 2.4. In the same table are listed the experimental values for the extinction plot as in Figure 2.30.

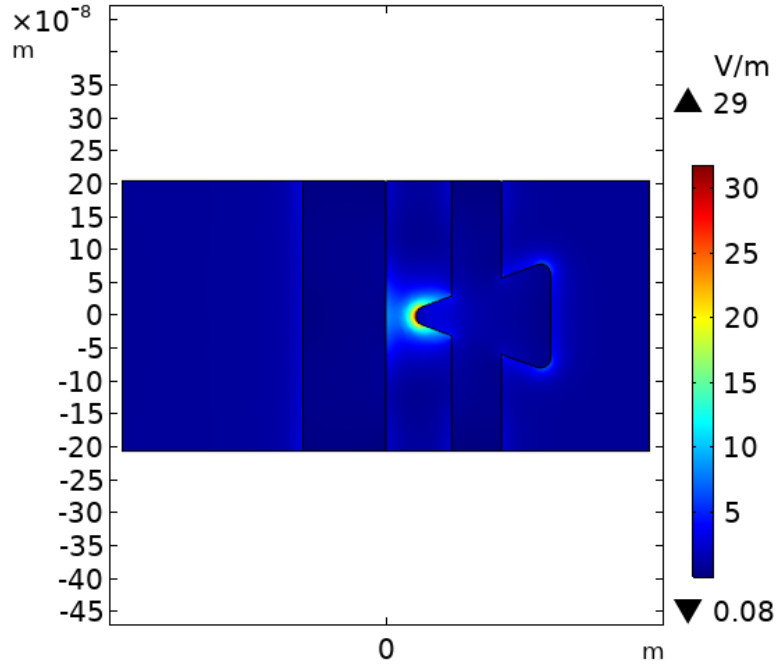


Figure 2.29: Field distribution at the wavelength corresponding to the main peak in the field enhancement plot for the 200 nm geometry, as listed in Table 2.1.

Connecting wire position tweaking

One can see that the simulation results are quite different to the experimental ones, so the connecting wire position is tweaked. The wire position, named "*wire_x*", is tweaked in a $[-5\%, +5\%]$ range with respect to the original measured value. The wavelengths at which the peaks occur in the extinction plots are reported in Table 2.5, whereas the ones for the field enhancement plot are in Table 2.6.

Throughout the tables, a trend can be observed. Indeed, when increasing the "*wire_x*" parameter, the tip-mode peak tends to increase its wavelength, whereas the wire-mode peak tends to decrease its wavelength, and viceversa if the "*wire_x*" parameter is decreased. As one can see, for different geometries different variations in the position of the connecting wire are needed to get the extinction and field enhancement plots as similar as the experimental ones. For the 200 nm geometry, the $+5\%$ variation is considered, for the 240 nm one, no variation is considered and for the 280 nm one, the -5% one is the best choice.

Triangle height tweaking

Since the 280 nm case showed no tip-mode peak, the wire position is kept to the -5% value and the triangle height is varied in a $[-5\%, 0\%]$ range. The results are

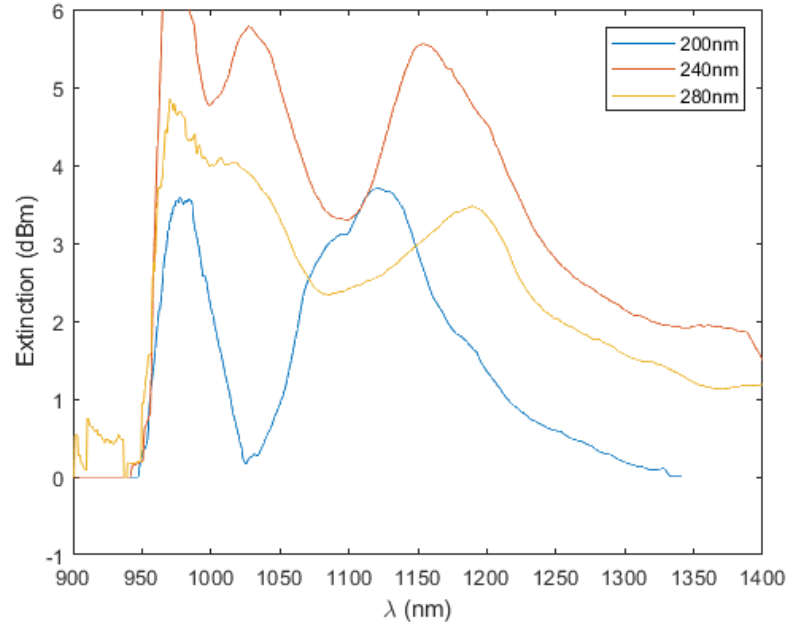


Figure 2.30: Experimental extinction plot for the devices fabricated by the QNN group and that are shown in the SEM images in Figures 2.4, 2.5 and 2.6.

listed in table 2.7.

The closest geometry to the experimental one is the -5% triangle height one.

Averaged measures on SEM images

As already explained in Subsection 2.2.1, once that the influence of these two geometry parameters is tested, a new measure on the SEM images is carried out. The devices measures were already listed in Table 2.1; the values are obtained by measuring 3 devices for each geometry in the SEM images and averaging them, in order to get a more representative measurements for the devices in the array. As seen in Subsection 2.2.1, these simulated geometries cannot replicate the experimental behaviour, so more tweaking is required.

Tip shrinking

In order to replicate the fabricated devices behaviour, the tips of the devices are shrunk. Indeed, the laser-induced reshaping that the fabricated devices undergo during illumination consists mainly in shrinkage of the portion of antenna that protrudes from the connecting wire towards the "rectifying" wire (i.e. the tip of the device). Some reduction is also seen in the rest of the device (triangles and wires).

Geometry features (in nm)	200 nm	240 nm	280 nm
- "Rectifying" wire width	130	130.8	130
- Connecting wire width	80	76.9	80
- Triangle base	173.3	215.4	245
- Triangle height	218.3	262	316.7
- Distance between wires ($wire_x$)	100	128	145
- Distance from the right border of the "rectifying" wire to the triangle base	250.5	300	341.7
- Simulation domain, horizontal dimension	800	800	800
- Simulation domain, vertical dimension	400	400	400
- Radius of curvature of the triangle vertices	10	10	10

Table 2.3: Features dimensions for the 3 considered geometries. The listed values are obtained by a single measure on one device for each geometry in the SEM images. The triangle heights and bases are reported without taking into account the rounding of the tips, so the actual dimensions will be shorter in the simulated geometry. The simulation domain dimensions are forcefully set to $800\text{nm} \times 400\text{nm}$, because are the ones that were set in the fabrication process.

	tip-mode peak	wire-mode peak	other peaks
200 nm experimental	$\sim 0.98\ \mu\text{m}$	$\sim 1.12\ \mu\text{m}$	$\sim 1.09\ \mu\text{m}$
200 nm simulated	$0.94\ \mu\text{m}$	$1.2\ \mu\text{m}$	$1.14\ \mu\text{m}$
240 nm experimental	$\sim 1.03\ \mu\text{m}$	$\sim 1.15\ \mu\text{m}$	—
240 nm simulated	$1.04\ \mu\text{m}$	$1.22\ \mu\text{m}$	—
280 nm experimental	$\sim 1.01\ \mu\text{m}$	$\sim 1.19\ \mu\text{m}$	—
280 nm simulated	$\sim 1.16\ \mu\text{m}$	$1.26\ \mu\text{m}$	—

Table 2.4: The data in the table corresponds to the wavelengths at which the peaks occur in the extinction plots in Figures 2.31 and 2.30.

This can be seen in the paper ref. [23], where similar devices are studied and a post-imaging of the device after illumination is carried out, see Figure 2.32.

This process can be simulated by keeping the points where the triangle meets the connecting wire fixed and by making the triangle vertex position closer to the connecting wire, as in Figure 2.33 for the 280 nm geometry.

The tip length is decreases in the following range: $[-5\text{nm}, -20\text{nm}]$, with step of 2.5 nm. The results of this shrinkage are shown in Figures 2.34, 2.36, 2.38, 2.35, 2.37 and 2.39. It can be seen that the tip-mode peak shifts to higher frequencies for shorter tips in the extinction plot; the same happens for the main peak of FE.

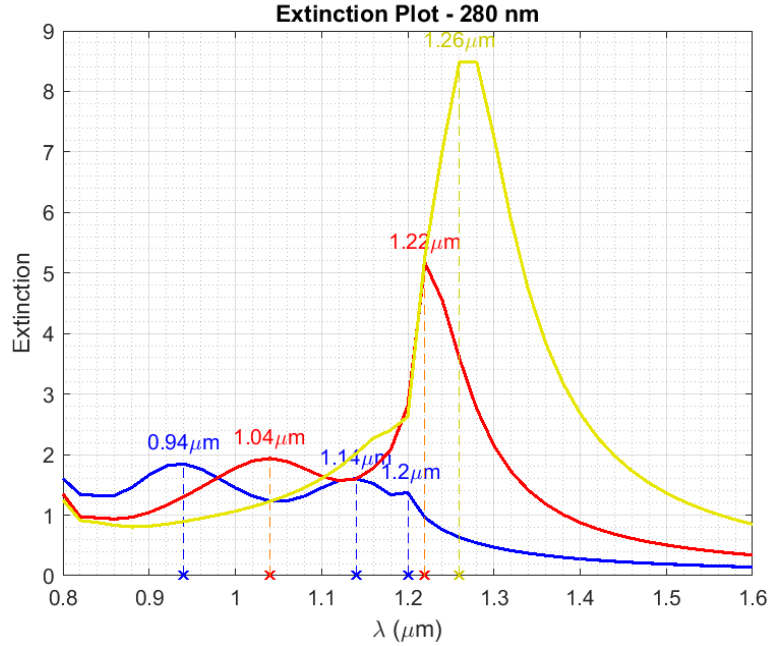


Figure 2.31: Extinction plots for all the considered geometries, as listed in Table 2.3. The yellow curve corresponds to the 280nm geometry, the red one to the 240 nm geometry and the blue one to the 200 nm geometry.

This trend shows the dependence of the tip-mode peak on the tip dimensions.

Final geometry tuning

The understanding of the dependence on the position of the connecting wire and on the tip dimension can help tune the geometry in order to obtain the desired extinction and field enhancement plots and, in this case, it helps matching the experimental results. In order to apply this method, the geometry that has the tip-mode peak matching to the experimental one is chosen and then the connecting wire position is tweaked, in order to shift the wire-mode peak. The geometry chosen from the ones with shrunk tips are: no shrinking for the 200 nm geometry, -7.5 nm shrinking for the 240 nm geometry and -20 nm for the 280 nm one. The wire position "*wire_x*", as originally measured and reported in Table 2.1, are: ~ 100 nm for the 200 nm geometry, ~ 132 nm for the 240 nm one and ~ 147 nm for the 280 nm one. The results of the "*wire_x*" tweaking are reported in Tables 2.8 and 2.9.

As might be seen in these tables, the wire position tweaking helped in finding the optimal device dimensions for the 200 nm geometry, where the "*wire_x*" = 107

Extinction	<i>wire_x</i>	tip-mode peak	wire-mode peak	other peaks
200 nm experimental		$\sim 0.98 \mu\text{m}$	$\sim 1.12 \mu\text{m}$	$\sim 1.09 \mu\text{m}$
200 nm	-5%	$0.92 \mu\text{m}$	$1.2 \mu\text{m}$	$1.16 \mu\text{m}$
200 nm	0%	$0.94 \mu\text{m}$	$1.2 \mu\text{m}$	$1.14 \mu\text{m}$
200 nm	+5%	$0.94 \mu\text{m}$	$1.2 \mu\text{m}$	$1.10 \mu\text{m}$
240 nm experimental		$\sim 1.03 \mu\text{m}$	$\sim 1.15 \mu\text{m}$	—
240 nm	-5%	$1.02 \mu\text{m}$	$1.26 \mu\text{m}$	—
240 nm	0%	$1.04 \mu\text{m}$	$1.22 \mu\text{m}$	—
240 nm	+5%	$1.06 \mu\text{m}$	$1.22 \mu\text{m}$	—
280 nm experimental		$\sim 1.01 \mu\text{m}$	$\sim 1.19 \mu\text{m}$	—
280 nm	-5%	$1.16 \mu\text{m}$	$1.3 \mu\text{m}$	—
280 nm	-2.5%	—	$1.28 \mu\text{m}$	—
280 nm	0%	—	$1.26 \mu\text{m}$	—
280 nm	+2.5%	—	$1.26 \mu\text{m}$	—
280 nm	+5%	—	$1.24 \mu\text{m}$	—

Table 2.5: The data in the table corresponds to the wavelengths at which the peaks occur in the extinction plots for all of the considered geometries, for different values of the parameter "*wire_x*".

nm configuration has peaks that best match the experimental ones, but not for the 240 nm and 280 nm geometries, where the optimal peak position is given by the original "*wire_x*" value.

Another phenomenon that needs to be taken into account is the generation of Wood-Rayleigh anomalies. Wood-Rayleigh anomalies, as explained in paper ref. [44], are "caused by the excitation of the surface electromagnetic waves supported by a periodically corrugated perfectly conducting surface". These excitations are a common feature of gratings and generally cause very sharp dips in power transmission, hence spikes in the extinction plot. These are different than wire modes, which are given by plasmonic resonances, but can maybe couple to them if the resonance frequencies are similar. An example of possible anomalies in the extinction plots that are reported in this thesis can be seen in Figure 2.34, where the wire-mode peak presents two sharp peaks. In particular, the resonance at $\lambda = 1.2 \mu\text{m}$ can also be seen in the relative FE in figure 2.35. This may show that a resonance of the whole device occurs at that particular frequency. These particular anomalies cannot be observed with the experimental setup, because the laser spot interacts with a small amount of devices and fabrication doesn't allow for perfect periodicity. On the other hand, these anomalies may show up in simulation, because large incident plane-waves and a high quality periodicity are assumed. Furthermore, since these

Field enhancement	<i>wire_x</i>	main peak	secondary peak
200 nm experimental		$\sim 1.07 \mu\text{m}$	$\sim 1.35 \mu\text{m}$
200 nm	-5%	$0.94 \mu\text{m}$	$1.2 \mu\text{m}$
200 nm	0%	$0.96 \mu\text{m}$	$1.2 \mu\text{m}$
200 nm	+5%	$0.98 \mu\text{m}$	$1.2 \mu\text{m}$
240 nm experimental		$\sim 1.11 \mu\text{m}$	$\sim 1.35 \mu\text{m}$
240 nm	-5%	$1.02 \mu\text{m}$	$1.26 \mu\text{m}$
240 nm	0%	$1.04 \mu\text{m}$	$1.22 \mu\text{m}$
240 nm	+5%	$1.06 \mu\text{m}$	$1.22 \mu\text{m}$
280 nm experimental		$\sim 1.19 \mu\text{m}$	—
280 nm	-5%	$1.14 \mu\text{m}$	$1.38 \mu\text{m}$
280 nm	-2.5%	$1.16 \mu\text{m}$	$1.36 \mu\text{m}$
280 nm	0%	$1.16 \mu\text{m}$	$1.32 \mu\text{m}$
280 nm	+2.5%	$1.16 \mu\text{m}$	$1.3 \mu\text{m}$
280 nm	+5%	$1.18 \mu\text{m}$	$1.28 \mu\text{m}$

Table 2.6: The data in the table corresponds to the wavelengths at which the peaks occur in the field enhancement plots for all of the considered geometries, for different values of the parameter "*wire_x*".

Extinction	<i>wire_x</i>	height	tip-mode peak	wire-mode peak
280 nm exp.			$\sim 1.01 \mu\text{m}$	$\sim 1.19 \mu\text{m}$
280 nm	-5%	-5%	$1.08 \mu\text{m}$	$1.3 \mu\text{m}$
280 nm	-5%	-2.5%	$1.12 \mu\text{m}$	$1.3 \mu\text{m}$

Table 2.7: The data in the table corresponds to the wavelengths at which the peaks occur in the extinction plots for the 280 nm geometry as listed in Table 2.3, for different values of the parameter "*wire_x*" and of the height of the triangle.

peaks are really narrow-band in frequency, they produce weak alterations of the time-domain response that does not impair the device function (in particular, they produce small ripples in the pulse pedestal, which do not affect the pulse main features).

Concluding, the final geometries that are considered for the comparison to the experimental results are the ones obtained by the averaged measures, as in Table 2.1, with the tip and "*wire_x*" corrections, as listed in Table 2.10.

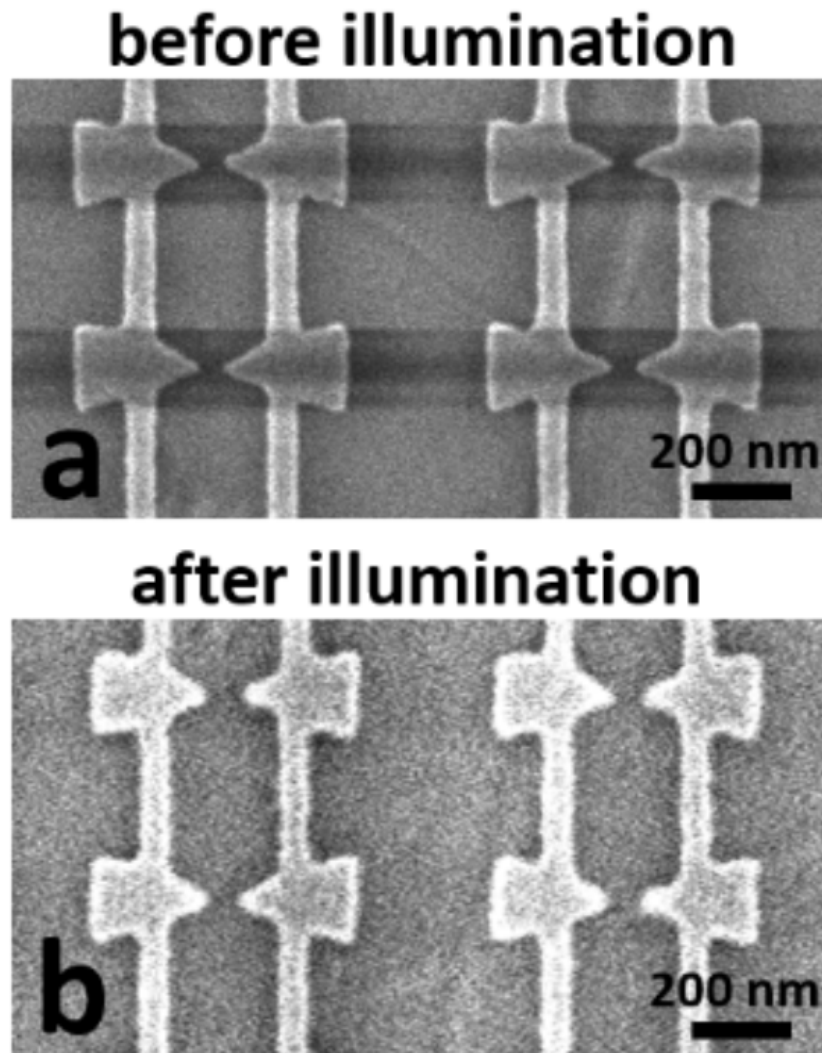


Figure 2.32: SEM image of the bow-tie nanoantennas, fabricated by the QNN Group, as in ref. [23]. In particular, the image shows the bow-tie antennas before and after being illuminated, in order to highlight the presence of laser-induced reshaping.

Final geometries plots

The resulting plots for the 3 final geometries are reported in this subsection. The resulting extinction plot for the 240 nm geometry is shown in Figure 2.40.

The extinction plot in Figure 2.40 shows a tip-mode peak for $\lambda = 1.02 \mu\text{m}$ and a wire-mode peak at $\lambda = 1.24 \mu\text{m}$. This can be seen by looking at the field

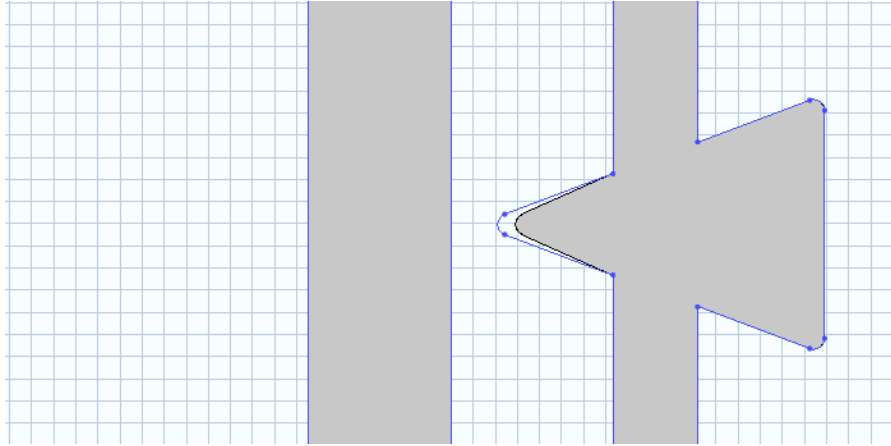


Figure 2.33: An example of how the process of tip shrinking is replicated in the simulation geometries. In particular, this figure shows a -20 nm decrease in the tip length for a 280 nm geometry.

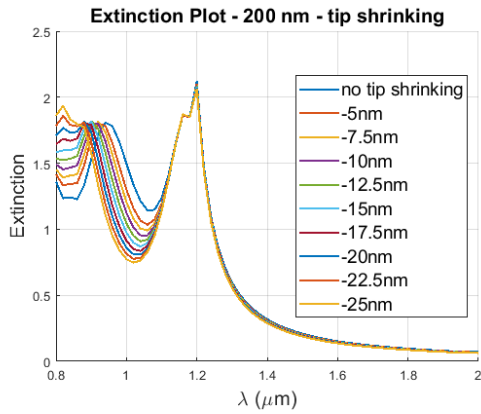


Figure 2.34: Extinction plot for the 200 nm geometry, as listed in Table 2.1, for different values of tip shrinking.

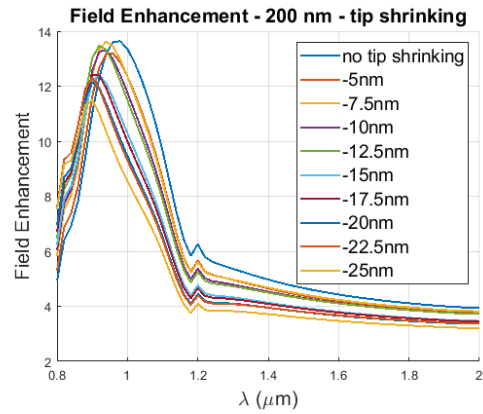


Figure 2.35: Field enhancement plot for the 200 nm geometry, as listed in Table 2.1, for different values of tip shrinking.

distribution in the device for the two frequencies. It is shown in Figures 2.41 and 2.42, respectively.

The field enhancement plot is showed in Figure 2.43.

In the field enhancement figure, one can see a main peak for $\lambda = 1.04 \mu\text{m}$ and a small peak for $\lambda = 1.32 \mu\text{m}$. The field distribution for these two wavelengths are shown in Figures 2.44 and 2.45.

The resulting extinction plot for the 280 nm geometry is shown in Figure 2.46.

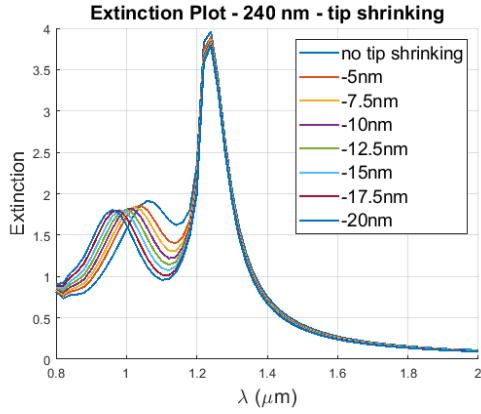


Figure 2.36: Extinction plot for the 240 nm geometry, as listed in Table 2.1, for different values of tip shrinking.

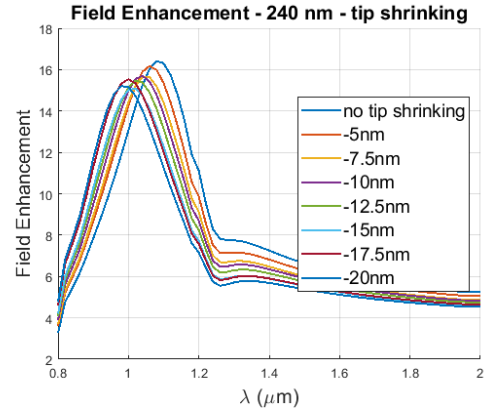


Figure 2.37: Field enhancement plot for the 240 nm geometry, as listed in Table 2.1, for different values of tip shrinking.

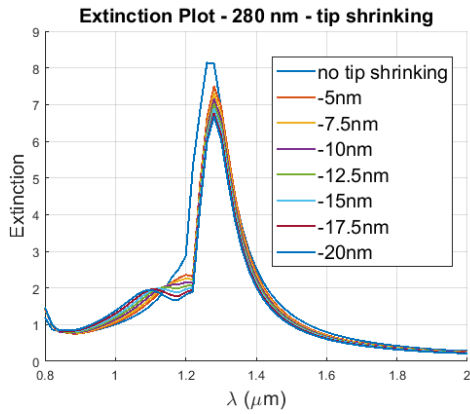


Figure 2.38: Extinction plot for the 280 nm geometry, as listed in Table 2.1, for different values of tip shrinking.

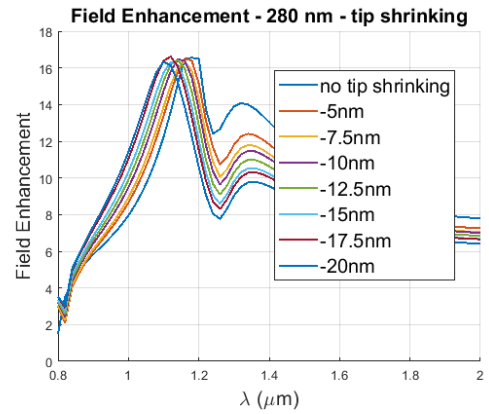


Figure 2.39: Field enhancement plot for the 280 nm geometry, as listed in Table 2.1, for different values of tip shrinking.

The extinction plot in Figure 2.46 shows a tip-mode peak for $\lambda = 1.1 \mu\text{m}$ and a wire-mode peak at $\lambda = 1.28 \mu\text{m}$. This can be seen by looking at the field distribution in the device for the two frequencies. It is shown in Figures 2.47 and 2.48, respectively.

The field enhancement plot is showed in Figure 2.49.

Extinction	<i>wire_x</i>	tip-mode peak	wire-mode peak	other peaks
200 nm experimental		$\sim 0.98 \mu\text{m}$	$\sim 1.12 \mu\text{m}$	$\sim 1.09 \mu\text{m}$
200 nm	93 nm	$0.92 \mu\text{m}$	—	—
200 nm	$\sim 100 \text{ nm}$	$0.94 \mu\text{m}$	$1.16 \mu\text{m}$	$0.84 \mu\text{m}$
200 nm	107 nm	$0.96 \mu\text{m}$	$1.14 \mu\text{m}$	$0.84 \mu\text{m}$
200 nm	115 nm	$0.96 \mu\text{m}$	—	—
240 nm experimental		$\sim 1.03 \mu\text{m}$	$\sim 1.15 \mu\text{m}$	—
240 nm	122 nm	$0.98 \mu\text{m}$	$1.28 \mu\text{m}$	—
240 nm	$\sim 132 \text{ nm}$	$1.02 \mu\text{m}$	$1.24 \mu\text{m}$	—
240 nm	145 nm	$1.08 \mu\text{m}$	$1.2 \mu\text{m}$	—
240 nm	160 nm	$1.06 \mu\text{m}$	$1.2 \mu\text{m}$	$1.16 \mu\text{m}$
280 nm experimental		$\sim 1.01 \mu\text{m}$	$\sim 1.19 \mu\text{m}$	—
280 nm	140 nm	$1.12 \mu\text{m}$	$1.24 \mu\text{m}$	$1.2 \mu\text{m}$
280 nm	$\sim 147 \text{ nm}$	$1.1 \mu\text{m}$	$1.28 \mu\text{m}$	$1.2 \mu\text{m}$
280 nm	155 nm	$1.12 \mu\text{m}$	$1.24 \mu\text{m}$	$.2\mu\text{m}$
280 nm	160 nm	—	$1.24 \mu\text{m}$	$1.2 \mu\text{m}$

Table 2.8: The data in the table corresponds to the wavelengths at which the peaks occur in the extinction plots for all of the considered geometries, for different values of the parameter "*wire_x*".

In the field enhancement figure, one can see a main peak for $\lambda = 1.1 \mu\text{m}$ and a peak for $\lambda = 1.36 \mu\text{m}$. The field distribution for these two wavelengths are shown in Figures 2.47 and 2.50.

The resulting extinction plot for the 200 nm geometry is shown in Figure 2.51.

The extinction plot in Figure 2.51 shows a tip-mode peak for $\lambda = 0.94 \mu\text{m}$ and a wire-mode peak at $\lambda = 1.2 \mu\text{m}$ and a small peak at $\lambda = 0.84 \mu\text{m}$ and one at $\lambda = 1.16 \mu\text{m}$. This can be seen by looking at the field distribution in the device for the two main peaks. It is shown in Figures 2.52 and 2.53, respectively. The two small peaks are just a slight increase in the power absorption and the one at $1.16 \mu\text{m}$ still represents a wire-mode, as can be seen in Figure 2.54.

The field enhancement plot is showed in Figure 2.55.

In the field enhancement figure, one can see a main peak for $\lambda = 0.98 \mu\text{m}$ and a small peak for $\lambda = 1.2 \mu\text{m}$. The field distribution for these two wavelengths are shown in Figures 2.56 and 2.53.

2.2.3 Numerical/experimental results comparison

As a final comparison, the experimental and the simulated extinction plots are reported respectively in Figures 2.57 and 2.58. The wavelength ranges are made

Field enhancement	<i>wire_x</i>	main peak	secondary peak
200 nm experimental		$\sim 1.07 \mu\text{m}$	$\sim 1.35 \mu\text{m}$
200 nm	93 nm	$0.94 \mu\text{m}$	$1.3 \mu\text{m}$
200 nm	$\sim 100 \text{ nm}$	$0.98 \mu\text{m}$	$1.2 \mu\text{m}$
200 nm	107 nm	$1 \mu\text{m}$	$1.2 \mu\text{m}$
200 nm	115 nm	$1 \mu\text{m}$	$1.2 \mu\text{m}$
240 nm experimental		$\sim 1.11 \mu\text{m}$	$\sim 1.35 \mu\text{m}$
240 nm	122 nm	$1.1 \mu\text{m}$	$1.4 \mu\text{m}$
240 nm	$\sim 132 \text{ nm}$	$1.04 \mu\text{m}$	$1.32 \mu\text{m}$
240 nm	145 nm	$1.1 \mu\text{m}$	—
240 nm	160 nm	—	$1.2 \mu\text{m}$
280 nm experimental		$\sim 1.19 \mu\text{m}$	—
280 nm	140 nm	$1.08 \mu\text{m}$	$1.4 \mu\text{m}$
280 nm	$\sim 147 \text{ nm}$	$1.1 \mu\text{m}$	$1.36 \mu\text{m}$
280 nm	155 nm	$1.12 \mu\text{m}$	$1.3 \mu\text{m}$
280 nm	160 nm	$1.14 \mu\text{m}$	$1.26 \mu\text{m}$

Table 2.9: The data in the table corresponds to the wavelengths at which the peaks occur in the field enhancement plots for all of the considered geometries, for different values of the parameter "*wire_x*".

Geometries	200 nm	240 nm	280 nm
tip shrinking	—	-7.5 nm	-20 nm
<i>wire_x</i>	107 nm	132 nm	147 nm

Table 2.10: Final considered geometries dimensions. The reported data corresponds to corrections to the values in Table 2.1.

the same, for sake of simplicity.

Different features can be noticed in this comparison. First of all, the experimental extinction shows a noisy behaviour in the $[900\text{nm}, 950\text{nm}]$ range; this is a feature given by the incident laser spectrum. Secondly, the wire-mode peak intensities in the simulated results increases with increasing triangle height. This is due partially to the fact that for larger triangles a larger power absorption occurs and hence a larger dip in power transmission is observable. Furthermore, this may be due to material properties; indeed, material properties depend on illumination frequency and they lead to stronger resonances at larger wavelengths. Concluding, the wavelengths at which these peaks can be observed do not match perfectly the experimental ones, but the numerical results show the tip-mode and wire-mode features in the device extinction plot that are characteristic of these devices, as seen in the experimental

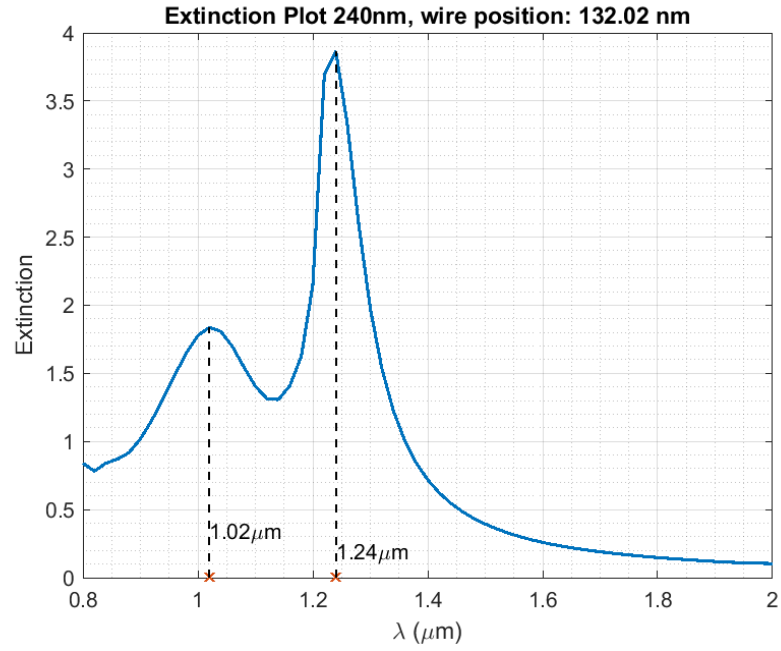


Figure 2.40: Extinction plot for the 240 nm geometry, as listed in Table 2.10.

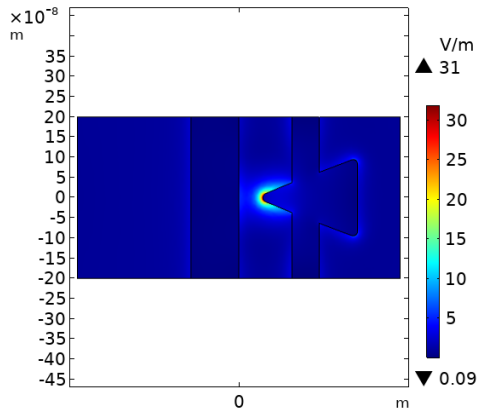


Figure 2.41: Field distribution at the wavelength corresponding to the tip-mode in the extinction plot for the 240 nm geometry, as listed in Table 2.10.

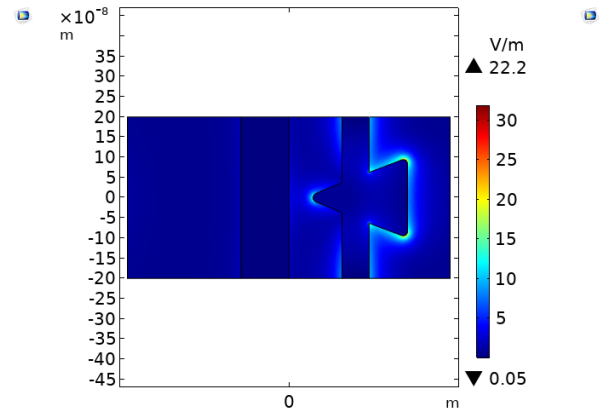


Figure 2.42: Field distribution at the wavelength corresponding to the wire-mode in the extinction plot for the 240 nm geometry, as listed in Table 2.10.

results. The mismatch in wavelength may be due to the presence in the fabricated device of small features given by fabrication imperfections that are hard to replicate in a CAD simulation; furthermore it may be due also to the fact that the fabricated

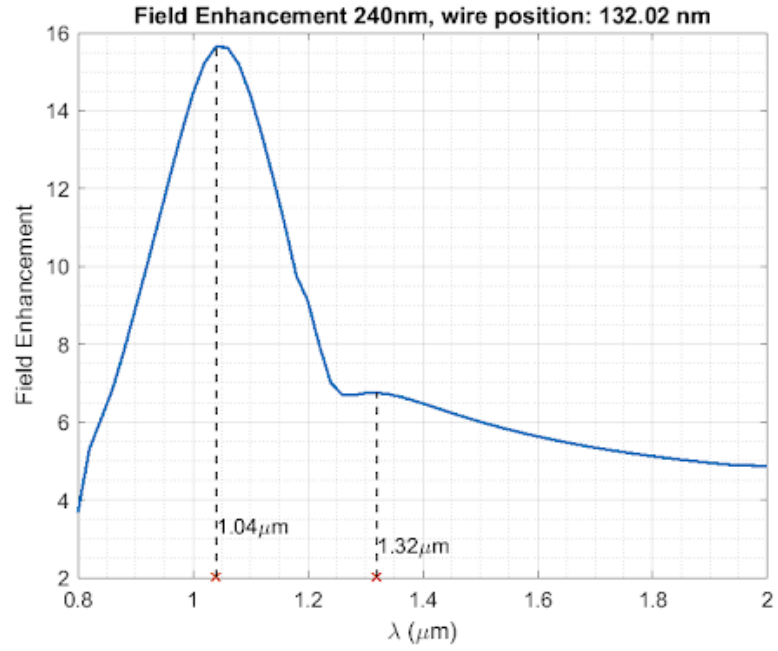


Figure 2.43: Field enhancement plot for the 240 nm geometry, as listed in Table 2.10.

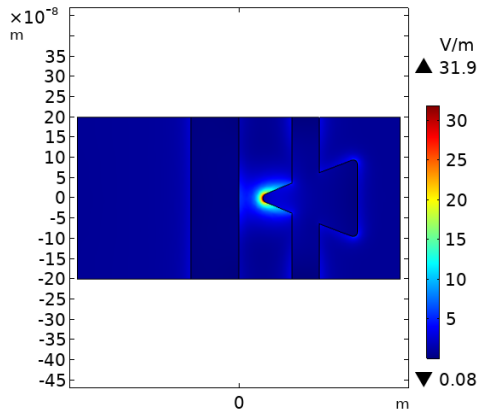


Figure 2.44: Field distribution at the wavelength corresponding to the main peak in the field enhancement plot for the 240 nm geometry, as listed in Table 2.10.

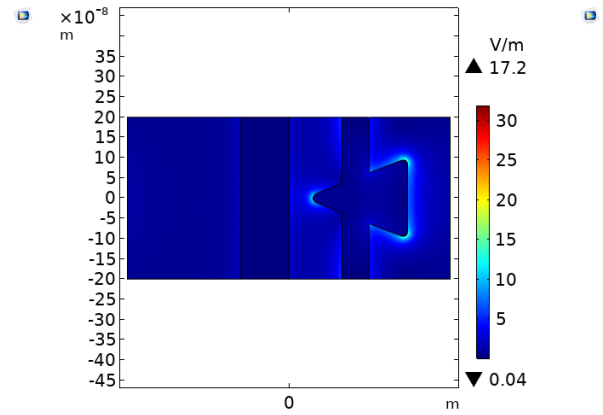


Figure 2.45: Field distribution at the wavelength corresponding to the secondary peak in the field enhancement plot for the 240 nm geometry, as listed in Table 2.10.

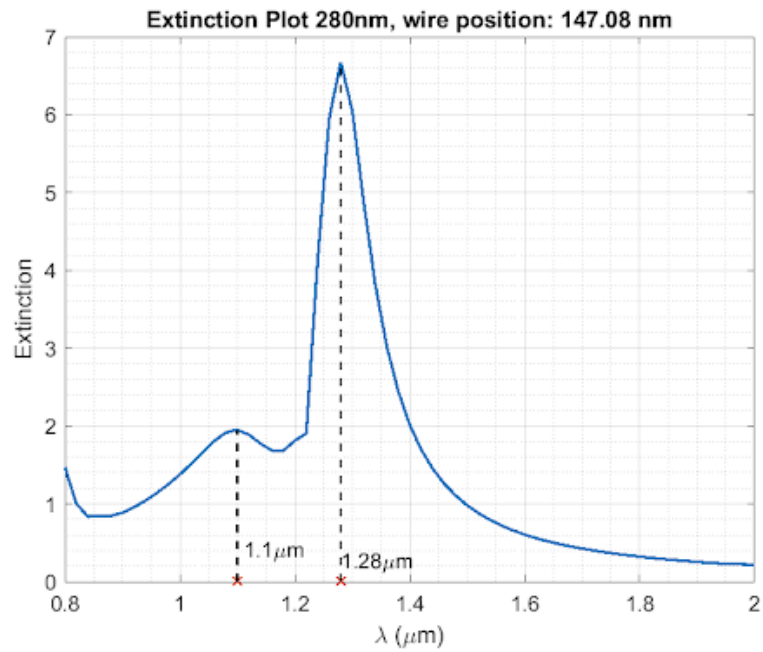


Figure 2.46: Extinction plot for the 280 nm geometry, as listed in Table 2.10.

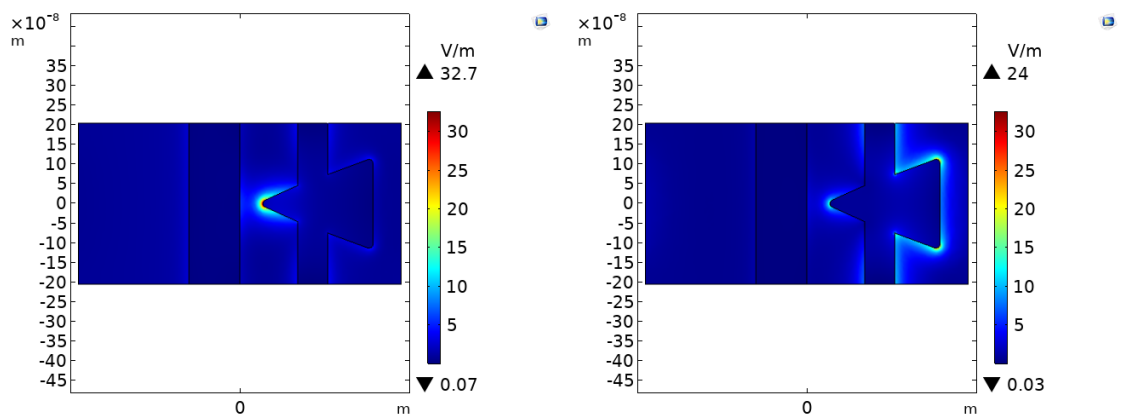


Figure 2.47: Field distribution at the wavelength corresponding to the tip-mode in the extinction plot for the 280 nm geometry, as listed in Table 2.10.

Figure 2.48: Field distribution at the wavelength corresponding to the wire-mode in the extinction plot for the 280 nm geometry, as listed in Table 2.10.

nanostructures do not all have the same exact dimensions and features, whereas the simulation cell duplicates one geometry indefinitely.

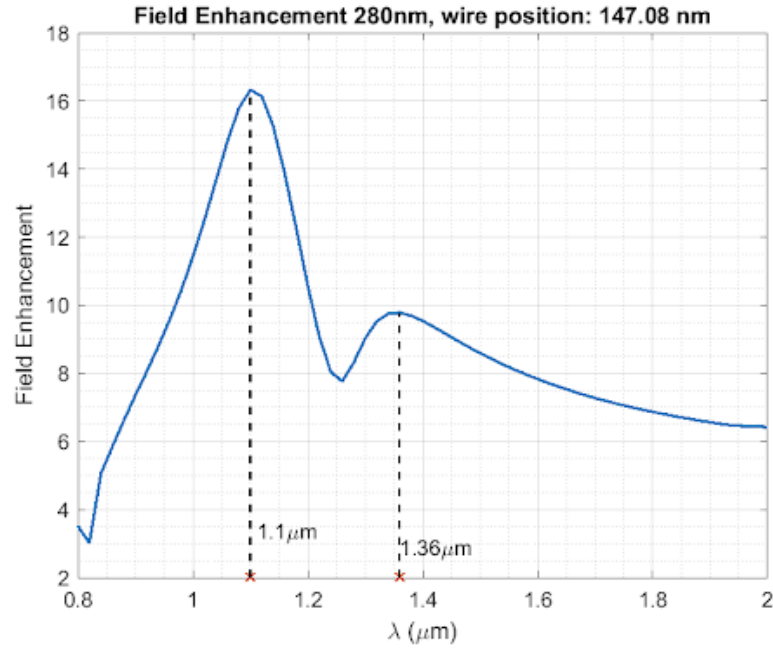


Figure 2.49: Field enhancement plot for the 280 nm geometry, as listed in Table 2.10.

2.3 Conclusions

In this Chapter, the frequency response of free-space plasmonic nanoantennas for field sampling is successfully simulated. In particular, the results show a rather good matching with experimental results for all three of the considered geometries. The excitation of plasmonic resonances is predicted in the near IR region (at wavelengths in the range $[1, 1.3] \mu\text{m}$) through power transmission and extinction studies and a field enhancement up to ~ 16 is observed at the antennas tips, for $\lambda \sim 1 \mu\text{m}$. Throughout the analysis, the simulated geometry is gradually adjusted in order to take into account the laser-induced reshaping phenomenon that the fabricated devices undergo during illumination and hence to better replicate the experimental results. The device simulation verified the experimental results, so the electromagnetic response of the fabricated antennas can be trusted for optical field sampling. Hence the fabricated devices are subsequently utilized by the QNN group for low-energy, near-infrared, arbitrary waveforms field sampling, ref. [24]. This field sampling device can allow for important applications such as precise attosecond metrology, studies on strong-field light-matter interaction and time-domain spectroscopy of molecular fingerprints. In particular, the devices studied in this work are on-chip (so compact and integrated) and work in ambient conditions.

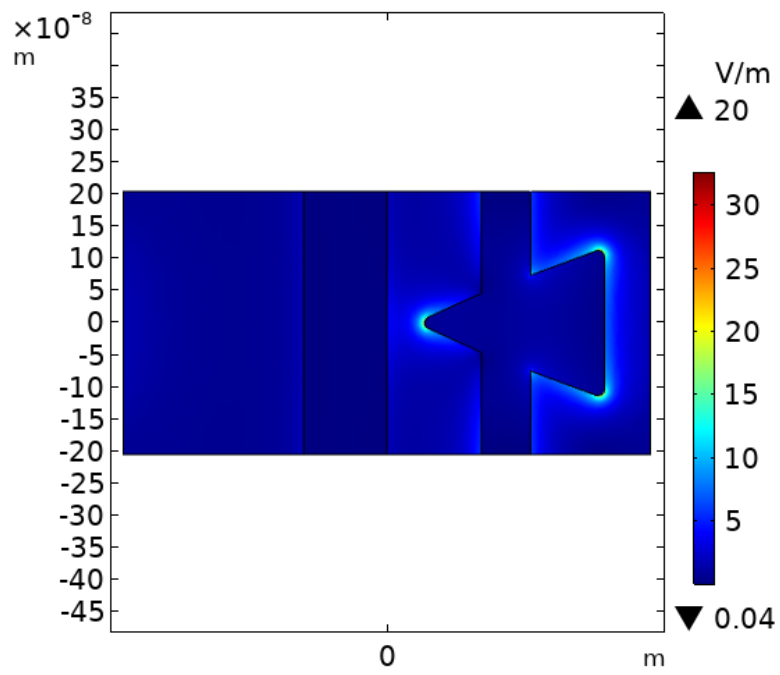


Figure 2.50: Field distribution at the wavelength corresponding to the secondary peak in the field enhancement plot for the 280 nm geometry, as listed in Table 2.10.

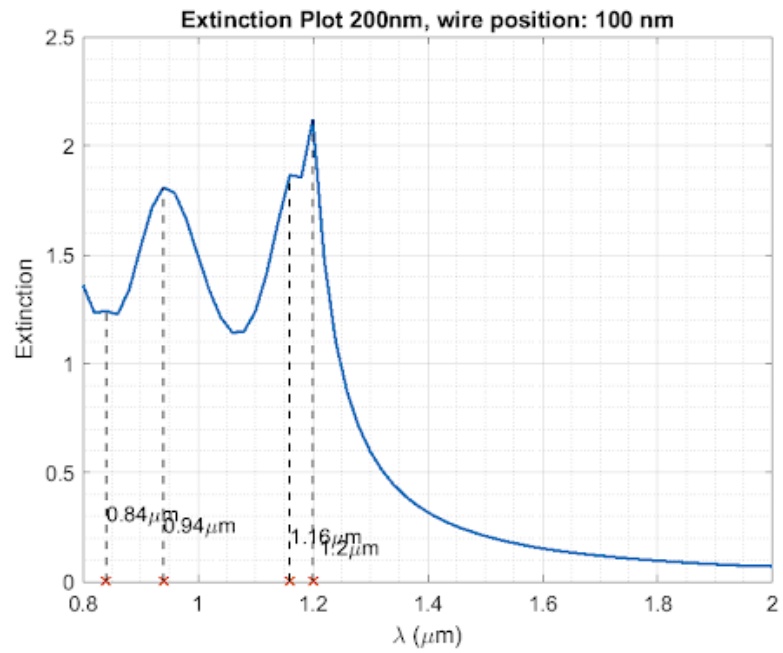


Figure 2.51: Extinction plot for the 200 nm geometry, as listed in Table 2.10.

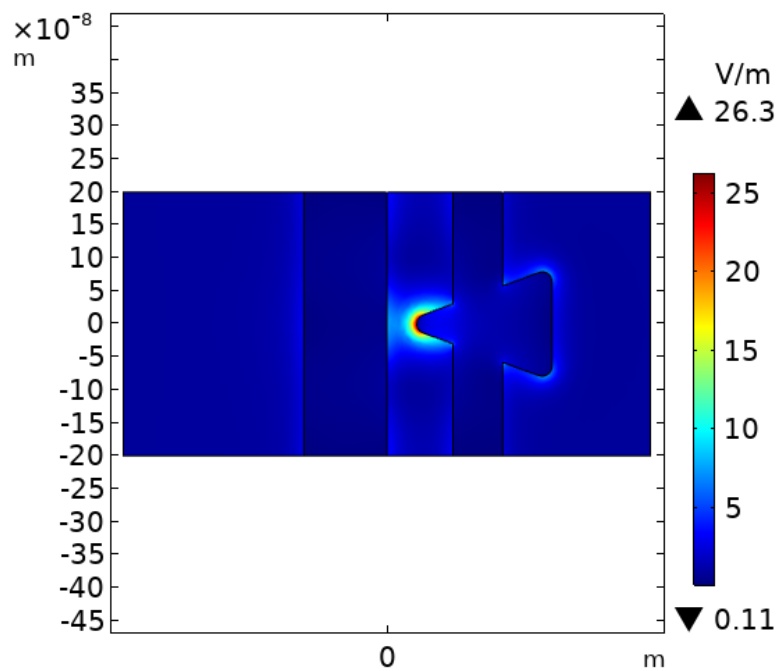


Figure 2.52: Field distribution at the wavelength corresponding to the tip-mode in the extinction plot for the 200 nm geometry, as listed in Table 2.10.

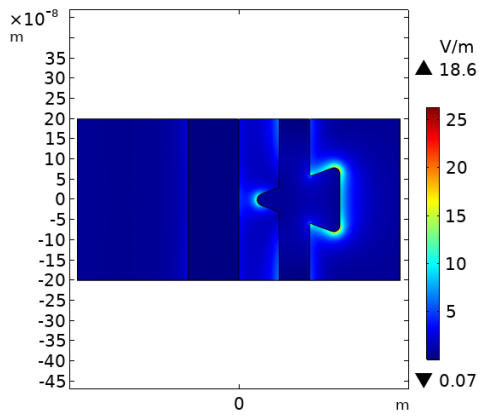


Figure 2.53: Field distribution at the wavelength corresponding to the wire-mode in the extinction plot for the 200 nm geometry, as listed in Table 2.10.

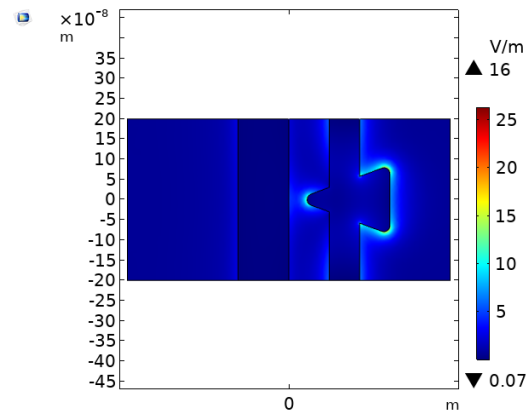


Figure 2.54: Field distribution at the wavelength corresponding to the wire-mode in the extinction plot for the 200 nm geometry, as listed in Table 2.10.

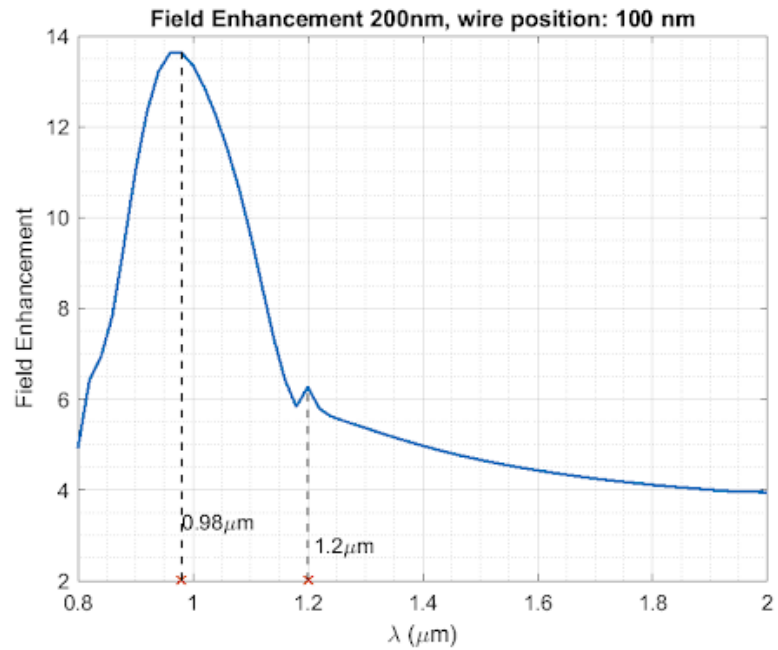


Figure 2.55: Field enhancement plot for the 200 nm geometry, as listed in Table 2.10.

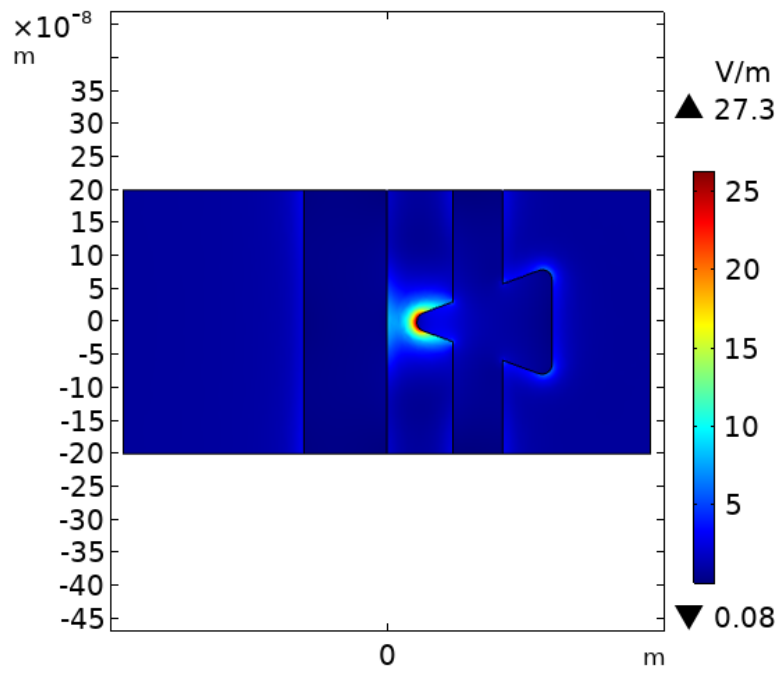


Figure 2.56: Field distribution at the wavelength corresponding to the main peak in the field enhancement plot for the 200 nm geometry, as listed in Table 2.10.

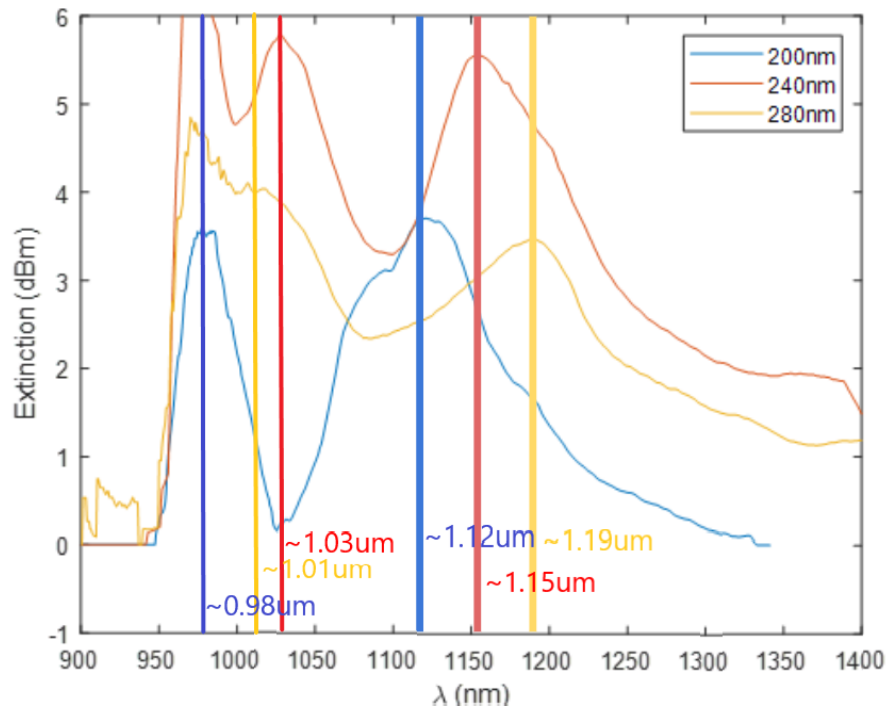


Figure 2.57: Experimental extinction plot for the devices fabricated by the QNN group and that are shown in the SEM images in Figures 2.4, 2.5 and 2.6. The vertical coloured lines serve the purpose of indicating the peaks wavelengths.

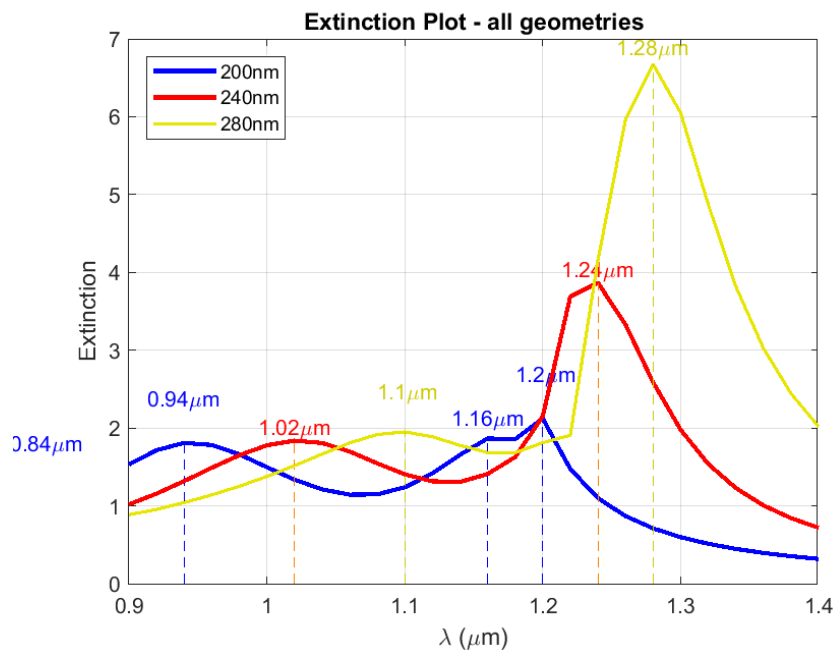


Figure 2.58: Extinction plots for all the considered geometries, as listed in Table 2.10.

Chapter 3

Waveguide-integrated bow-tie nanonantennas for CEP detection

The second device configuration that is simulated and analysed in this thesis is the CEP detector. As explained in the Introduction, the carrier-envelope phase (CEP) is a feature of optical pulses or waveforms that describes the offset between the peak of the electric field carrier wave and the peak of the pulse envelope. CEP defines the exact optical waveform of a pulse and is then fundamental for strong-field light–matter interactions, since in this regime the interactions depend on the instantaneous electric field value rather than on the intensity envelope of the pulse. Furthermore, in frequency-comb optical sources, ref. [8], it is fundamental to stabilize the carrier-envelope offset frequency (f_{CEO}), that is the frequency at which the CEP changes from one generated peak to the next and it is important for applications like optical frequency synthesis, ref. [9] and [10] and attosecond pulse generation, ref. [11]. As a future application, precisely controlled CEP can lead to ultrafast information processing, thanks to lightwave-based petahertz electronics, ref [12]. Indeed, carrier dynamics manipulation due to ultrafast field waveforms occurs at subfemtosecond time scales and is dominated by the CEP value. Finally, CEP is important in the attosecond metrology for microscopy, ref. [13], [14] and [15].

In the past, CEP detection was achieved with both frequency-domain interferometric techniques, see ref. [10], [16] and [17], and time-domain photoelectron emission, see ref. [18], [19] and [20]. These techniques require either interferometry within complex optical systems or vacuum apparatuses and high energy pulses, whereas the device studied in this work is a compact and integrable solid state detector working in ambient conditions. Time-domain CEP detection in solid state

devices is demonstrated in several papers, as shown in ref. [21], [22] and [23], which make the basis of this work.

In both the field sampler and the CEP detector configurations, the optical wave-form that is to be analysed is delivered to the devices as a free-space wave. Since pulse sources are going towards being completely integrated and optical signals are mainly delivered by waveguides, a need for waveguide-integrated CEP detectors and field samplers for potential operation within integrated photonics platforms arose. Furthermore fully integrated devices have a small foot-print. For these reasons, in this Chapter the antennas will be integrated on top of a waveguide and coupled to waveguide modes. In particular, the design is optimized for CEP detection, but can be easily corrected for field sampling. The antennas configuration for CEP detection is the bow-tie structure, as shown in Figure 3.1.

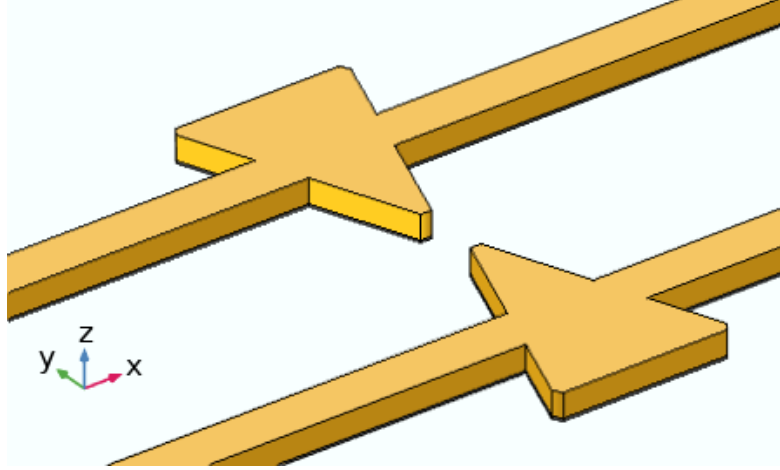


Figure 3.1: Bow-tie antennas configuration. No scale is present but the triangle height is 200 nm. The 20 nm Au nanostructures are represented in yellow, the 2 nm Cr adhesion layer is black and the SiN waveguide core is light blue / white. The waveguide SiO₂ cladding is not represented in this figure.

Throughout this Chapter, first of all, it is verified that the numerical and the analytical calculations for a simple rectangular and slab waveguide are matching. Once the accuracy is checked, the nanoantennas are placed on top of a rectangular waveguide core and the device is studied with both a frequency-domain and a time-domain analysis. In particular, the field distribution in the device as a function of frequency is analysed and particularly interesting is the field enhancement at the tips of the antennas. The field distribution gives information about the behaviour of the device, whereas the field enhancement at the tips of the antennas is important

for understanding the evolution of an optical waveform at the antennas tips. Indeed, different frequency components of the waveform will be enhanced according to field enhancement at tips. A time-domain approach studies this transformation of pulses at the antennas and it results in the evaluation of CEP at each antenna. The device is then studied for its losses and power transmission, in order to better engineer the design and signal collection. As a last step, the electron emission is evaluated, according to Fowler-Nordheim tunnelling theory.

3.1 Waveguide numerical simulation vs. analytical method

In order to verify the accuracy of the COMSOL Multiphysics simulator, a comparison between the numerical and analytical results is carried out, for both a rectangular and a slab waveguide. The theoretical analysis on a waveguide can be found in multiple textbooks and in this particular case it is from ref. [45], as shown in the introduction Subsection 1.2.3. The analytical formulas are implemented in a MATLAB script.

3.1.1 Materials, geometry and model setup

The considered materials and geometries are the following. The rectangular waveguide has a ($0.8 \mu\text{m} \times 1 \mu\text{m}$) SiN core and a SiO₂ cladding; the slab waveguide has a $0.5 \mu\text{m}$ -thick SiN core and a SiO₂ cladding. SiN as core material is chosen because few-cycle supercontinuum sources can be generated directly in SiN waveguides, ref. [46].

The simulation is carried out by the COMSOL Multiphysics software. The considered geometries are the same as the theoretical analysis and the cladding thicknesses are $3 \mu\text{m}$ for the rectangular one and $1.75 \mu\text{m}$ for the slab waveguide. Besides, the waveguide is kept very short, $0.2 \mu\text{m}$ for the rectangular one and $0.5 \mu\text{m}$ for the slab one, because the waveguide mode analysis only requires information on the section and materials of the waveguide and not on its length. In the COMSOL model, PML layers (perfectly matched layers, domains that are added along the exterior of the model which absorb all outgoing waves) are added to the whole geometry in order to avoid reflection of the wave at the boundaries back to the device. Then, input and output ports are defined, in order to insert an input monochromatic plane wave, at a power of $1W$. The wave input mode is calculated by the software as the fundamental one for the selected geometry and it is a TM mode for the rectangular waveguide and a TE mode for the slab one. The optical

properties of Au and Cr are taken from ref. [43]. The ones for SiN from ref. [47] and for SiO₂ from ref. [48] and ref. [49].

3.1.2 Results

Both analyses (analytical and numerical) were carried out varying the input wave frequency in a large range: [800, 3000] nm, which is approximately the frequency span that is important for the studied devices. In Figure 3.2 is shown the dispersion relation $\beta(\omega)$, with switched axis in order to make the analysis of phase and group velocity easier.

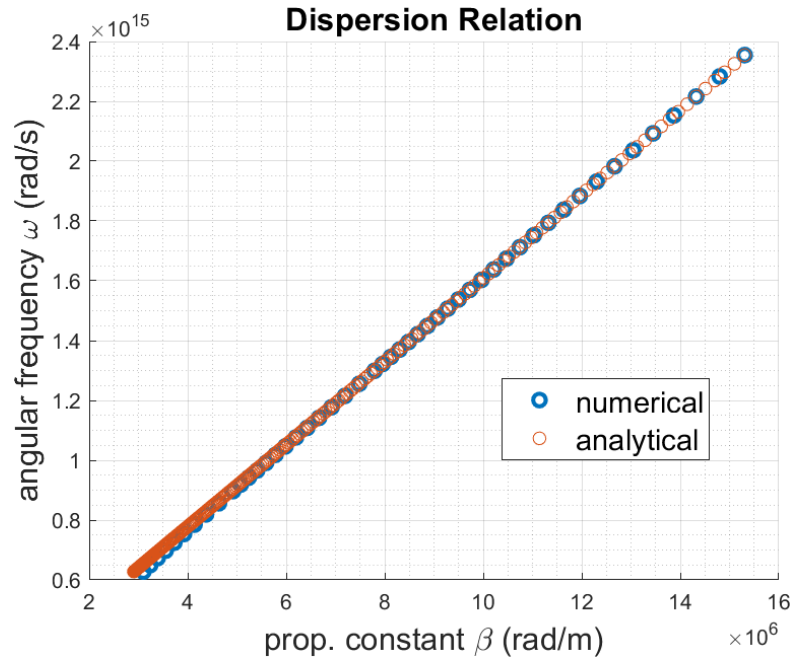


Figure 3.2: Dispersion relation. Comparison between numerical and analytical results for a rectangular waveguide.

One can see that the two methods deliver the same result. Nevertheless, for large wavelengths the two curves start to separate. This is due to the fact that the analytic model is approximated. In particular, the formulas do not describe the corner zones of the waveguide; the ones that are in the cladding, close to the corners of the rectangular core. In fact, for larger wavelengths, the field is less and less confined in the core, so more field is present in these zones, creating the difference that can be observed in the dispersion relation graph. This behaviour can be discerned in all relevant quantities, as can be seen in the following figures, since they all are related to the dispersion relation, as is expressed in the Introduction in

Subsection 1.2.3. In particular, it is important to notice that the studied devices show major features close to the $1.5 \mu\text{m}$ wavelength, well inside the considered range.

Phase and group velocity as a function of frequency are important quantities to study, because they describe the behaviour of the pulse travelling through the waveguide. Figures 3.3 and 3.4 show the phase and group velocities in light velocity units.

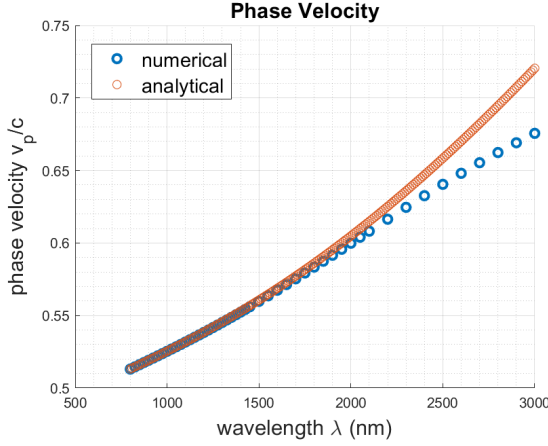


Figure 3.3: Phase velocity. Comparison between numerical and analytical results for a rectangular waveguide.

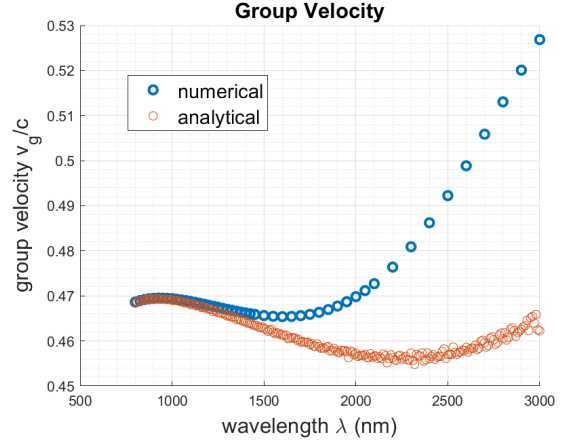


Figure 3.4: Group velocity. Comparison between numerical and analytical results for a rectangular waveguide.

One can observe the same behaviour as in the dispersion relation. This feature is amplified for the group velocity because the derivation operation is carried out. The fact that for high frequencies (so, stronger field confinement and so a more ideal situation) the two analyses converge to the same behaviour is the key factor that confirms the trustworthiness of the simulator.

Further important quantities to be studied are the mode effective index and the possible CEP slippage along the waveguide. The mode effective index can be observed in Figure 3.5.

The CEP slippage per μm travelled in the waveguide ($\Delta CEP_{\mu\text{m}}$), calculated as in formula 1.1, for $l = 1 \mu$, is shown in Figure 3.6. This is an important parameter for a CEP detector design, because it helps predict the distance in the waveguide after which the CEP value shows a 2π circling, so it has the same value as the input signal, the one that is to be measured. This can be estimated from the following formula: $\frac{2\pi}{\Delta CEP_{\mu\text{m}}}$ and it is shown in Figure 3.7:

As one can see, for $\lambda = 1.5 \mu\text{m}$, CEP would undergo a 2π shift in $\sim 4.2 \mu\text{m}$

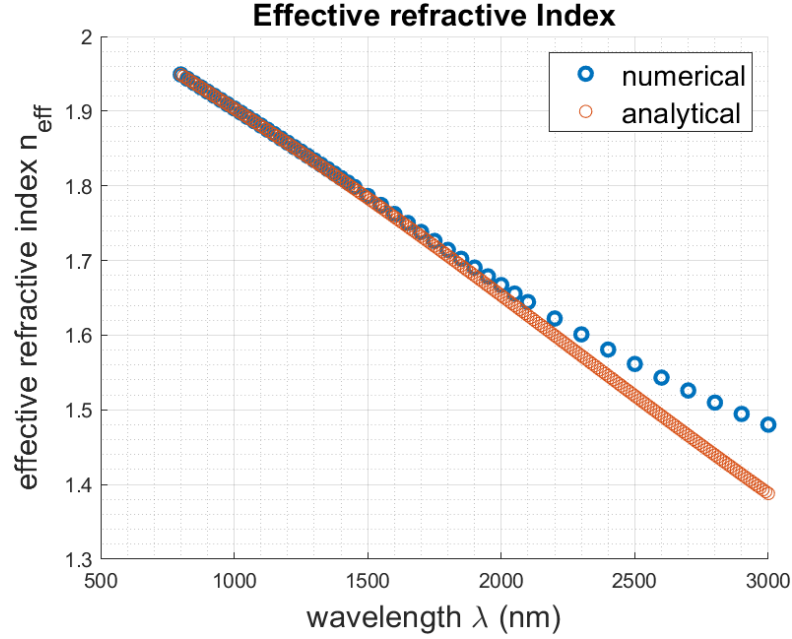


Figure 3.5: Effective refractive index. Comparison between numerical and analytical results for a rectangular waveguide.

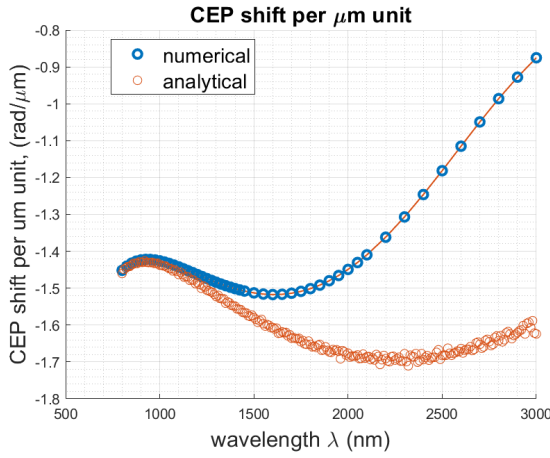


Figure 3.6: CEP shift per μm travelled in the waveguide. Comparison between numerical and analytical results for a rectangular waveguide.

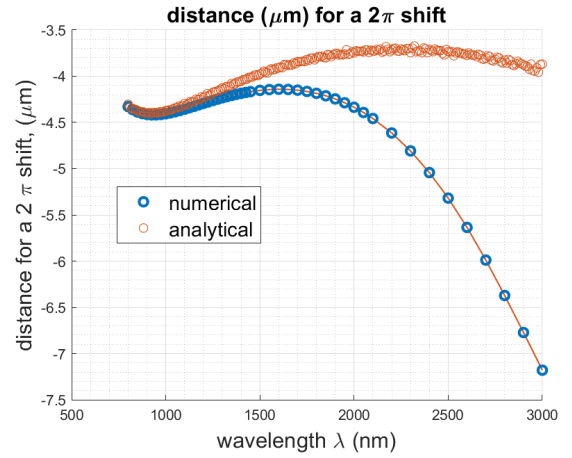


Figure 3.7: Distance in the waveguide after which CEP shifts of 2π . Comparison between numerical and analytical results for a rectangular waveguide.

space in the waveguide. At large wavelengths, the simulated results show that the CEP shifts at a much smaller rate along the waveguide. This may be due to the

fact that what led to a large CEP shifting is the geometry of the waveguide and hence its field confinement. Indeed, for large wavelengths, the confinement is lower and so is the CEP slippage along the waveguide.

The same analysis is done on the slab waveguide. Since the slab waveguide does not have the regions of space where the theory is approximated, the analytic results are expected to be better matching the simulation ones. This is what can be shown in Figures 3.8, 3.9, 3.10, 3.11, 3.12 and 3.13 of the relevant quantities analyzed before.

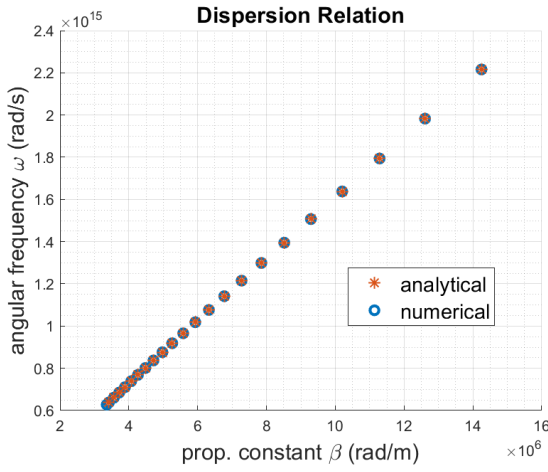


Figure 3.8: Dispersion relation. Comparison between numerical and analytical results for a slab waveguide.

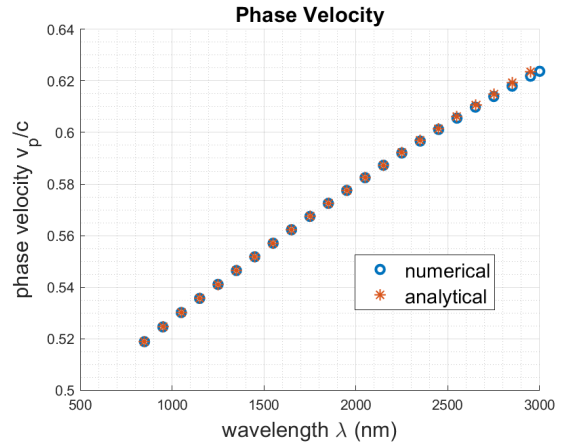


Figure 3.9: Phase velocity. Comparison between numerical and analytical results for a slab waveguide.

As can be noticed, the simulated and analytical results are more similar than it is for the rectangular waveguide case. A slight difference can still be observed for high wavelengths, for the reasons we discussed in the previous case.

This demonstrates that the simulator matches the theoretical behaviour for simple waveguides and additionally makes precise calculations for the portions of space that are usually approximated in the theoretical reasoning.

3.2 Waveguide-integrated bow-tie nanoantennas

Once verified the simulator accuracy, the nanoantennas are placed on top of the core of a rectangular waveguide, as can be seen in Figures 3.14, 3.15 and 3.16.

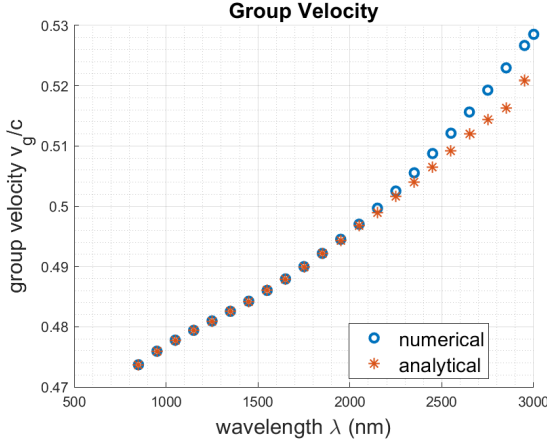


Figure 3.10: Group velocity. Comparison between numerical and analytical results for a slab waveguide.

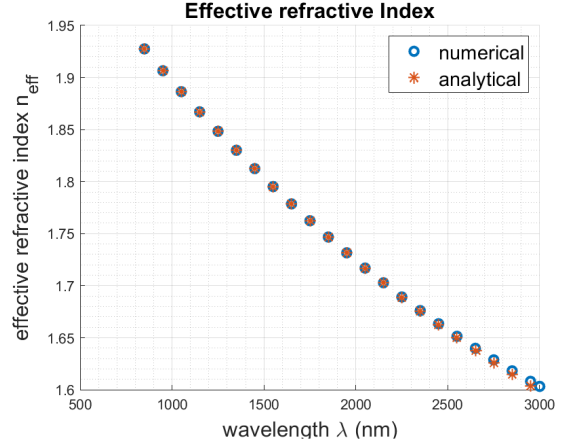


Figure 3.11: Effective refractive index. Comparison between numerical and analytical results for a slab waveguide.

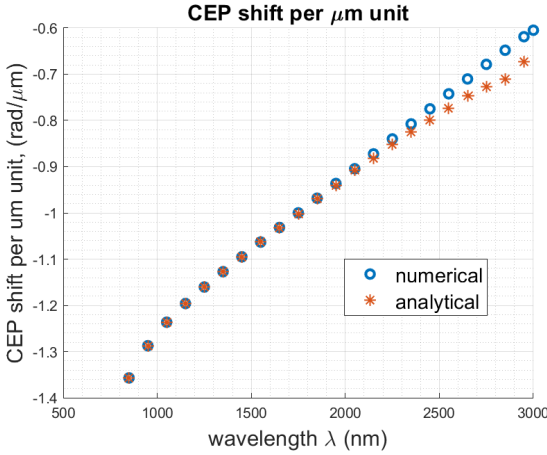


Figure 3.12: CEP shift per μm travelled in the waveguide. Comparison between numerical and analytical results for a slab waveguide.

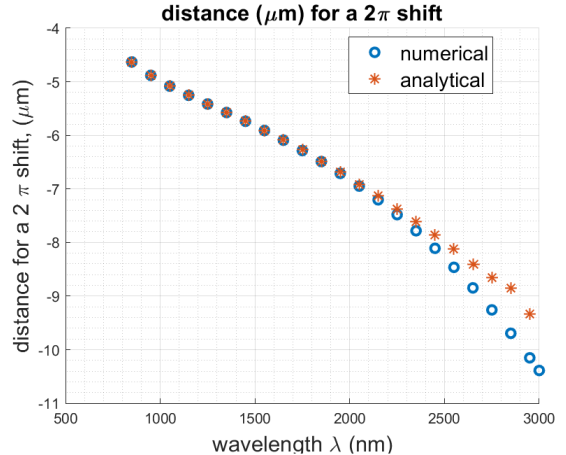


Figure 3.13: Distance in the waveguide after which CEP shifts of 2π . Comparison between numerical and analytical results for a slab waveguide.

This design exploits the fact that the antennas are evanescently coupled to the waveguide, so light will interact with the bow-tie antennas and eventually force electron expulsion from the material, hence generating a detectable electric signal. The signals from all the antennas are then integrated in a single one. In order for this signal to contain information on the CEP of the incident waveform, which

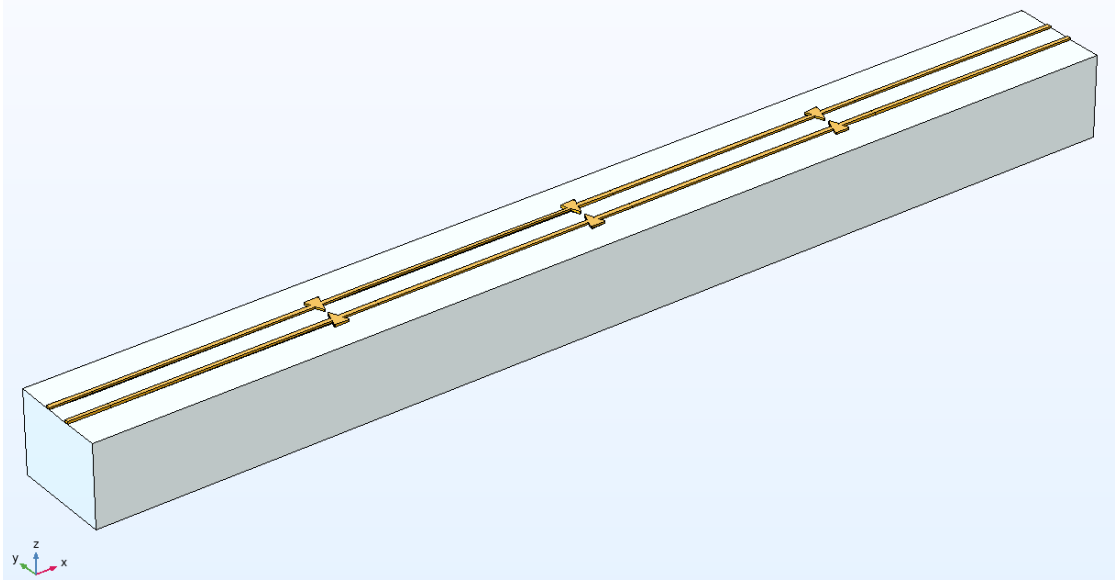


Figure 3.14: 3D COMSOL Multiphysics model for the waveguide-integrated bow-tie nanoantennas. No scale is present but the waveguide core height is 800 nm. The 20 nm Au nanostructures are represented in yellow, the 2 nm Cr adhesion layer is black and the SiN waveguide core is light blue / white. The waveguide SiO₂ cladding is not represented in this figure.

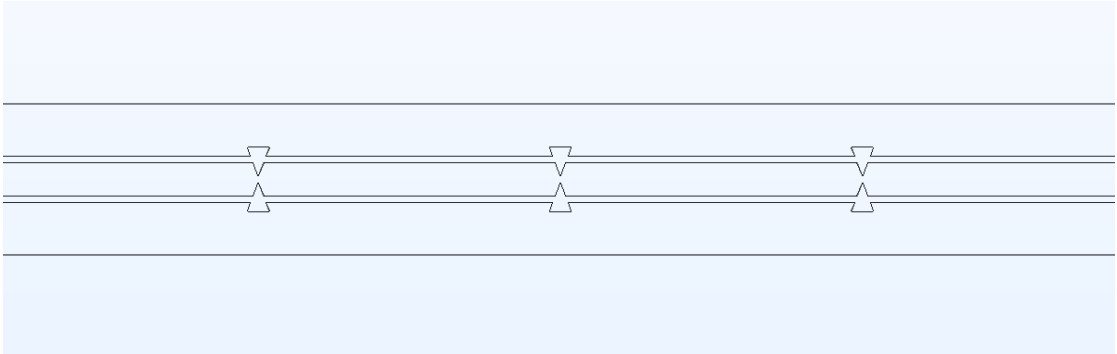


Figure 3.15: Top-view of the simulated model for the waveguide-integrated bow-tie nanoantennas. No scale is present but the triangles height is 200 nm.

is the feature to be detected, the CEP value at each subsequent antenna needs to be the same. This is not trivial, since CEP circles when travelling inside a material, due to a difference in phase and group velocity, as explained in Section 1.2.3. This CEP slippage can be predicted and the antennas are then placed at a certain distance among each other, such that after this distance the CEP has

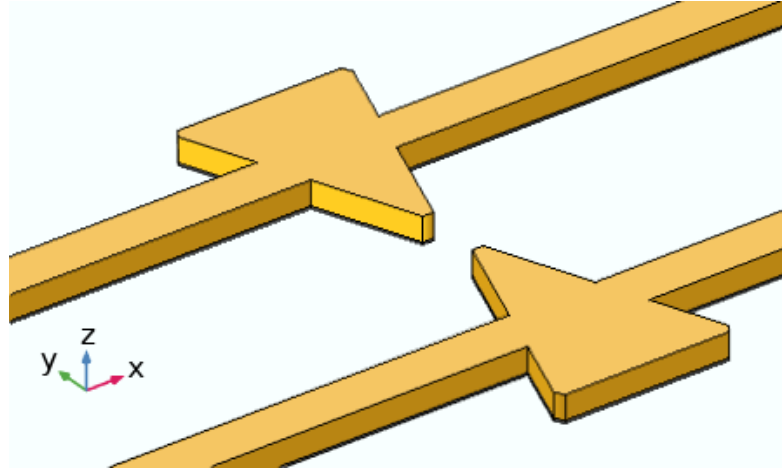


Figure 3.16: Bow-tie antennas configuration. No scale is present but the triangle height is 200 nm. The 20 nm Au nanostructures are represented in yellow, the 2 nm Cr adhesion layer is black and the SiN waveguide core is light blue / white. The waveguide SiO₂ cladding is not represented in this figure.

shifted of an integer multiple of 2π and hence possesses the same value as the CEP of the input waveform. Under these conditions, the signal is called *CEP sensitive* and possesses information on the detected waveform CEP value. In this Chapter, the correct antenna spacing is estimated.

3.2.1 Device structure and simulation setup

The device structure is composed of a ($0.8 \mu\text{m} \times 1 \mu\text{m}$) SiN and ($4 \mu\text{m} \times 4 \mu\text{m}$) SiO₂ cladding rectangular waveguide. On top of the waveguide core a metal structure is present, composed of a 2 nm Cr adhesion layer and a 20 nm Au layer, shaped as two parallel connecting wires with periodic antennas. The antennas configuration is given by two isosceles triangles placed in a bow-tie shape, as in figure 3.16. The connecting wire width is 40 nm; the triangle's base is 150 nm and its height is 200 nm. The connecting wire is placed at 110 nm from the center of the gap between the two triangles. The radius of curvature of the triangle's vertices is set to 5 nm. The gap between the tips is ~ 48 nm. These values were taken from ref. [23], as they are optimized for plasmonic excitation. The optimal spacing between one bow-tie antenna and the next and the number of antennas and subsequently the final total length of the waveguide will be estimated throughout this Chapter.

The type of simulation is the same as the simple waveguide one (COMSOL Multiphysics) and the settings are kept the same (boundary conditions, input/output port, frequency range). The fundamental mode for the waveguide is the TM

(transverse magnetic) mode, with non-zero components: (E_x, E_y, H_z) , according to the axis convention shown in figure 3.14 and 3.16. In particular, the dominant component is the E_y one, which is $\sim 5\times$ the E_x one and $\sim 200\times$ the H_z one. This mode is optimal for the chosen application; indeed, the needed light polarization is in such a way to have the E field directed along the nanotriangles main heights.

3.2.2 Type of analyses

As mentioned before, to achieve CEP sensitivity, the correct spacing between bow-tie antennas along the waveguide is a key factor and it requires the knowledge of the CEP slippage along the waveguide. In order to study the CEP value at each antenna and hence the correct spacing, several analyses are needed.

As a first step, the frequency response of the device is to be studied; which is, the field distribution in the device as a function of frequency and in particular the field enhancement at the tips of the antennas. The field distribution gives information about the behaviour of the device, whereas the field enhancement at the tips of the antennas is important for understanding the evolution of the pulse along the device. Indeed, different frequency components of the pulse will be enhanced according to field enhancement at tips. The study of the transformation of pulses along the device is given by a time-domain approach, which results in the evaluation of CEP at each antenna. The device is then studied for its losses and power transmission, in order to better engineer the design and signal collection. As a last step, the electron emission is evaluated, according to Fowler-Nordheim tunnelling theory.

3.3 Simulation results

3.3.1 Frequency-domain analysis

The considered frequency range is [1000, 2500] nm. This is due to the fact that the device is optimized for an input ultrashort pulse with central wavelength 1550 nm and so the main device properties are observed in this range. The simulation input power was initially set to 1 W. The correct spacing among antennas for a CEP sensitive signal is calculated in the following way. Firstly, different devices with 3 antennas at different antennas spacing are studied; then, the CEP value at each antenna for the three devices is analysed and the average CEP shift between one antenna and the next is evaluated. These values are set into a graph, as in Figure 3.17.

The required CEP shift from one antenna to the next is ~ 0 , in order to obtain a successful CEP detection. Finally the results are interpolated and the spacing value with zero CEP shift among one tip and the next is extrapolated. The extracted

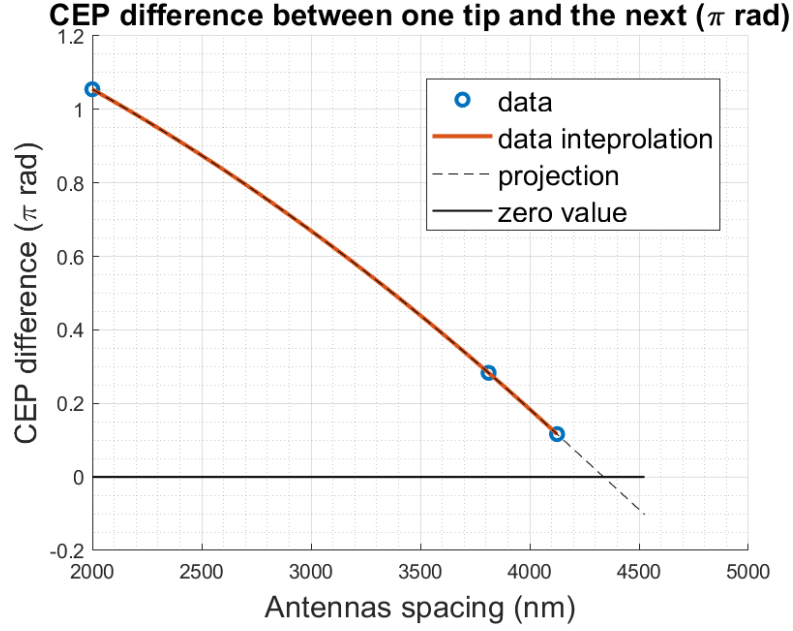


Figure 3.17: Average CEP difference between one antenna and the next as a function of antennas spacing.

antennas spacing value for CEP sensitivity is $\sim 4.3 \mu\text{m}$. Nevertheless, a few more data are subsequently collected, as shown in Figure 3.18, and a new interpolation is carried out. The $4.5 \mu\text{m}$ -spacing device is the one that has the lowest CEP shift among the collected values and it is the one that will be considered in this thesis. Besides, a more precise CEP detection can be carried out for values of antenna spacing of $\sim 4.42 \mu\text{m}$, as extrapolated from the linear interpolation in Figure 3.19.

Field distribution

The field distribution in the device is described in this section, at different frequencies and at relevant device zones. The field in the center of the waveguide core, for $\lambda = 1500 \text{ nm}$ is shown in figure 3.20, studied along a XY cut-plane, with coordinate $z = 0$, which is the middle of the core height (reference to axis orientation in Figures 3.14 and 3.16).

As one can see, the field is mainly confined in the waveguide core, as expected, but the creation of standing waves occurs; this is due to the fact that the periodically-placed antennas reflect a fraction of the travelling wave and behave as resonant cavities. Right after the antennas, the field gradually distributes back to the core. This can be seen clearly in the last section of the waveguide, on the right, where no reflection occurs, so the field distributes as it would do in a simple waveguide.

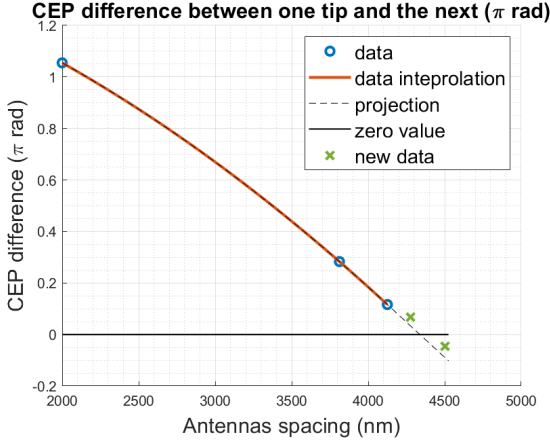


Figure 3.18: Average CEP difference between one antenna and the next as a function of antennas spacing.

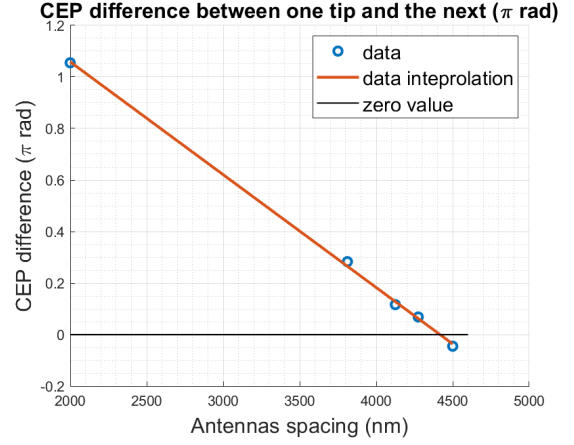


Figure 3.19: Average CEP difference between one antenna and the next as a function of antennas spacing.

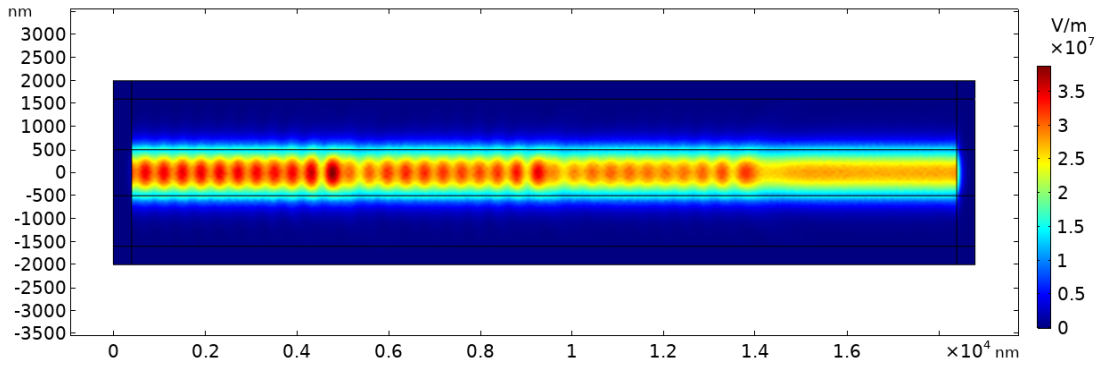


Figure 3.20: Field distribution in the core of the waveguide, for $\lambda = 1500$ nm, studied along a XY cut-plane, with coordinate $z = 0$, which is the middle of the core height (reference to axis orientation in Figures 3.14 and 3.16). The considered device has 3 antennas and antennas spacing $4.5 \mu\text{m}$.

Figure 3.21 shows the field distribution in the center of the waveguide, for $\lambda = 1500$ nm, studied along a XY cut-plane, with coordinate z such that it is at $3/4$ of the core height (reference to axis orientation in Figures 3.14 and 3.16).

This cut-plane representation is helpful for visually observe power losses, which will be studied thoroughly in subsection 3.3.3. Indeed, one can appreciate that at the third antenna (at $3/4$ of the length of the waveguide), field strength is weaker than at the first or second antennas. Figures 3.22 and 3.23 show the field distribution at the antennas, studied along a XY cut-plane, with coordinate z such

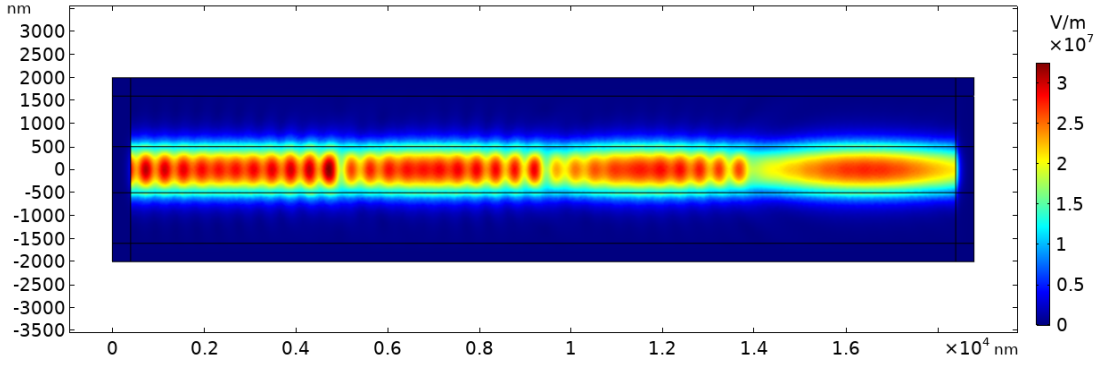


Figure 3.21: Field distribution in the core of the waveguide, for $\lambda = 1500$ nm, studied along a XY cut-plane, with coordinate z such that it is at $3/4$ of the core height (reference to axis orientation in Figures 3.14 and 3.16). The considered device has 3 antennas and antennas spacing $4.5 \mu\text{m}$.

that it is at the center of the gold layer.

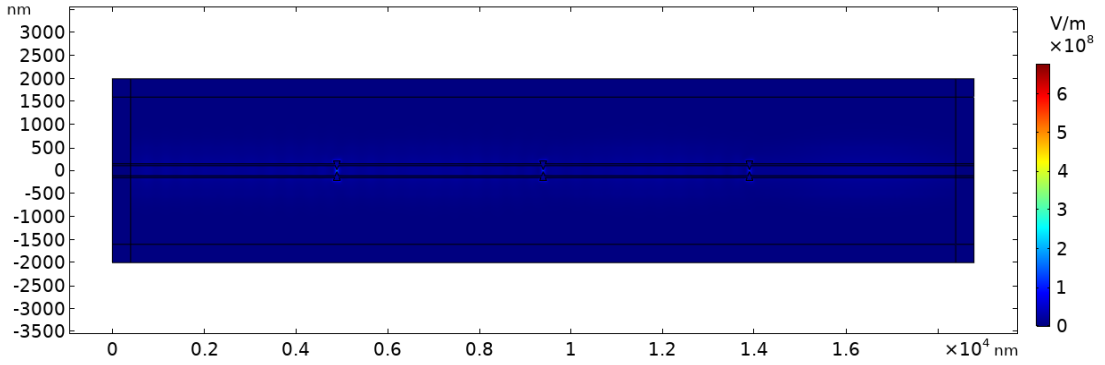


Figure 3.22: Field distribution at the antennas, for $\lambda = 1500$ nm, studied along a XY cut-plane, with coordinate z such that it is at the center of the gold layer. The considered device has 3 antennas and antennas spacing $4.5 \mu\text{m}$.

The scale is changed with respect to the previous image, since the field at tips of the antennas is around 10 times stronger than the one in center of the waveguide. Figure 3.23 shows the field at the tips of the second antenna of the device. As it is in Chapter 2, for the free-space nanoantennas, the field is focused to and enhanced at the tips of the antenna, at this wavelength value. Figure 3.24 shows the field distribution at the same cut-plane, but with saturated color scale; in particular, the scale maximum is set equal to the scale maximum of Figures 3.20 and 3.21.

This is done to enhance and analyze the behaviour of the field in the region surrounding the antennas. One can observe that the field is strongly concentrated at the antennas, but it also is enhanced at the connecting wires. Thus, the wires

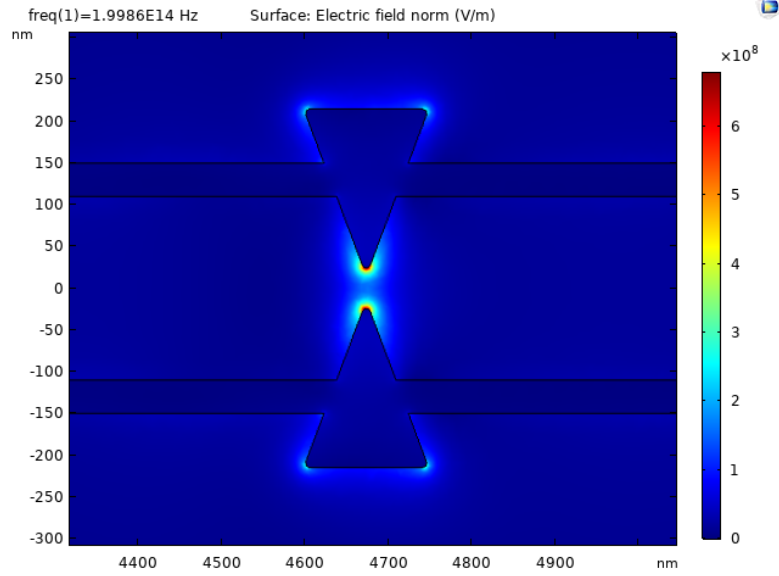


Figure 3.23: Field distribution at the antennas, for $\lambda = 1500$ nm, studied along a XY cut-plane, with coordinate z such that it is at the center of the gold layer.

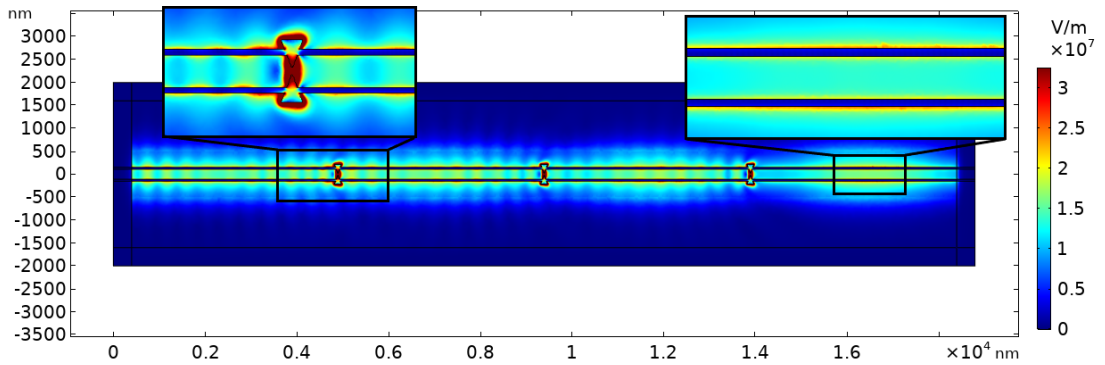


Figure 3.24: Field distribution at the antennas, for $\lambda = 1500$ nm, studied along a XY cut-plane, with coordinate z such that it is at the center of the gold layer. Colour scale is saturated, in order to enhance and analyze the behaviour of the field in the region surrounding the antennas. The considered device has 3 antennas and antennas spacing $4.5 \mu\text{m}$. The inset on the left shows the particular of the field oscillation around the connection wires. The inset on the right shows the concentration of field at the wires.

start behaving like a directional coupler, with some field exchange from one wire to the other, as can be seen by a slight field oscillation around the wires. Besides, one can see the light scattering from the device to the exterior.

From the waveguide section point of view, that is a YZ cut-plane (reference to axis orientation in Figures 3.14 and 3.16), one expects the field to travel along the waveguide, in a confined way inside the core; then, when in proximity to an antenna, the field is expected to concentrate to the antenna tips. This is what one can appreciate in Figures 3.25, 3.26, 3.28, 3.29, 3.31 and 3.32, describing the field distribution at different subsequent sections along the waveguide.

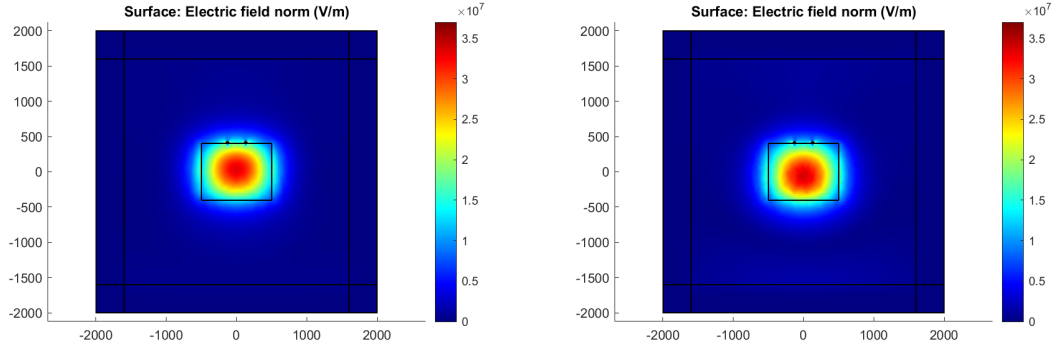


Figure 3.25: Field distribution at a waveguide section, at the input port, for $\lambda = 1500$ nm. **Figure 3.26:** Field distribution at a waveguide section, at ~ 600 nm from the input port, for $\lambda = 1500$ nm.

Figure 3.27

As can be seen, the field is confined to the waveguide core at the entrance of the device (Figure 3.25), with oscillating intensity caused by the standing wave generation due to reflection (Figures 3.26, 3.28 and 3.29). Then it concentrates to the bow-tie antenna (Figure 3.31) and the field is focused to the tips (Figure 3.32). This final process unfolds in several steps; first of all, the field displaces towards the antenna, as in Figure 3.31, then a large percentage of it gets focused to the antenna and some of it simultaneously still travels in a confined way inside the core, as in Figure 3.32. Finally, the field gets back to the center of the waveguide core, but it oscillates up and down around the central position, due to the fact that it is periodically concentrated up to the antennas. This can be appreciated by comparing Figure 3.25 and 3.26, which show two different position with respect to the center of the core. This oscillation and the interaction with the antennas cause power loss due to field scattering and absorption. Indeed, the field is scattered to the external cladding and it is absorbed by it. This process can be observed in Figure 3.32, as some field is present in the cladding region above the antenna. It

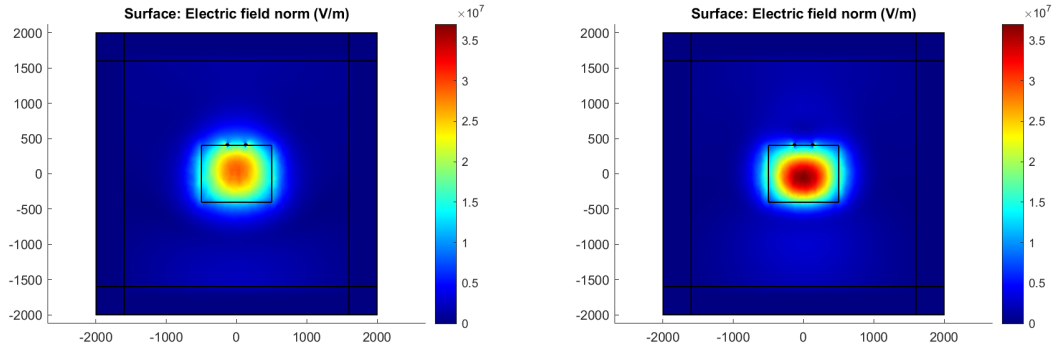


Figure 3.28: Field distribution at a waveguide section, at $\sim 1.2 \mu\text{m}$ from the input port, for $\lambda = 1500 \text{ nm}$.

Figure 3.29: Field distribution at a waveguide section, at $\sim 3.6 \mu\text{m}$ from the input port, for $\lambda = 1500 \text{ nm}$.

Figure 3.30

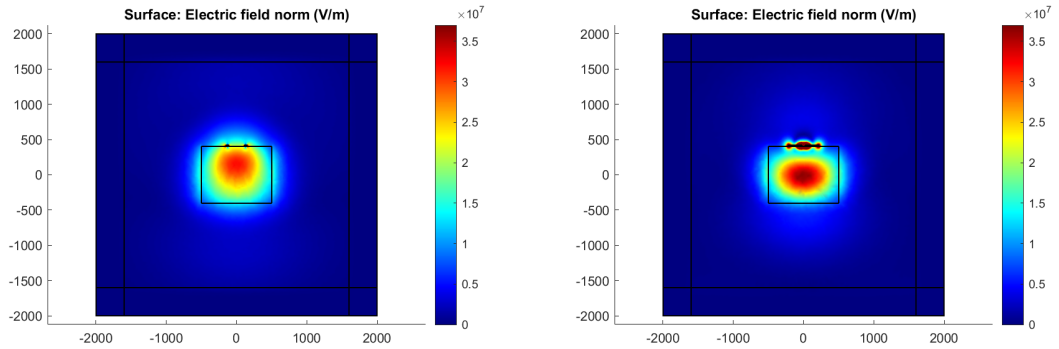


Figure 3.31: Field distribution at a waveguide section, $\sim 300 \text{ nm}$ before the first antenna, for $\lambda = 1500 \text{ nm}$.

Figure 3.32: Field distribution at a waveguide section, at the first antenna, for $\lambda = 1500 \text{ nm}$. The color scale is saturated, in order to show the fact that some field is still confined in the center of the core. Indeed, the field at the antennas is $\sim 10\times$ the maximum colour scale value.

Figure 3.33

will also be studied quantitatively in Subsection 3.3.3.

Field distribution - intermediate analyses

This understanding of the role of antennas and wires was obtained by analysing each of them separately. In this subsection, simulations of a device with bow-tie antennas only and no connecting wire and one with only wires and no antennas are carried out.

For the antennas only case, the device structure is the same as the waveguide-integrated bow-tie nanoantennas case, but no connecting wires are present, as in Figure 3.34.

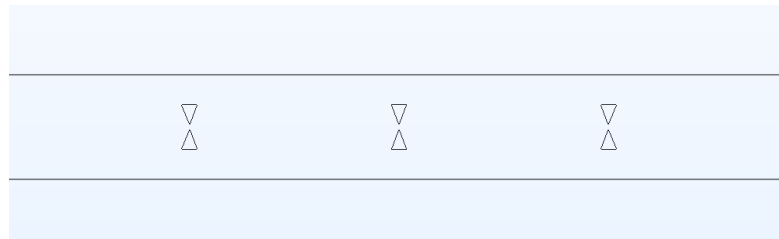


Figure 3.34: Top-view of the simulated model for the waveguide-integrated bow-tie nanoantennas, with no connection wires. No scale is present but the triangles height is 200 nm.

The spacing between one bow-tie antenna and the next is set to $2 \mu\text{m}$; this value does not ensure a 2π CEP shift between one antenna and the next, but it is chosen for a shorter simulation time. This will not have an impact on the accuracy of the results, since the antennas spacing only affects the pulse evolution and not the field behaviour (in terms of reflection and confinement) in the device. Besides, the effect of different spacing among bow-tie antennas along the waveguide are analyzed in the following subsection. The type of simulation is the same as the previous case and the settings are kept the same as well (boundary conditions, input/output port, frequency range). The fundamental mode for the waveguide is the same TM (transverse magnetic) mode, with non-zero components: (E_x, E_y, H_z) . The field distribution in the device can be seen in Figures 3.35 and 3.36 from a top viewpoint; the focusing of the field at the antennas is shown in Figure 3.37.

One can see that the same features as the previous case are present; indeed, both the generation of standing waves and the attraction of the field to the antennas occur in the same way. This shows that are the antennas that mainly contribute to the reflections.

For the wires only case, the device structure is the same as the waveguide-integrated bow-tie nanoantennas case, but no bow-tie antennas are present, as in

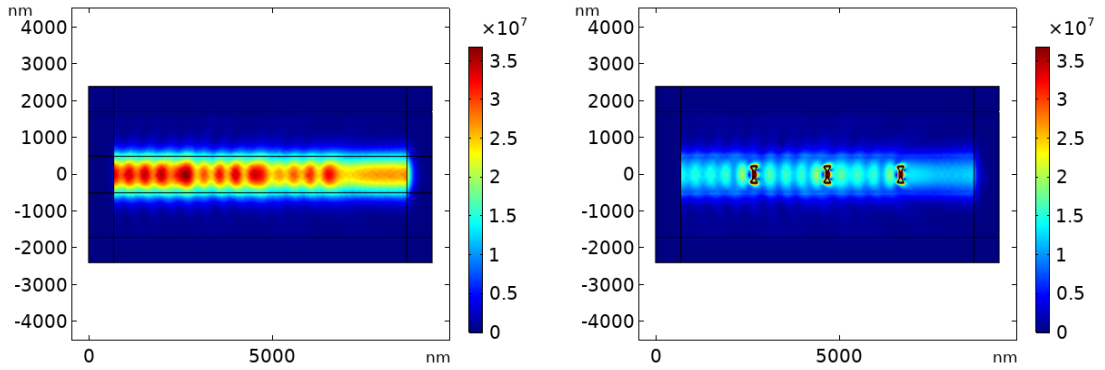


Figure 3.35: Field distribution in the core of the waveguide, for $\lambda = 1500$ nm, studied along a XY cut-plane, with coordinate $z = 0$, which is the middle of the core height (reference to axis orientation in Figures 3.14 and 3.16). The considered device has 3 antennas and antennas spacing $2 \mu\text{m}$.

Figure 3.36: Field distribution at the antennas, for $\lambda = 1500$ nm, studied along a XY cut-plane, with coordinate z such that it is at the center of the gold layer.. The considered device has 3 antennas and antennas spacing $2 \mu\text{m}$. Colour scale is saturated, in order to enhance and analyze the behaviour of the field in the region surrounding the antennas.

Figure 3.38. The total length of the device is $4 \mu\text{m}$.

The field distribution is shown in Figure 3.39 and the behaviour along the section of the waveguide is shown in Figure 3.40.

One can see that the two parallel wires behave as directional coupler, since the field is slightly concentrated at the wires and it oscillates spatially around them. One can also observe that from the section view the field is confined in the core of the waveguide, as it would do in a simple waveguide.

Field enhancement at tips

As explained earlier, in order to understand the interaction of a pulse with the plasmonic nanoantennas, it's important to study the field enhancement at the nanoantennas tips as a function of frequency. Indeed, different frequencies components of the pulse are enhanced according to field enhancement at tips. As done in Chapter 2, the field enhancement at tips (sometimes expressed as FE) is defined as the field averaged over the tip's surface, divided by a field reference value E_0 . The reference value is calculated as the maximum field value in the center of the core, at the entrance of the waveguide. It is calculated by averaging the field over a small parametric surface around the center of the waveguide, as shown in Figure 3.41,

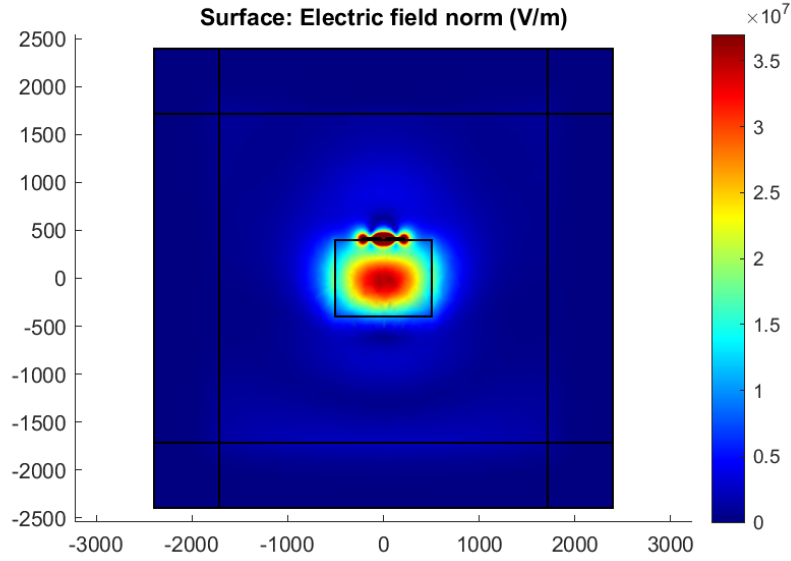


Figure 3.37: Field distribution at a waveguide section, at the first antenna, for $\lambda = 1500$ nm. The color scale is saturated, in order to show the fact that some field is still confined in the center of the core. Indeed, the field at the antennas is $\sim 10\times$ the maximum colour scale value.

considering a simple waveguide, without any metal structure on it. The surface is $30\text{ nm} \times 30\text{ nm}$ wide.

This average operation is needed to avoid numerical artifacts, that can lead to nonphysical values for the field at the center of the waveguide; the E_0 value in the considered frequency range is shown in 3.42.

The considered device is the same as in subsection (**Field distribution**) of section 3.3, with antennas spacing of $4.5\ \mu\text{m}$. The field enhancement of such structure is shown in Figures 3.43, 3.44, 3.45 and 3.46 and it is studied only for one of the two tips of a bow-tie antennas.

The field enhancement, as a whole, shows a trend composed mainly of very low field enhancement at low wavelength values, then a main increasing slope that leads to a main peak of $\sim 10/12$ at around $\lambda \sim 1500$ nm and finally a decrease to a plateau of ~ 6 at $\lambda > 1800$ nm. The main peak is due to plasmonic effects that enhance the field the tips. Its most relevant features are 3 main dips from the peak trend at around $\lambda = 1500$ nm, $\lambda = 1350$ nm and $\lambda = 1650$ nm and a couple of less appreciable ones at $\lambda = 1300$ nm and $\lambda = 1750$ nm. They can be explained as results of the resonant cavity reflections inside the device, due to the



Figure 3.38: Top-view of the simulated model for the waveguide-integrated bow-tie nanoantennas, with no bow-tie antennas, with only the connection wires. No scale is present but the waveguide width is $1 \mu\text{m}$.

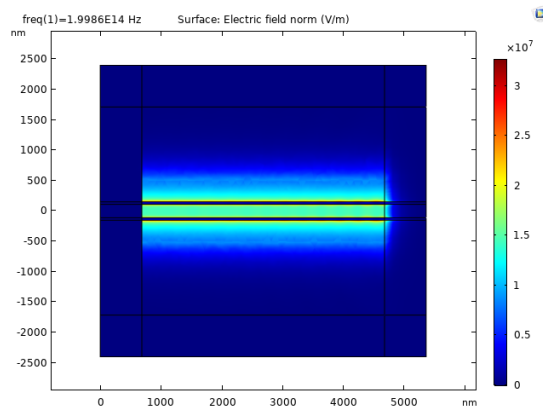


Figure 3.39: Field distribution at the gold layer, for $\lambda = 1500 \text{ nm}$, studied along a XY cut-plane, with coordinate z such that it is at the center of the gold layer. Colour scale is saturated.

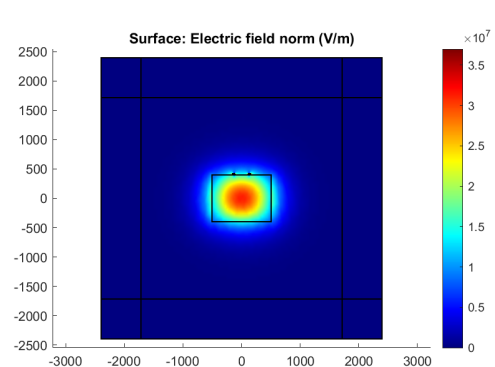


Figure 3.40: Field distribution at a waveguide section, at the middle point of the waveguide, for $\lambda = 1500 \text{ nm}$.

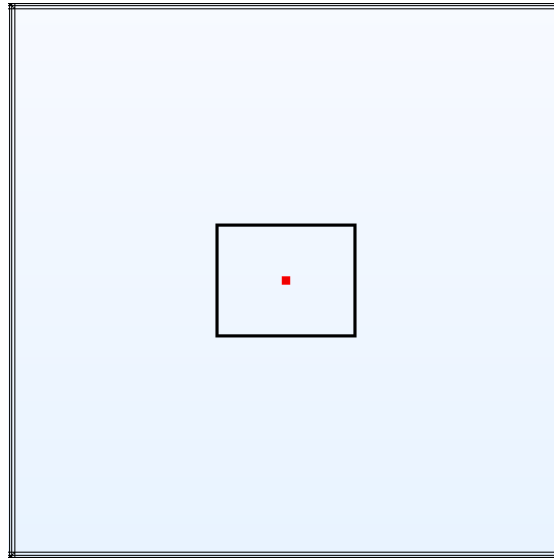


Figure 3.41: Waveguide section at the input port. In red is represented the parametric surface over which the field average operation is carried out in order to obtain the E_0 value. No scale is present but the waveguide core height is 800 nm.

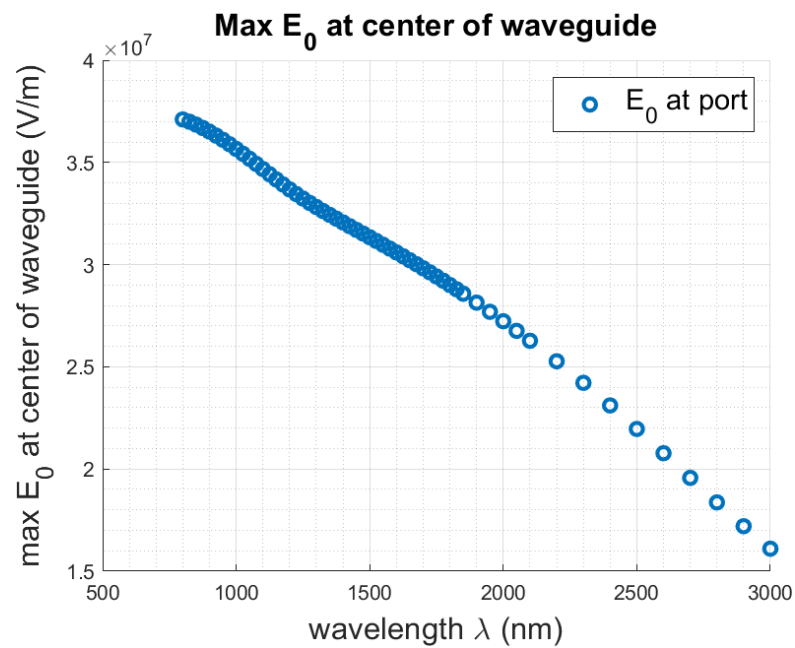


Figure 3.42: Reference value E_0 at the waveguide input port as a function of wavelength λ .

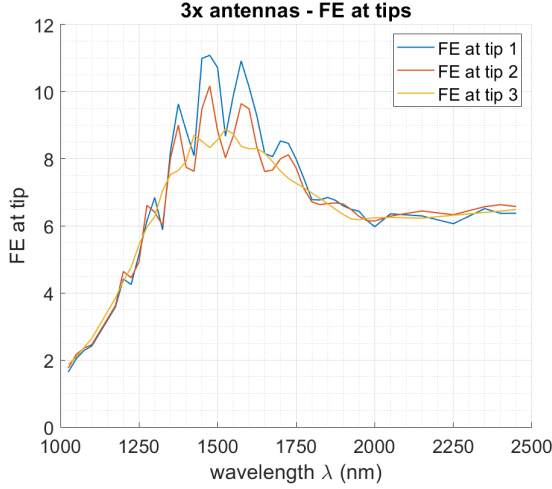


Figure 3.43: Field enhancement at the antennas tips as a function of wavelength λ , for the three bow-tie antennas along the waveguide. The considered device has 3 antennas and antennas spacing $4.5 \mu\text{m}$

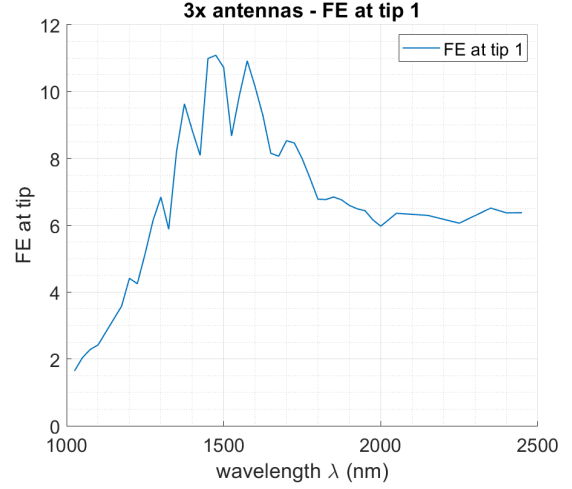


Figure 3.44: Field enhancement at the antennas tips as a function of wavelength λ , for the first bow-tie antenna along the waveguide. The considered device has 3 antennas and antennas spacing $4.5 \mu\text{m}$

periodic placement of antennas. Indeed, the generation of standing waves may lead to destructive resonance at the tip location for certain frequencies and hence a dip in the field value. It is interesting to notice that this phenomenon is less present at the last antenna of the device. Indeed, in Figure 3.46, the dips are not at the same frequencies as the other two and they are not as deep. This is due to the fact that no reflection occurs from the last tip to the end of the waveguide, so the destructive resonance is not as strong as at the other tips. Besides, the standing wave between the second and third antenna is different with respect to the one generated between the first and second antenna, since it is not surrounded by standing waves; hence, the dips are not at the same frequencies. This is demonstrated by the fact that if only one antenna is present in the device, no dip in FE is appreciable, as will be discussed in Figure 3.48 in subsection (**Field enhancement at tips - intermediate analysis**) of section 3.3. At lower frequencies, a plateau at FE value different than 0 is reached. This is due to the fact that at lower frequencies the field is less confined in the core of the waveguide and extends outside of it, up to the antennas. This leads to have FE different than 0 always for $\lambda > 1800 \text{ nm}$; in particular, the plateau is then bound to increase at even higher wavelengths, but that is not the range of frequencies at which the device shows interesting results.

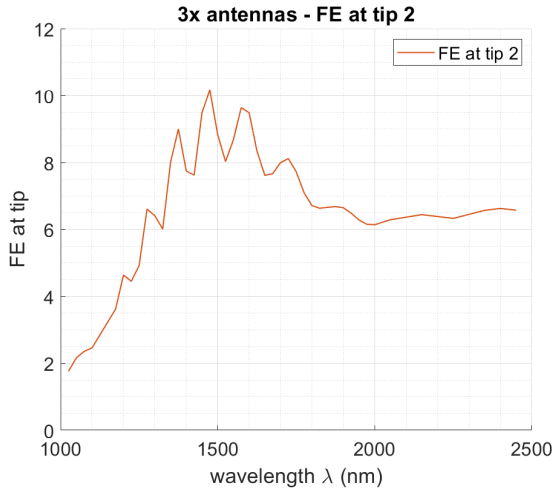


Figure 3.45: Field enhancement at the antennas tips as a function of wavelength λ , for the second bow-tie antenna along the waveguide. The considered device has 3 antennas and antennas spacing $4.5 \mu\text{m}$

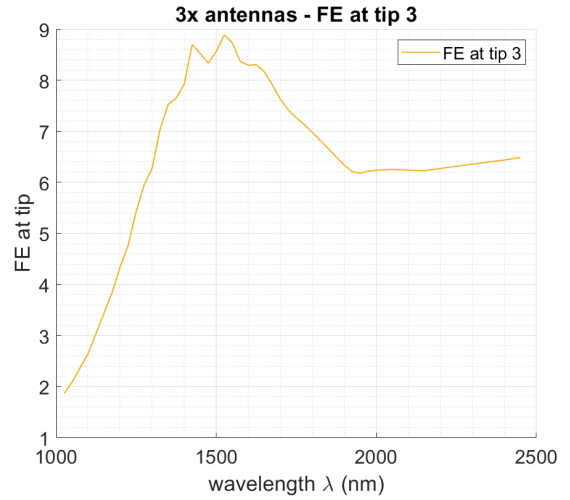


Figure 3.46: Field enhancement at the antennas tips as a function of wavelength λ , for the third bow-tie antenna along the waveguide. The considered device has 3 antennas and antennas spacing $4.5 \mu\text{m}$

Field enhancement at tips - intermediate analysis

As stated earlier, a device that only has one bow-tie antenna in it is simulated and the results are reported in Figures 3.47 and 3.48.

This result shows the characteristic peak given by plasmonic effects, but does not show any dip in FE. This is explained by looking at Figure 3.47, which shows that the antenna is not impinged from the right side by a reflected standing wave. The effect of the reflected waves can be verified by adding even more antennas. For example, in Figures 3.49 and 3.50, the simulation results of a device with 5 bow-tie antennas is shown.

As one can see, the dip in FE at $\lambda \sim 1600 \text{ nm}$ is very deep at tip 1, but decreases in depth at the following tips. Tip 5 has a very shallow dip. This is due to the fact that the device is behaving like a multilayered material, where at each antenna a portion of light is transmitted and a portion is reflected. This causes the first tip to be impinged by more reflected waves than the following ones and the last one is not impinged by any reflected wave.

Given the reflection and the generation of standing waves, one can expect that the spacing between antennas is an important parameter to fit the standing wave

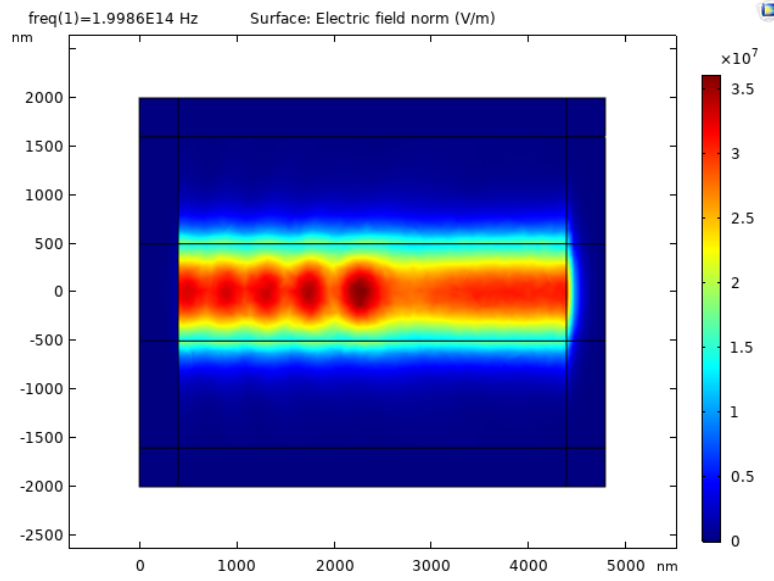


Figure 3.47: Field distribution in the core of the waveguide, for $\lambda = 1500$ nm, studied along a XY cut-plane, with coordinate $z = 0$, which is the middle of the core height (reference to axis orientation in Figures 3.14 and 3.16). The considered device has 1 antenna and antennas spacing $2 \mu\text{m}$.

in the cavity and consequently to obtain a higher field enhancement at tips. This aspect is analyzed by varying the antennas spacing and sampling the FE at a given frequency. The chosen frequency is $\lambda = 1475$ nm, because it coincides with the main peak of FE. The result is shown in Figure 3.51. One can see that the FE at $\lambda = 1475$ nm oscillates as a function of spacing. In particular, this happens mainly for antenna 1 and antenna 2. The results show that a rapid oscillation is present, as expected, but the change in FE value is not much relevant, since it varies between [9, 12]. As explained in previous examples, antenna 3 is not affected by reflected waves, so no oscillation is observable.

3.3.2 Time-domain analysis

The field enhancement studied in the previous section is important in order to study the behaviour of pulses at the antennas. Indeed, different frequency components of the waveform will be enhanced according to field enhancement at tips. This operation is implemented in a MATLAB script, that can be found in Appendix A, as "pulsefilter.m". A \cos^2 -shaped incident pulse with a central wavelength of 1550 nm and a pulse duration of 10 fs FWHM was assumed. The spectrum of the pulse was obtained by a Fourier transform. The time-domain response was obtained by

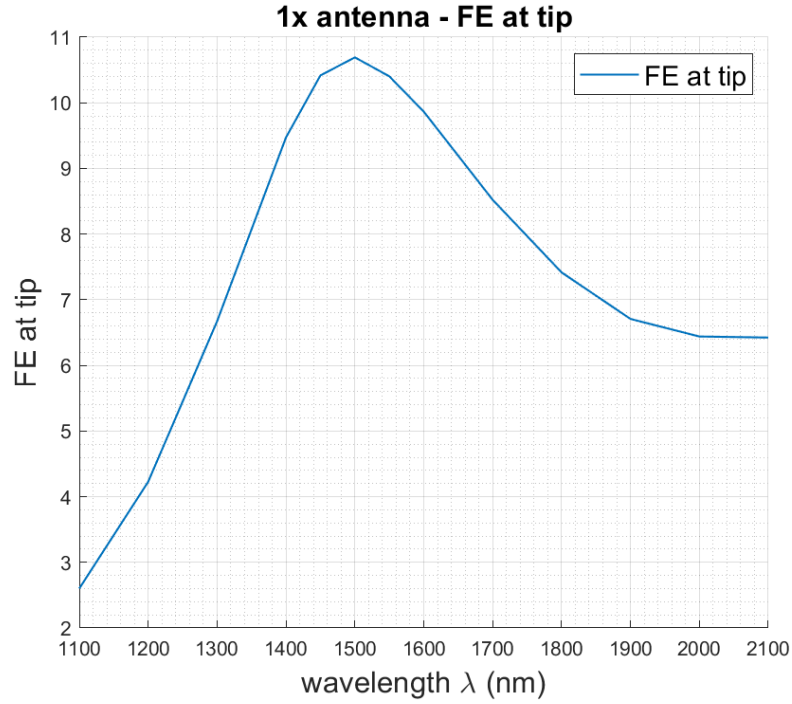


Figure 3.48: Field enhancement at the antenna tips as a function of wavelength λ . The considered device has 1 antenna and antennas spacing $2 \mu\text{m}$.

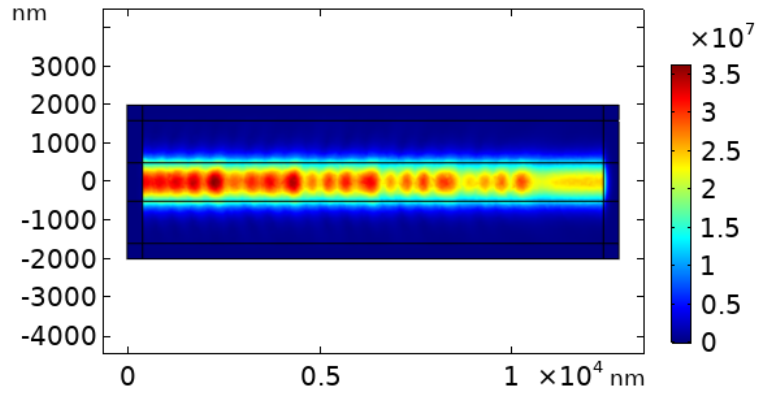


Figure 3.49: Field distribution in the core of the waveguide, for $\lambda = 1500 \text{ nm}$, studied along a XY cut-plane, with coordinate $z = 0$, which is the middle of the core height (reference to axis orientation in Figures 3.14 and 3.16). The considered device has 5 antennas and antennas spacing $2 \mu\text{m}$.

an inverse Fourier transform of the frequency-domain response.

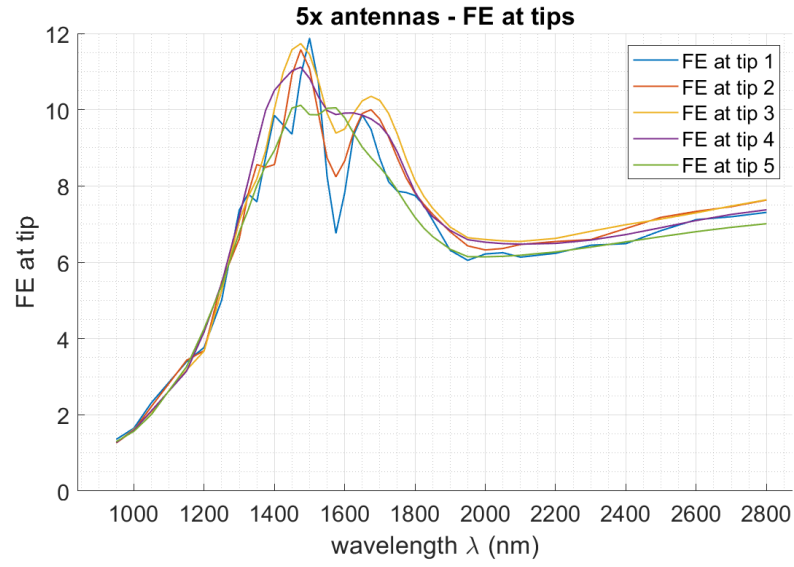


Figure 3.50: Field enhancement at the antennas tips as a function of wavelength λ . The considered device has 5 antennas and antennas spacing $2 \mu\text{m}$

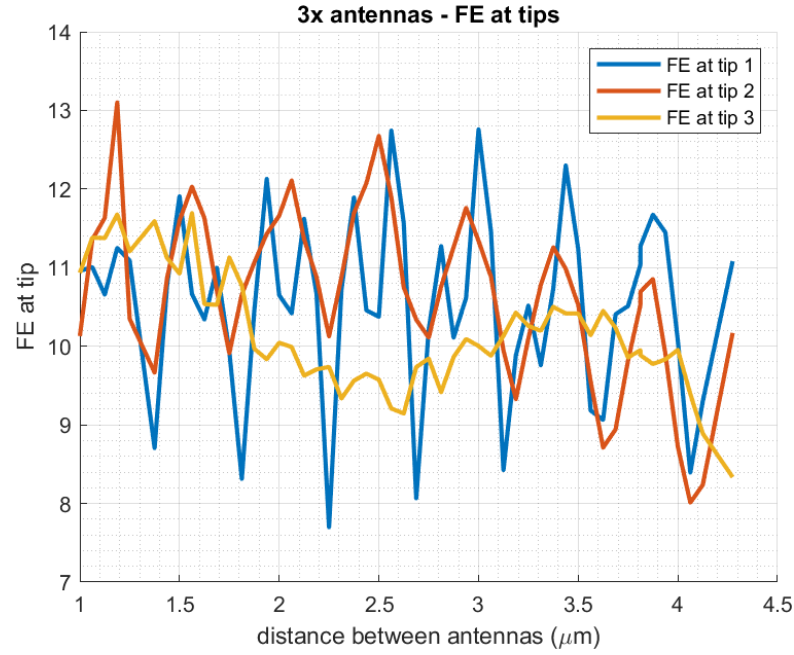


Figure 3.51: Field enhancement at the antenna tips as a function of antennas spacing, at $\lambda = 1475 \text{ nm}$. The considered device has 3 antennas.

Pulses at antennas

The input pulse can be seen in Figure 3.52. The considered device is the one with 3 antennas and $4.5 \mu\text{m}$ spacing between them. The pulse is then filtered by the code,

given the device frequency response. The obtained enhanced pulses are shown in Figures 3.53, 3.54 and 3.55 and 3.56.

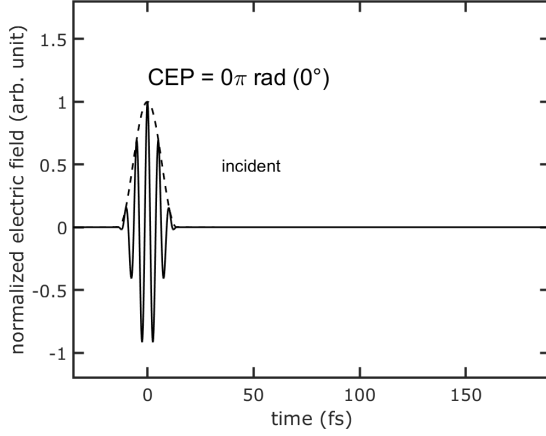


Figure 3.52: Normalized incident pulse field as a function of time, at the input port of the waveguide. The considered device has 3 antennas and antennas spacing $4.5 \mu\text{m}$.

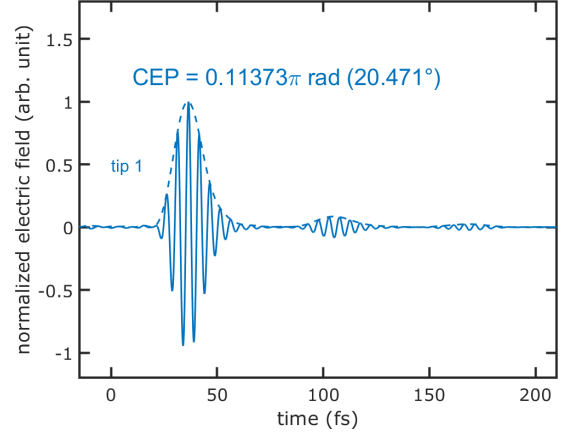


Figure 3.53: Normalized enhanced pulse at the first antenna as a function of time. The considered device has 3 antennas and antennas spacing $4.5 \mu\text{m}$.

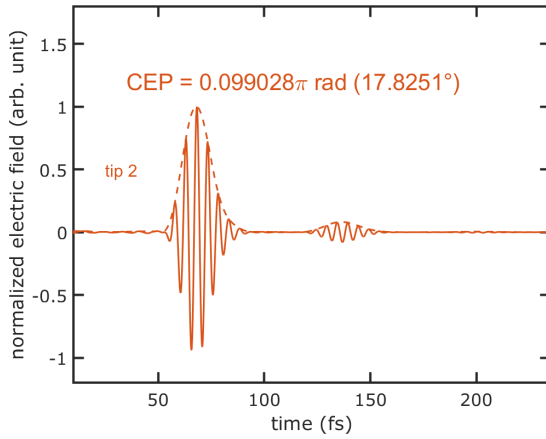


Figure 3.54: Normalized enhanced pulse at the second antenna as a function of time. The considered device has 3 antennas and antennas spacing $4.5 \mu\text{m}$.

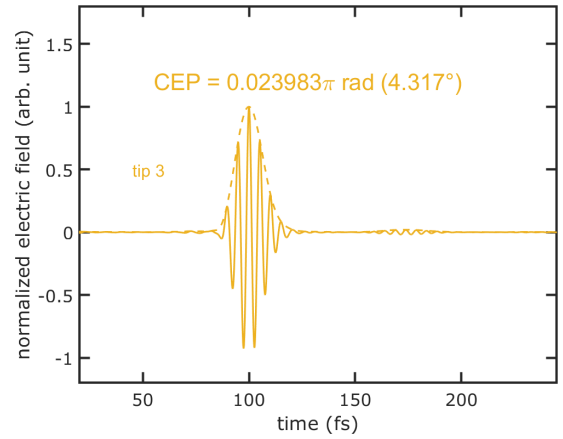


Figure 3.55: Normalized enhanced pulse at the third antenna as a function of time. The considered device has 3 antennas and antennas spacing $4.5 \mu\text{m}$.

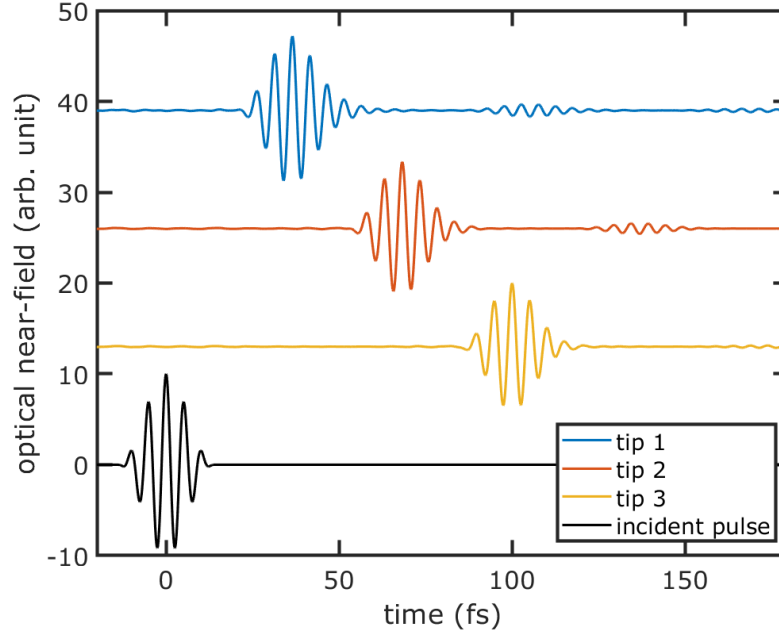


Figure 3.56: Input pulse and enhanced pulses at the antennas. Arbitrary field units. The considered device has 3 antennas and antennas spacing $4.5 \mu\text{m}$.

First of all, one can notice that the three pulses are shifted ahead in time, with respect to the incident one. In particular, the pulse at tip 1 is shifted of ~ 35 fs, the one at tip 2 of ~ 65 fs and the one at tip 3 of ~ 95 fs. This is due to the fact that the pulse travels along the waveguide and it takes some time to do it. The group velocity of the pulse can be calculated, since we set the distance among antennas; for tip 3: $v_g = \frac{3 \times 4.5 \mu\text{m}}{95 \text{ fs}} \simeq 0.45 \cdot c$. More or less the same value is extracted from tip 1 and tip 2. This is quite an expected value for the group velocity of the pulse, since the estimated value for a simple waveguide of the same structure, dimension and materials was ~ 0.46 , as shown in Figure 3.4. Besides, the resulting pulses show a smaller secondary pulse forward in time ($\sim 65 - 75$ fs ahead than the pulse) and an even smaller one ($\sim 115 - 135$ fs ahead than the pulse). This is due to the reflection between bow-tie antennas along the waveguide, that cause reflected pulses that take some more time to get back to the previous tip. The normalized spectra of the pulses is shown in Figure 3.57.

2π CEP circling

As one can see from the pulses figures, the pulses at antenna 1, 2 and 3 possess roughly the same CEP value. This is shown in Figure 3.58.

This is important in order to make the device CEP sensitive.

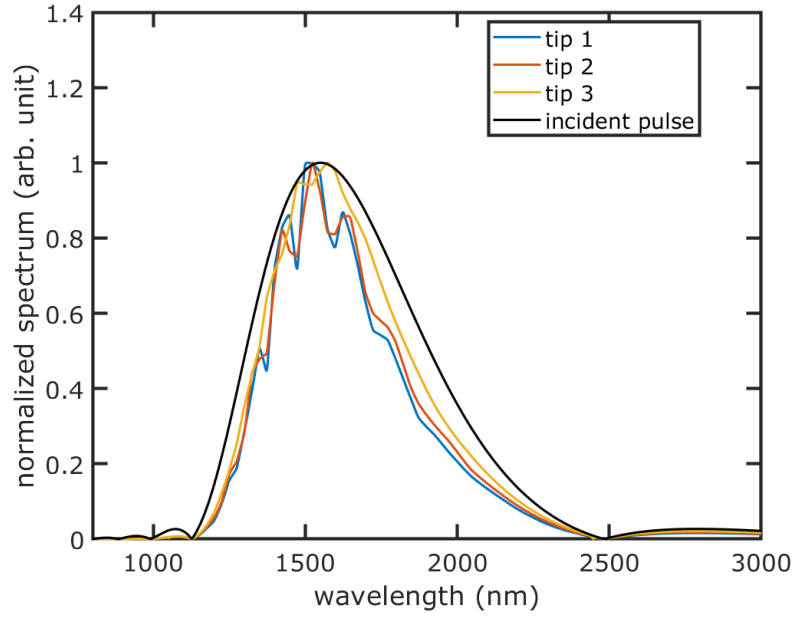


Figure 3.57: Normalized spectra of the studied pulses. The considered device has 3 antennas and antennas spacing $4.5 \mu\text{m}$.

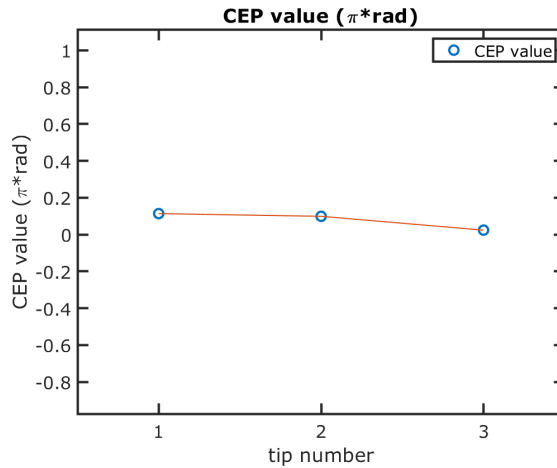


Figure 3.58: CEP value, calculated at the three considered antennas. The considered device has 3 antennas and antennas spacing $4.5 \mu\text{m}$.

For this device, the average CEP shift from one antenna to the next is $\sim 0.04\pi$; this shows that the chosen spacing among antennas is very close to the ideal case.

As an example for an incorrect antennas spacing value, the case of the device with 3 antennas, $2 \mu\text{m}$ apart from each other is analysed. The pulses are shown in

Figure 3.59.

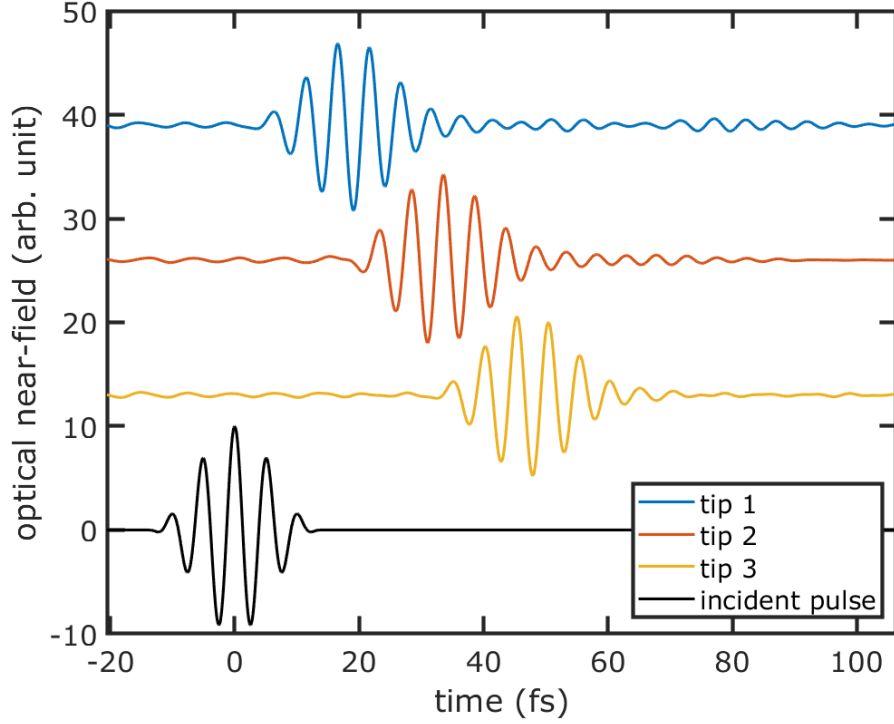


Figure 3.59: Input pulse and enhanced pulses at the antennas. Arbitrary field units. The considered device has 3 antennas and antennas spacing $2 \mu\text{m}$.

The calculated CEP is shown in Figure 3.60. The average CEP shift from one antenna to the next is $\sim 1\pi$.

3.3.3 Power transmission and losses

In order to understand the behaviour of the device, it's important to evaluate the power transmission and the power losses. The power transmission can be evaluated by means of the square of the S-parameter $|S_{21}|^2$. The S-parameter S_{21} studies the field that exits the output port, divided by the field that is injected in the input port. The $|S_{21}|^2$ value for the 3 antennas, $4.5 \mu\text{m}$ spacing device, as a function of frequency is shown in Figure 3.61.

This graph shows the presence of a dip in power transmission for $\lambda \sim 1450 \text{ nm}$; this wavelength corresponds roughly to the peaks in FE at the tips of the antennas, so it shows the fact that when the antennas are resonantly excited, power is absorbed and scattered by the antennas. This will be studied thoroughly in Figure 3.63. The power losses, for that frequency, are around 25% of the total input power. The other dips in power transmission (at $\lambda \sim 1350 \text{ nm}$, 1550 nm and

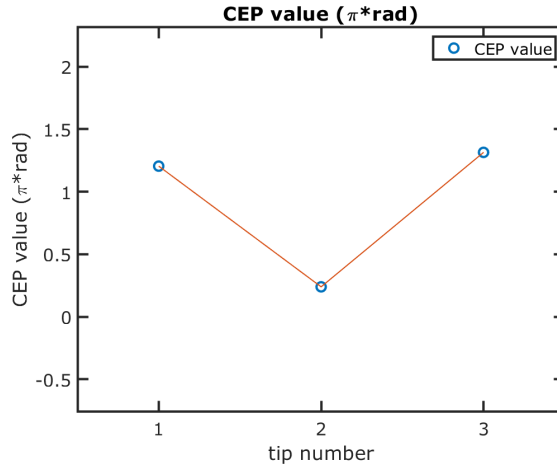


Figure 3.60: CEP value, calculated at the three considered antennas. The considered device has 3 antennas and antennas spacing $2 \mu\text{m}$.

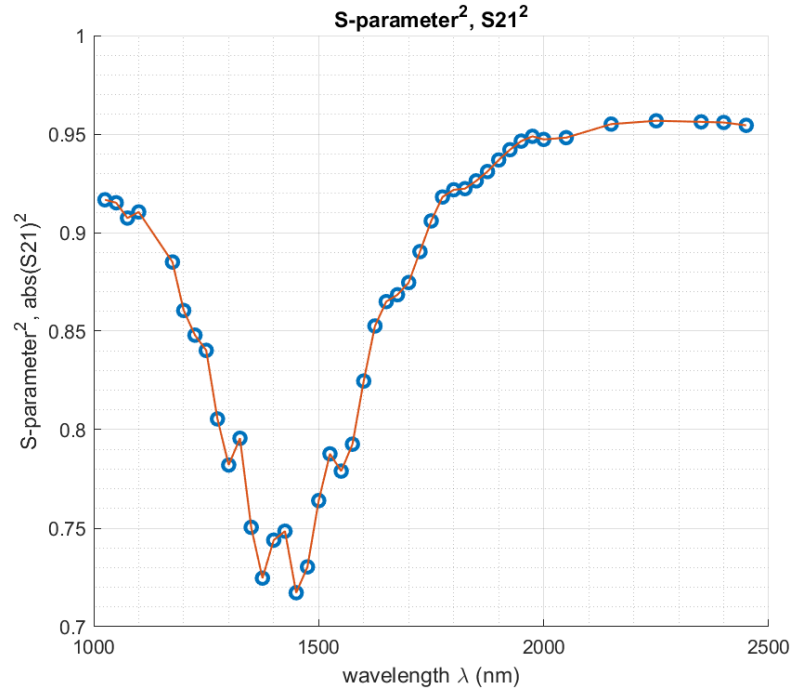


Figure 3.61: S_{21}^2 parameter as a function of wavelength. The considered device has 3 antennas and antennas spacing $4.5 \mu\text{m}$.

1300 nm) are due to the generation of standing waves and hence the presence of constructive and destructive interference.

The power transmission can also be studied by discerning the power that exits the output port through the core of the waveguide and through the cladding. This is studied in Figure 3.62.

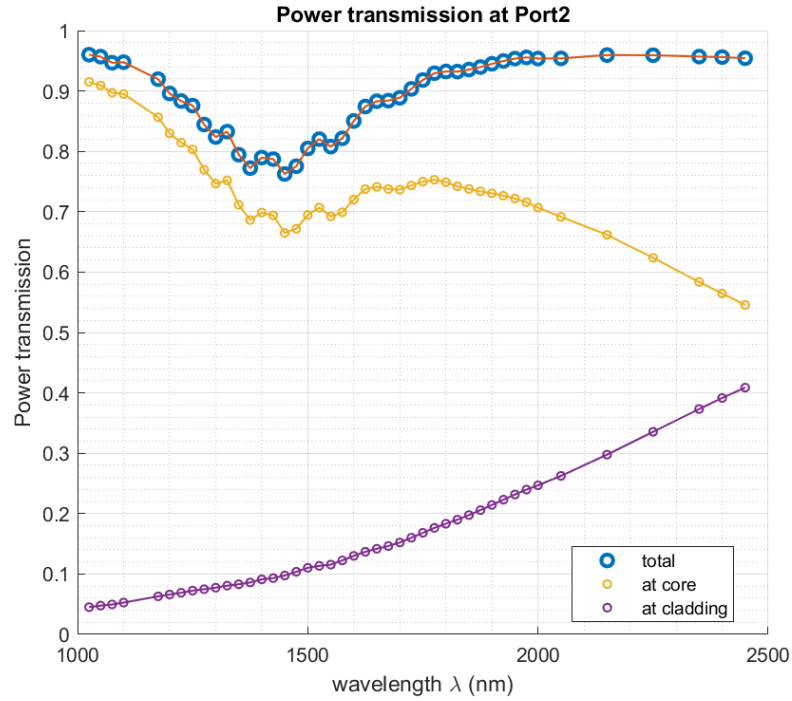


Figure 3.62: Power transmission at output port of the waveguide as a function of wavelength. In particular, the contribution of power crossing the core or the cladding of the waveguide is shown. The considered device has 3 antennas and antennas spacing $4.5 \mu\text{m}$.

As one can see, at $\lambda \sim 1500 \text{ nm}$ around 65% of the input power goes through the core of the waveguide and only $\sim 10\%$ through the cladding. This gap decreases as the frequency decreases, as an effect of the less confinement in the core for lower frequencies. The total losses can be studied as a result of several contributions. The main ones are found to be the power absorption in the metal structure (wires and antennas) and the power scattering towards the outer region of the cladding; no power is lost in the waveguide materials, because they are set as lossless in the simulation. This evaluation is reported in Figure 3.63.

The yellow curve shows the power absorption in the metal structure, with peaks of 10% – 15% of power loss for the resonance frequencies, whereas a constant absorption of 3% – 5% in the rest of the frequency range. Concerning the scattered power, the green curve, one can observe a peak of 10% – 15% power loss in the resonance frequencies and a very low scattering ($\sim 1\%$) at the rest of the frequency

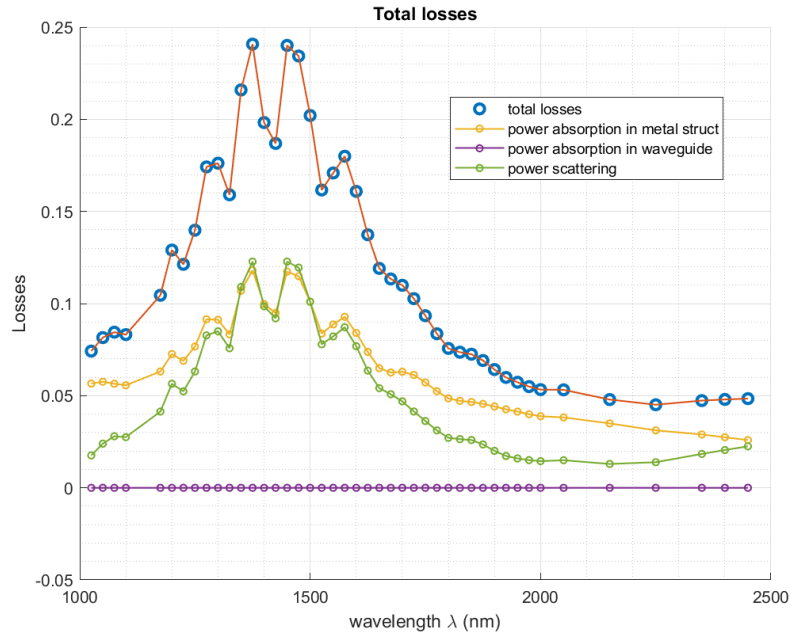


Figure 3.63: Total power losses as a function of wavelength. In particular, the contributions of power absorption at the metal nanostructures and in the waveguide material and power scattering at the antennas are shown. The considered device has 3 antennas and antennas spacing $4.5 \mu\text{m}$.

range.

Finally, it is important to study how losses change when an additional antennas are added to the device, in order to understand the effect of one antenna to the whole device. This is done by evaluating the losses of 5 different devices, respectively with 1, 2, 3, 4 and 5 antennas. The distance among antennas is set to $2 \mu\text{m}$ for all devices; it was previously verified that this parameter has no great influence on power losses. The transmitted power is studied for each device at $\lambda = 1550 \text{ nm}$ and, for each additional antenna, is reported in Figure 3.64. One can see that transmitted power decreases linearly with each added antenna. In particular, from Figure 3.65, around 8.3% of power is lost when adding an antenna to the device.

This shows that after 10 – 12 antennas, the signal would be all absorbed or scattered. The losses analysis is important in order to properly design a working device (number of antennas that can be placed in a row) and in order to subsequently evaluate the photoemission at each antenna. In the next subsection (3.3.4), photoemission from each antenna will be evaluated.

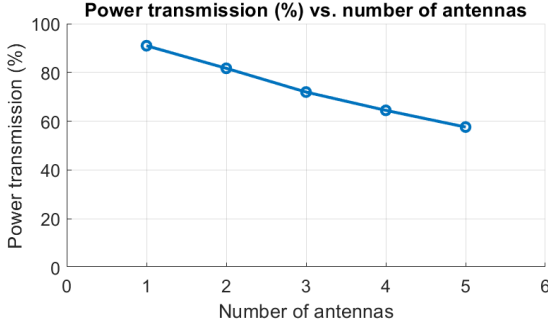


Figure 3.64: Power transmission at output port as a function of number of antennas coupled to the waveguide, for $\lambda = 1500$ nm. The considered devices have antennas spacing $2 \mu\text{m}$.

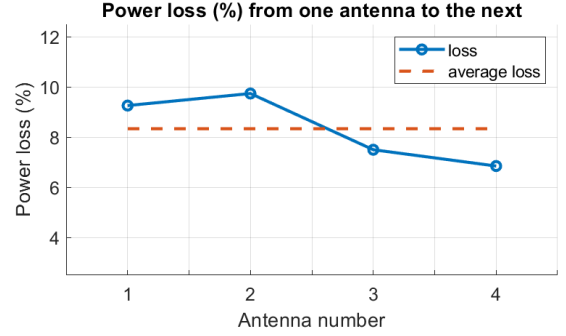


Figure 3.65: Power losses from one antenna to the next along the waveguide, for $\lambda = 1500$ nm. The considered devices have antennas spacing $2 \mu\text{m}$.

3.3.4 Fowler-Nordheim emission

As it is explained in Chapter 1, when a strong enough field is applied to the antennas, the potential barrier at the metal surface is deflected and electrons can be emitted in the surrounding space. This emission can be approximated by a quasi-static tunnelling rate and is calculated by a quasi-static Fowler-Nordheim (FN) emission model. The FN formulas are studied in Chapter 1 and are implemented in a MATLAB script. The waveform at the device input is a few-cycle 10 fs laser pulse, which shows ~ 2.5 optical cycles full-width half-maximum; the pulse's features are listed in Table 3.1.

Pulse features	Values
Pulse energy	100 pJ
Pulse duration	10 fs
Central frequency	1550 nm
Pulse peak power (100 pJ/10 fs)	10 kW
Pulse peak field	3.097 GV/m

Table 3.1: Features of the input field waveform at the waveguide port. The considered device has 3 antennas and antennas spacing $4.5 \mu\text{m}$.

As described in section 3.3.2, the pulse is processed by the field enhancement at the tips of the antennas, so the optical waveforms that cause photoemission are the resulting enhanced pulses in Figure 3.56, multiplied by the peak field value of the input pulse. The peak field value of the input pulse that is reported in Table 3.1,

and hence the peak intensity, are obtained by evaluating the peak field value at the center of the waveguide core at the input port of the waveguide, by the same process that is reported in section 3.3.1, where the field enhancement normalization value E_0 is calculated (see Figures 3.41 and 3.42). The peak field is taken for the pulse central wavelength $\lambda = 1550$ nm and it is $3.097 \times 10^7 V/m$, as from figure 3.42. But, since the input power in the COMSOL simulations is set to $1W$ and the chosen input pulse power is $10kW$, the peak pulse that is needed for the photoemission calculation for this kind of pulse is $3.097 \times 10^7 V/m \cdot \sqrt{(10000)} = 3.097GV/m$.

Another important parameter in the FN emission calculation is the energy barrier that has to be overcome to cause photoemission. In this case, emission occurs from the metal (Au) to an insulator (SiO_2) and the barrier can be studied as a Schottky barrier ϕ , which is the band offset between a semiconductor (or an insulator intended as a large band-gap semiconductor) and a metal. This is given by $\phi = \Phi_{Au} - \chi_{SiO_2} = 5.1eV - 0.9eV = 4.2eV$, where Φ_{Au} is the gold work function and χ_{SiO_2} is the SiO_2 electron affinity. These values are taken respectively from ref. [50] and ref. [51].

As described in Chapter 1, section 1.2.2, photoemission given by pulses is CEP sensitive and varies with the considered pulse CEP value. In this bow-tie configuration, photoemission occurs from both triangles tips according to field directed from one tip to the other or vice versa. Photoemission can then be written with the notation, used in ref. [30] and ref. [23], which is: $I = I_L - I_R$, where I_L is the photocurrent emitted by the left-side triangles (left-side as one sees them when looking at the waveguide from the input port) and I_R the one emitted by the right-side ones. They can be expressed as:

$$I_L \approx I_{0,L} + |I_{1,L}| \cos(\varphi_{ce} + \angle I_{1,L}) \quad \& \quad I_R \approx I_{0,R} - |I_{1,R}| \cos(\varphi_{ce} + \angle I_{1,R}) \quad (3.1)$$

where I_0 represents the total average photocurrent, I_1 the complex amplitude of the first harmonic of the CEP-sensitive photocurrent. As explained in the two cited papers, if the nanoantennas are perfectly symmetric $I_{1,L}$ and $I_{1,R}$ would be equal, so $I = 2|I_{1,L}| \cos(\varphi_{ce} + \angle I_{1,L})$; otherwise, in presence of imperfections in fabrication (as is the case in the cited papers), a more general expression is $I = I_{0,detected} + |I_{cep}| \cos(\varphi_{ce} + \angle I_{cep})$, where $I_{0,detected}$ is the residual average total photocurrent and I_{cep} is the complex amplitude of the first harmonic of the total CEP-sensitive photocurrent. The minus sign in the CEP-sensitive component of I_R is given by the fact that the right-side antennas needs a reversed field polarity to emit electrons with respect to the left-side one. This leads to a peak in the emitted CEP-sensitive current for a carrier wave that is shifted by π radians with respect to the left-side one.

In the following results, the charge and current emitted by the left-side nanotriangles are reported with a "positive" sign, while the ones from the right-side nanotriangles are set as "negative". This is given by the fact that the pulse possesses positive and negative field components, which are eventually associated to the field polarity directed from the left-side tips to the the right-side ones or viceversa.

The steps that are carried out in this analysis are the following. Firstly the FN equation is expressed in a simplified form to get to a physically complete Fowler-Nordheim-type equation, as explained in the introduction, Subsection 1.2.2; this leads to a computation of the photocurrent density, hence an estimation of the emission surface is needed in order to obtain the total emitted CEP-sensitive photocurrent. The emission surface can be estimated by analysing the emitted photocurrent obtained in the experimental work reported in ref. [23] on the free-space bow-tie nanoantennas array. Indeed, in the paper is reported the measured value of CEP-sensitive photocurrent per antenna. Thank to this, after the free-space device behaviour is simulated and the CEP-sensitive current density is estimated by means of the FN-type equation, the emission area can be calculated. Finally the the CEP-sensitive photocurrent from the waveguide-integrated nanoantennas is calculated.

Simplified Fowler-Nordheim-type equation

The physically complete, simplified standard Fowler-Nordheim-type equation is obtained following ref. [39], as is done in some unpublished work from Drew Buckley¹ *et al.* and it consists in:

$$J = a\phi^{-1}H(-F)F^2 \exp\left[-\frac{\nu \cdot b \cdot \phi^{3/2}}{F}\right] \quad (3.2)$$

where the variable ν is the adjustment factor, F the electric field strength normal to the nanoantenna surface in V/m, H is the Heaviside function, and ϕ the Schottky barrier in eV. The adjustment factor was defined by

$$\nu \approx 1 - f + \frac{1}{6}f \ln f \quad (3.3)$$

where f is the barrier field which was approximated to $f \approx 1.44 \frac{eV^2 nm}{V} \left(\frac{F}{\phi^2}\right)$. The scaling factors a and b were taken to be 1.5×10^6 A eV V⁻² and 6.8 V eV^{-3/2} nm⁻¹,

¹Research Laboratory of Electronics, Massachusetts Institute of Technology, Cambridge, MA 02139, USA and Department of Electrical and Computer Engineering, Wentworth Institute of Technology, Boston, MA, USA.

respectively. The following figures show the obtained results. In Figure 3.66, the enhanced pulse at antenna number 1 of the device is plotted together with the calculated photoemitted current density, for an incident pulse with CEP = 0 rad and for an incident pulse peak field of 3.097 GV/m.

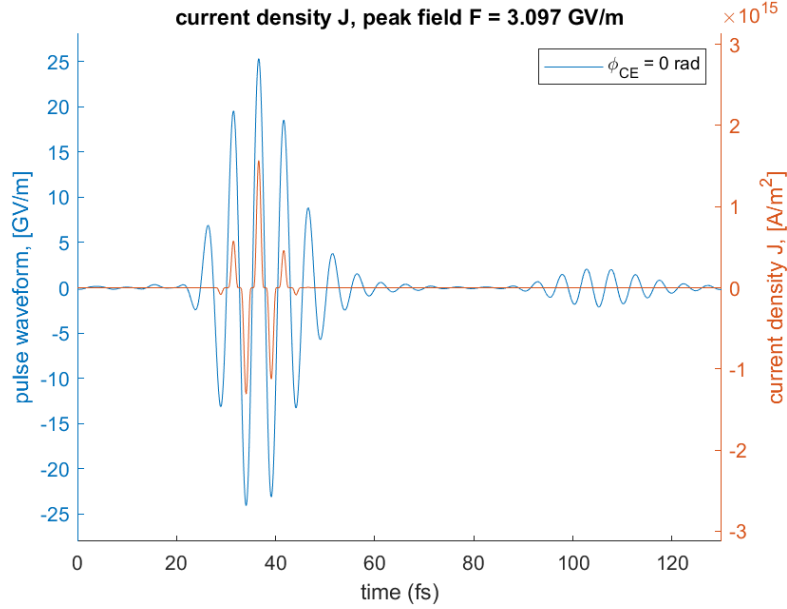


Figure 3.66: Field waveform of the enhanced pulse at the first antenna and instantaneous emitted current density as a function of time. The CEP value for the input pulse is set to zero.

One can appreciate the presence of both "positive" and "negative" current densities, according to the pulse field sign (i.e. polarity). Furthermore, current is emitted only at field values that are high enough to cause tunneling across the interface energy barrier. It is important to notice that the secondary peak that lies ahead in time does not contribute to photocurrent. By integrating the instantaneous current density over time, the emitted charge density is calculated. In particular, the "positive" component (corresponding to the current emitted from the left-side nanotriangle) and the "negative" one are integrated separately, in order to obtain separate information on the charge emitted from one tip and from the other. Eventually the charge density is multiplied by the repetition rate of the incident pulse, as in Table 3.1, to obtain the total emitted current density. The charge density is studied for different CEP values of the incident pulse at the same antenna number 1, so the graph in Figure 3.67 is obtained:

This figure is the graphical representation of the formulas in Equation 3.1, except for two constant factors: the repetition rate, that transforms the charge density in current density, and the emission surface that transforms current densities in current

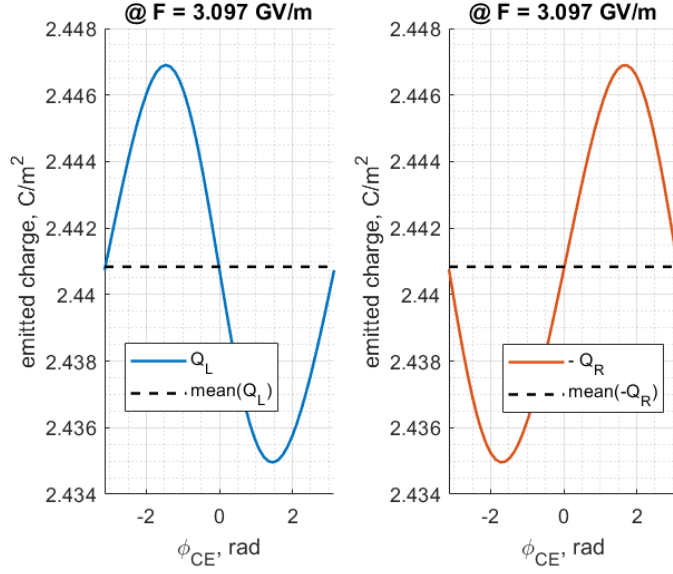


Figure 3.67: Emitted charge density as a function of CEP value of the input pulse, from the left and right tip of the bow-tie antennas.

values. In Figure 3.67, the amplitudes of the sinusoidal curves are, in the analogy to equations 3.1: $|Q_{1,L}| = 5.971 \times 10^{-3} \text{C/m}^2$ and $|Q_{1,R}| = 5.965 \times 10^{-3} \text{C/m}^2$, respectively and the mean values are $Q_{0,L} = 2.441 \text{C/m}^2$ and $Q_{0,R} = 2.441 \text{C/m}^2$. Finally the charge components are subtracted as in equation $I = I_L - I_R$ and the graph in Figure 3.68 is obtained:

As expected, this curve shows a residual average total charge density $|Q_{0,detected}| \sim 0 \text{C/m}^2$ and an amplitude of $|Q_{cep}| = 1.186 \times 10^{-2} \text{C/m}^2$, which corresponds to 2 times the amplitudes of the left and right tips charge density values. The latter is the CEP-sensitive charge density value of the 1st antenna. The CEP sensitivity is defined as the CEP-sensitive current over the average current: $|I_1|/I_0$, which, for constant emission surface and constant repetition rate can be expressed as $|Q_1|/Q_0$ or $|J_1|/J_0$.

The relevant results for all of the antennas are reported in Table 3.2; they all are expressed as current densities J , by multiplying the charge densities by the laser repetition rate. The considered quantities are: CEP-sensitive charge density from left-side nanotriangles $|J_{1,L}|$, mean charge density from left-side nanotriangles $J_{0,L}$, CEP-sensitive charge density from right-side nanotriangles $|J_{1,R}|$, mean charge density from right-side nanotriangles $J_{0,R}$, CEP sensitivity for the left-side nanotriangle $|J_{1,L}|/J_{0,L}$, CEP sensitivity for the right-side nanotriangle $|J_{1,R}|/J_{0,R}$, total CEP-sensitive current density $|J_{cep}|$ and residual average total current density

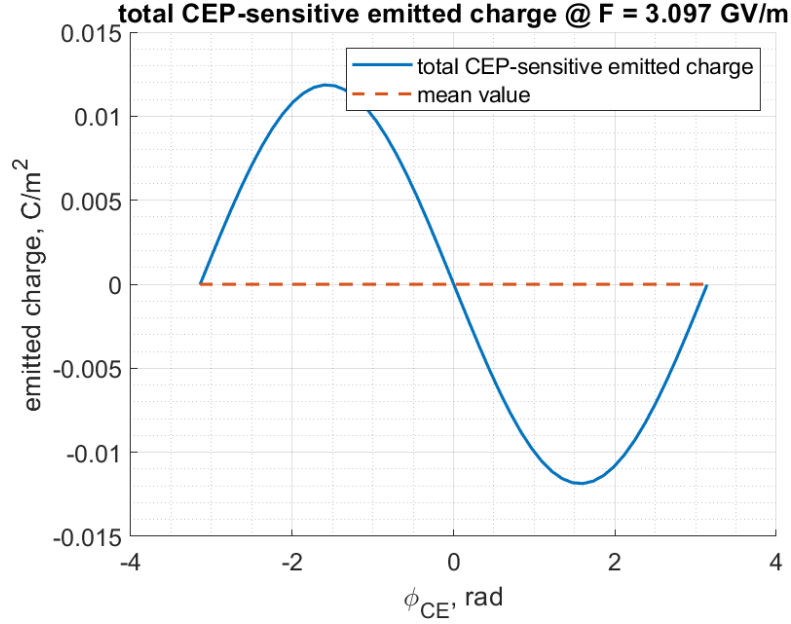


Figure 3.68: Total emitted charge density as a function of CEP value of the input pulse.

$J_{0,detected}$.

From the data in Table 3.2, one can appreciate a slight increase in the CEP-dependent photo-emitted current density when going to tip 2 and 3. This is not the expected behaviour. Indeed, from Subsection 3.3.3 on losses, it was observed a linear power loss for subsequent antennas, so one would expect less current emission from the furthest antenna. Although this may look counter-intuitive, this behaviour can be explained by the phenomenon of vanishing points, that is illustrated in the paper in ref. [30]. It explains that "At a critical pulse energy, which we call a vanishing point, we observe a pronounced dip in the magnitude of the CEP-sensitive photocurrent accompanied by a sudden shift of π radians in the photocurrent phase. Analysis shows that this vanishing behaviour arises due to competition between sub-optical-cycle electron emission events from neighbouring optical half-cycles and that both the dip and phase shift are highly sensitive to the precise shape of the driving optical waveform at the surface of the emitter."². The dip shape can be seen in Figure 3.69.

In the device studied for this thesis project, indeed, at the 3 different antennas, a different pulse peak intensity impinges on the structure, due to losses along the

²from paper cited as ref. [30]

Antenna 1	values
$ J_{1,L} $	0.5971 pA/nm ²
$J_{0,L}$	2.441 pA/nm ²
$ J_{1,R} $	0.5965 pA/nm ²
$J_{0,R}$	-2.441 pA/nm ²
$ J_{1,L} /J_{0,L}$	0.0025
$ J_{1,R} /J_{0,R}$	0.0024
$ J_{cep} $	1.186 pA/nm ²
$J_{0,detected}$	-5×10^{-5} pA/nm ²
Antenna 2	values
$ J_{1,L} $	0.5933 pA/nm ²
$J_{0,L}$	1.502 pA/nm ²
$ J_{1,R} $	0.5932 pA/nm ²
$J_{0,R}$	-1.502 pA/nm ²
$ J_{1,L} /J_{0,L}$	0.0039
$ J_{1,R} /J_{0,R}$	0.0039
$ J_{cep} $	1.1865 pA/nm ²
$J_{0,detected}$	1.75×10^{-2} pA/nm ²
Antenna 3	values
$ J_{1,L} $	0.6329 pA/nm ²
$J_{0,L}$	1.175 pA/nm ²
$ J_{1,R} $	0.6323 pA/nm ²
$J_{0,R}$	-1.175 pA/nm ²
$ J_{1,L} /J_{0,L}$	0.0054
$ J_{1,R} /J_{0,R}$	0.0054
$ J_{cep} $	1.265 pA/nm ²
$J_{0,detected}$	2.41×10^{-2} pA/nm ²

Table 3.2: The quantities in the table are: CEP-sensitive charge density from left-side nanotriangles $|J_{1,L}|$, mean charge density from left-side nanotriangles $J_{0,L}$, CEP-sensitive charge density from right-side nanotriangles $|J_{1,R}|$, mean charge density from right-side nanotriangles $J_{0,R}$, CEP sensitivity for the left-side nanotriangle $|J_{1,L}|/J_{0,L}$, CEP sensitivity for the right-side nanotriangle $|J_{1,R}|/J_{0,R}$, total CEP-sensitive current density $|J_{cep}|$ and residual average total current density $J_{0,detected}$. These quantities are studied for all of the considered antennas.

waveguide. A different peak intensity value corresponds to a different position in the curve of the CEP-sensitive photocurrent in Figure 3.69. So, if the peak intensity at antenna number 1 is almost inside the dip, on its left-side, the peak

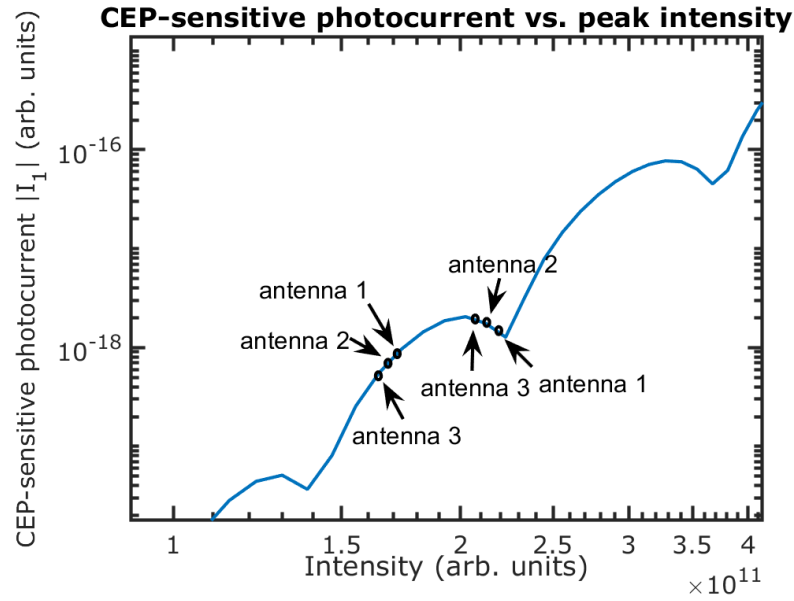


Figure 3.69: CEP-sensitive photocurrent as a function of the pulse peak intensity. The images focuses on the so-called "vanishing points".

intensities at antennas 2 and 3 will be located to its left, at a higher CEP-sensitive photocurrent value. The occurrence of this phenomenon can be shown by studying the same structure and enhanced pulses for different peak fields. The results are shown in Figure 3.70.

This figure shows that for every peak field value except for 3.097 GV/m and 3.51 GV/m the CEP-sensitive photocurrent decreases at further antennas. On the opposite, for 3.51 GV/m, it's probable that the peak intensity at antenna number 2 is very close to the vanishing point and the other two antennas peak intensities are on both sides of the dip, at a higher photocurrent value.

Emission surface area estimation

Once the CEP-sensitive photocurrent density is studied for the considered pulse, an emission surface area needs to be evaluated in order to estimate the total CEP-sensitive current emitted by the antennas. Indeed, the instantaneous emitted CEP-sensitive photocurrent was then calculated by integrating the current density J over the considered emission surface.

As previously stated, the emission surface area can be estimated by comparing the experimental results of the free-space bow-tie nanoantennas array, that are reported in the paper cited as ref. [23], with the simulated numerical results of the

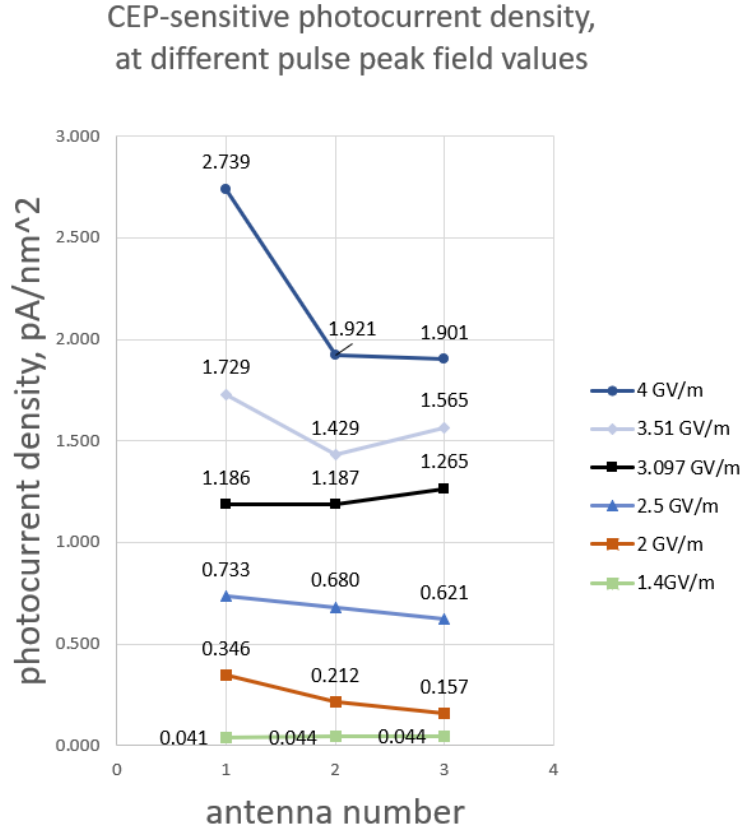


Figure 3.70: CEP-sensitive photocurrent density at the considered antennas, for different pulse peak field values.

same structure, that are developed by the authors of the paper and that are shared with the author of this thesis project. Indeed, in the paper is reported the measured value of CEP-sensitive photocurrent emitted as an average by each antenna. In parallel, the CEP-sensitive photo-emitted current density can be simulated. Hence, the emission surface area can be calculated by dividing the experimental current by the simulated current density. The experiments reported in paper ref. [23] study a free-space bow-tie nanoantennas array, as in Figure 3.71, whose nanoantennas and wires dimensions are the same as the one studied in this thesis Chapter. The incident pulse features are listed in Table 3.3.

These features lead to a measured CEP-sensitive photocurrent of ~ 1.3 pA per bow-tie antenna. Furthermore, the fact that the antenna interfaces with air/vacuum is taken into account by setting the energy barrier as $\phi = \phi_{Au} = 5.1eV$, which is the work function of gold. The simulated enhanced pulse, together with the emitted current density is shown in Figure 3.72, for an incident pulse with CEP =

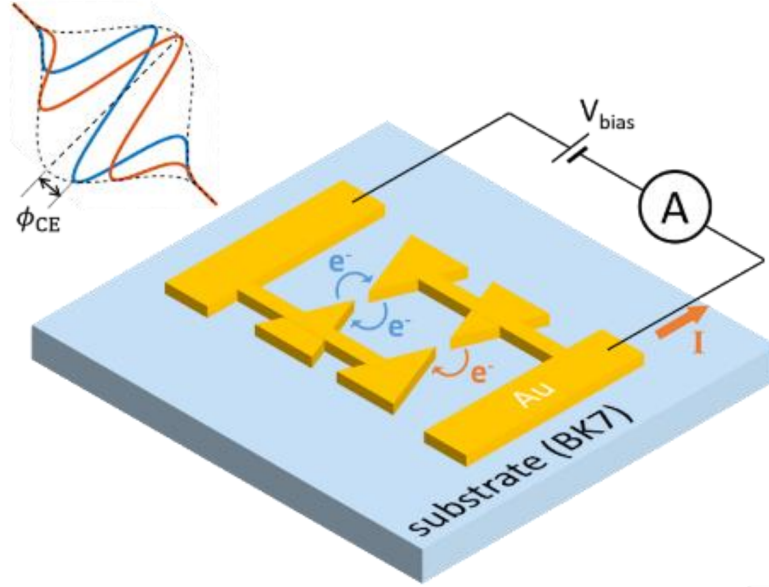


Figure 3.71: Representation of the devices studied in ref. [23] and of the CEP value for an ultrashort pulse.

Pulse features	Values
Pulse energy	190 pJ
Pulse duration	10 fs
Central frequency	1177 nm
Pulse peak power (190 pJ/10 fs)	19 kW
Pulse peak field	~ 1.4 GV/m

Table 3.3: Features of the incident field waveform for the fabricated devices reported in ref. [23].

0 rad.

The resulting values for CEP-sensitive current are listed in table 3.4.

By dividing the experimental CEP-sensitive photocurrent per bow-tie antenna by the simulated CEP-sensitive current density, the emission area is calculated as:

$$A_e = \frac{\sim 1.3 \text{ pA}}{|J_{cep}|} \approx 36 \text{ nm}^2.$$

This value is quite small, considering that the surface of the antenna tip is $20 \text{ nm} \cdot 5 \text{ nm} \cdot \pi \sim 300 \text{ nm}^2$. This is due to the fact that photoemission is a nonlinear process, both in space and in time, and hence is very confined in both directions. Given this value for the emission surface area, the total emitted CEP-sensitive photocurrent for the three antennas is listed in Table 3.5.

So, each bow-tie antenna can emit ~ 45 pA. This strong difference in emitted

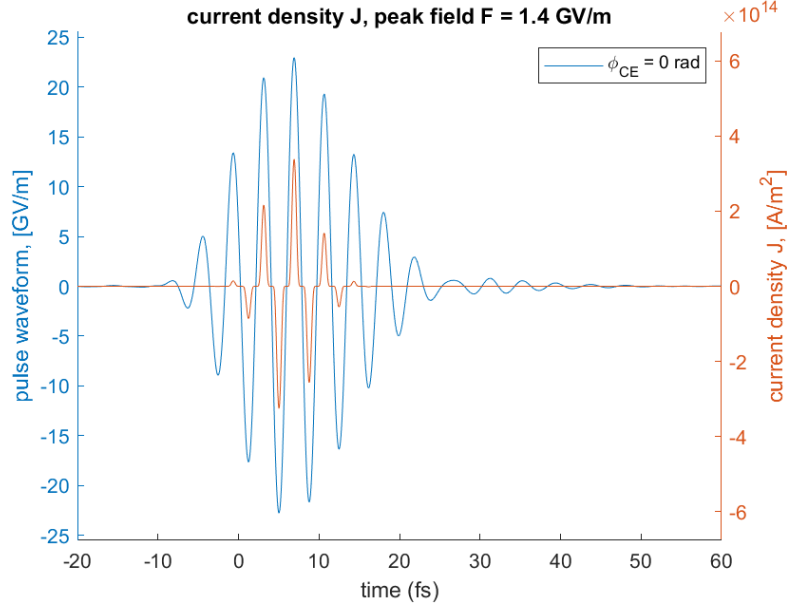


Figure 3.72: Field waveform of the enhanced pulse at the free-space bow-tie antennas and instantaneous emitted current density as a function of time. The CEP value for the input pulse is set to zero.

Antenna	values
$ J_{1,L} $	1.931×10^{-2} pA/nm ²
$J_{0,L}$	44.4 pA/nm ²
$ J_{1,R} $	1.933×10^{-2} pA/nm ²
$J_{0,R}$	-44.4 pA/nm ²
$ J_{1,L} /J_{0,L}$	0.00043
$ J_{1,R} /J_{0,R}$	0.00043
$ J_{cep} $	3.8×10^{-2} pA/nm ²
$J_{0,detected}$	35.48×10^{-5} pA/nm ²

Table 3.4: See Table 3.2 for the listed quantities definitions. These values are given by the free-space bow-tie nanoantennas.

photocurrent with respect to the fabricated free-space devices (which yielded 1.3 pA per bow-tie antenna) is given by the fact that the waveguide-integrated device has a higher CEP sensitivity. It is not a difference in impinging field values that causes a larger photoemission. Indeed, even though the peak field value of the input pulse for this device is twice as high as the one used for the fabricated device, the FE is lower, hence a similar peak field interacts with the antennas (as can be seen by comparing Figure 3.72 and Figure 3.66). On the other hand, the CEP

	$ I_{cep} $
Antenna 1	42.69 pA
Antenna 2	42.71 pA
Antenna 3	45.54 pA

Table 3.5: Total emitted CEP-sensitive photocurrent per each bow-tie antenna of the waveguide-integrated device.

sensitivity in the free-space experimental devices is $\sim 4 \times 10^{-4}$, whereas in the simulated waveguide-integrated device the CEP sensitivity is $\sim 4 \times 10^{-3}$, so ~ 10 times higher. This is given by the fact that the central frequencies of the used input pulses are different in the two cases. Indeed, in the fabricated free-space devices, a pulse with central wavelength $\lambda = 1177$ nm is used, whereas in the waveguide-integrated device a $\lambda = 1550$ nm central frequency pulse is used. A higher central frequency would lead to more optical cycles inside the 10 fs pulse, as it can be seen comparing Figure 3.72 and Figure 3.66. A lower number of optical cycles, leads to a higher CEP sensitivity. Indeed, a lower number of optical cycles means a lower number of side peaks around the central peak of the pulse. When studying the CEP sensitivity, the variation of the emitted photocurrent around a mean value as a function of CEP is analysed. If one looks at the contribution of the central peak of the pulse and of the side peaks separately, one can see that the central peak of the pulse has a maximum of photoemission at a certain value ϕ_0 of CEP and two minima at $\phi_0 \pm \pi$. On the other hand, its closest side peaks have the same behaviour, but shifted of π , so they create destructive interference with the contribution of the central peak. Since the contributions are not equal and the central peak generates more photocurrent than the side ones, the interference is not completely destructive and a CEP dependence can still be appreciated. Due to this process, the lower the number of side peaks, the higher the CEP sensitivity. In fact, if the pulse were a CW (Continuous Wave) sinusoidal wave, the contribution of each peak would be the same and no CEP dependence could be appreciated. Furthermore, a lower electrostatic barrier ϕ at the emission surface is considered for the waveguide-integrated device ($\phi = 4.2eV$) with respect to the free-space fabricated one ($\phi = 5.1eV$). As can be seen in Equation 3.2, a smaller barrier leads to a larger emitted photocurrent.

Pulse features analysis

In order to optimize the device behaviour, the device response needs to be studied under different pulse characteristics. In particular, the pulse duration and the pulse peak intensity are varied. The pulse duration is varied in a large range, [5, 34] fs and the CEP-sensitive current density and the CEP sensitivity are studied. Figures

3.73 and 3.74 show these features, respectively. Both figures show the values for all of the antennas along the waveguide.

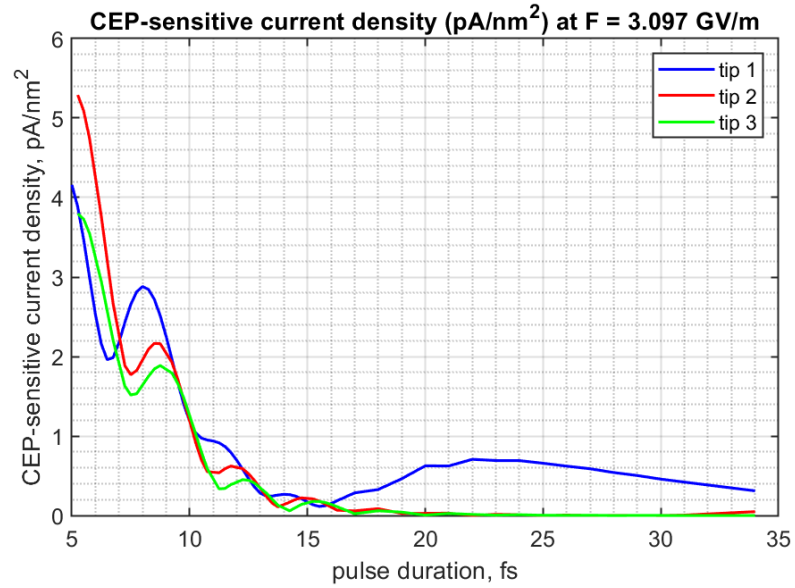


Figure 3.73: CEP-sensitive current density as a function of pulse duration.

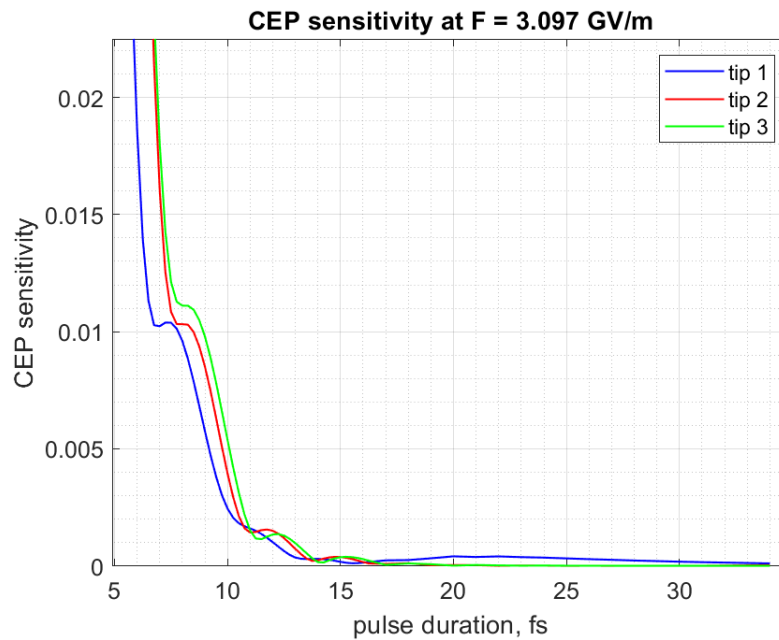


Figure 3.74: CEP sensitivity as a function of pulse duration.

When reducing the pulse duration, the number of optical cycles inside the pulse decreases so, as explained before, a shorter duration pulse leads to a higher CEP-sensitive photocurrent and a higher CEP sensitivity. A single cycle pulse would lead to a CEP sensitivity of 1; this trend can be seen in Figure 3.74.

Finally, the device is studied when varying the pulse peak field value for the incident pulse. Figures 3.75 and 3.76 show the CEP-sensitive current density and the CEP sensitivity, respectively. Both figures show the values for all of the antennas along the waveguide.

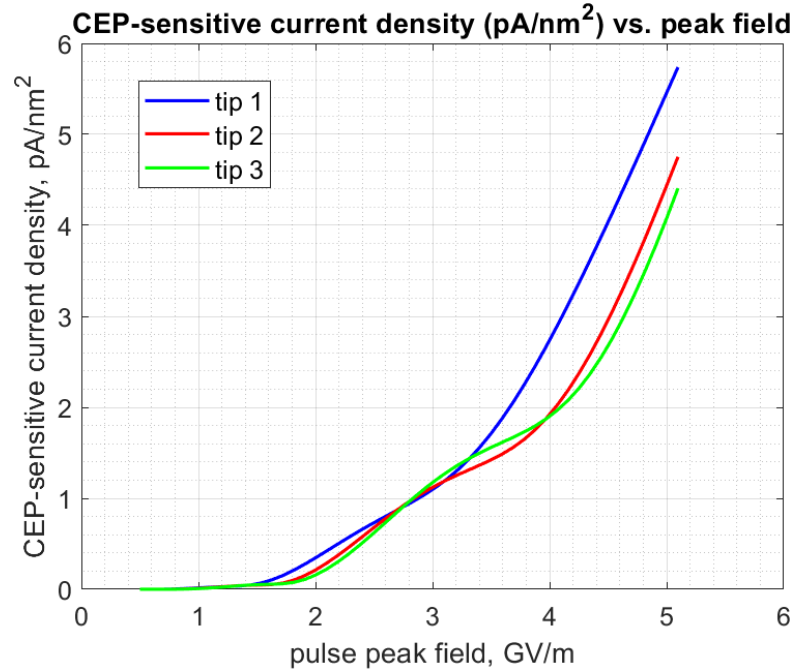


Figure 3.75: CEP-sensitive current density as a function of pulse peak field.

As one can see from these figures, the CEP-sensitive current increases at higher pulse peak intensities, but CEP sensitivity decreases. Hence, a trade-off is needed in order to obtain the highest CEP sensitivity but also a high enough CEP-sensitive photocurrent.

3.4 Conclusions

In this Chapter, the integration of plasmonic nanoantennas on a SiN waveguide for CEP detection is successfully achieved. In particular, the detector is optimized for evanescent coupling to waveguide modes of a ($0.8 \mu\text{m} \times 1 \mu\text{m}$) SiN core and a

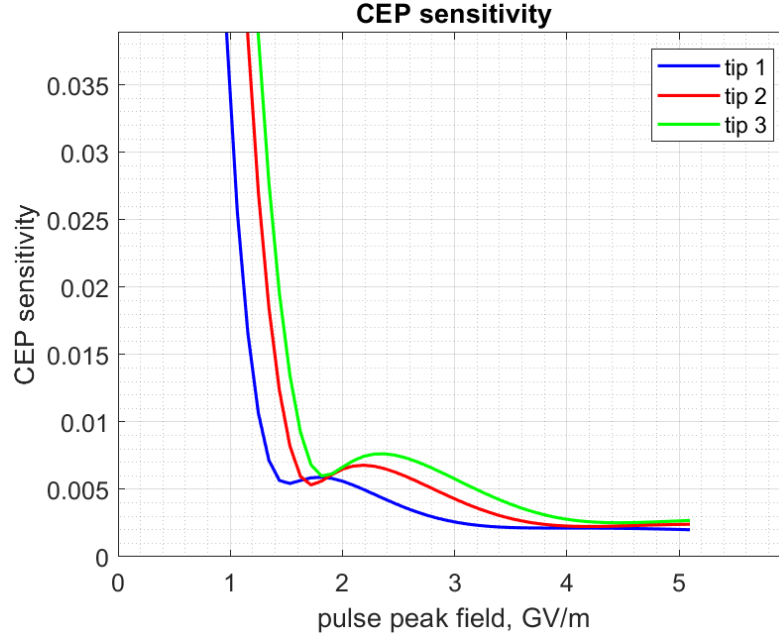


Figure 3.76: CEP sensitivity as a function of pulse peak field.

SiO₂ cladding waveguide. The CEP slippage for a waveform travelling through the waveguide is taken into account and the correct spacing among antennas along the waveguide, in order to detect the same CEP value at each antenna, for CEP-sensitive photocurrent generation, is found to be $\sim 4.5 \mu\text{m}$. The field distribution in the device is studied and the evanescent coupling to the waveguide is confirmed. Additionally, the formation of standing waves due to power reflection at the periodically-placed antennas is observed. A field enhancement up to ~ 11 can be detected at the antennas tips due to the excitation of plasmonic resonances, with a maximum at $\lambda \sim 1500 \text{ nm}$. A 10 fs FWHM pulse with central wavelength of 1550 nm and peak field of 3.1 GV/m is pumped in the waveguide and its transformation at the plasmonic antennas due to field enhancement is studied. The CEP value of the enhanced pulse is then measured at each antenna. The enhanced pulse possesses a peak field of $\sim 25 \text{ GV/m}$ and the CEP value is found to vary of $\sim 0.04\pi$ from one antenna to the next, given a $4.5 \mu\text{m}$ antennas spacing, showing that the chosen antennas spacing is close to the optimal value. Subsequently, the optical-field photocurrent that is generated by the interaction of the enhanced pulses with the nanoantennas material is estimated by a quasi-static Fowler-Nordheim (FN) emission model, for each antenna along the waveguide. An optical-field-driven CEP-sensitive photocurrent of $\sim 45 \text{ pA}$ per bow-tie nanoantenna and a CEP sensitivity of ~ 0.004 are obtained. Finally, a power loss of around 8.3% of the total input power is estimated at each antenna, due to power absorption at the

metal nanostructure and scattering at the antennas.

With respect to the free-space bow-tie nanoantennas array, studied in ref. [23], the device designed in this thesis has a $\sim 10\times$ higher CEP sensitivity and can emit a $\sim 30\times$ larger CEP-sensitive photocurrent. This is mainly due to different working frequency range and incident pulse features. Indeed, the waveguide-integrated device shows plasmonic resonance at $\lambda \sim 1500$ nm and the input pulse has central wavelength 1550 nm. This means that the pulse possesses a smaller number of optical cycles, which increases CEP sensitivity. Furthermore, this device can be implemented on photonics platforms. On the other hand, the free-space device is more compact than the waveguide-integrated one, because tens of bow-tie antennas can be illuminated simultaneously, with the same CEP value and the CEP slippage does not need to be taken into account. Furthermore, the waveguide-integrated device has larger losses due to power scattering at the antennas and the input power decreases rapidly along the waveguide, meaning that after 8 – 10 antennas no photoemitted signal can be appreciated. Because of this and for further reasons, some improvements can be made to improve the device performance:

- Alternative configurations for the collection wires can be useful to reduce the antennas spacing and hence the total length of the device, making it more compact. Namely, a connection from the sides of the antennas, instead of two wires running along the waveguide, can allow for this improvement. Indeed, the antennas can be placed, for example, at half the distance needed for CEP to perform a 2π shift (so the CEP only shifts of π from one antenna to the next), if the signal collector inverts the current obtained from the antennas that detects a π shift in CEP. Indeed, a π shift corresponds to a inversion of incident waveform field and hence to current being emitted in the opposite direction. Thus, the antennas can be placed at a fraction of the spacing needed for a complete 2π shift in CEP, if the signal collector is designed accordingly. This increases majorly the device integration. The same can be done with vertical vias that penetrate the cladding from the top, in order to reach for the antennas and collect the emitted signal.
- Further studies are needed in order to design the optimal antennas disposition in order to collect enough CEP-sensitive photocurrent for shot-to-shot CEP tagging. Indeed, in the studied disposition, the waveform undergoes a $\sim 8\%$ power loss at each antenna. This means that in 10 – 12 antennas, the optical signal is lost to power absorption and scattering. This number of antennas may not be able to generate the required CEP-sensitive signal, so different dispositions may have to be considered. Possible dispositions are:

- If the field waveform is strong enough, the signal power can be split in several waveguides with ~ 10 antennas each.
- Two or more antennas can be placed parallel to each other at the distance along the waveguide where CEP performs a 2π shift. This would increase the emitted photocurrent, but may also increase losses due to power absorption and scattering.
- In the current configuration, the antennas are coupled on top of the waveguide core. Different antennas coupling can be investigated, for example:
 - Butt coupling can be achieved if the antennas are placed in an array, as in the free-space application in ref. [23], and the waveguide that delivers the optical signal is coupled perpendicularly to the array plane.
 - MIM configuration can be utilized. Indeed, if on top of the waveguide core, perpendicularly to it, is placed a multi-layered material strip (Au, insulator, Au) and the insulator layer is a couple nm thick, field enhancement at the Au lower layer can lead to electron tunnelling to the upper Au layer through the insulator.
 - Finally, a slot configuration can be achieved if two Au nanowires are placed on top of the waveguide, both parallel to it. Field enhancement can lead photoemission from one wire to the other.
- Finally, in the current configuration, the antennas are immersed in SiO_2 . This is not ideal for electron transmission from one tip to the other, because there's a non negligible probability of scattering with the dielectric material atoms during transfer. This can be solved by studying the same bow-tie nanoantennas on top of the waveguide core, but removing the higher portion of the cladding that covers the antennas and study this device in air or in vacuum.

These are some of the possible improvements for the device.

Concluding, this on-chip waveguide-integrated solid state detector can be used for time-domain CEP detection in ambient conditions. It allows for a deeper understanding of strong-field light-matter interactions, for precise attosecond metrology and microscopy, for CEO stabilization for frequency-comb optical sources, for shot-to-shot CEP tagging and as a future application it can lead to ultrafast information processing with lightwave-based petahertz electronics.

Chapter 4

Conclusions

4.1 Summary and discussion

In this thesis project the operation of optical waveform detectors for field sampling and CEP detection is simulated. In particular, ultrafast nanoscale plasmonic electron emitting antennas in free-space are studied and the design and optimization of coupling to waveguide modes for potential operation within an integrated photonics platform is obtained. Throughout this thesis, two different applications of the nanoscale plasmonic antennas were analysed: field waveforms sampling and CEP detection.

As a first application, the frequency response of free-space plasmonic nanoantennas for field sampling is simulated with COMSOL Multiphysics. The electromagnetic response is important in order to quantitatively estimate the field behavior at the antennas tip. Indeed, in the field sampling process, it is fundamental to control the field value at the antennas tip, in order to study the possible emitted photocurrent.

The simulated device geometry was obtained by the SEM images of the fabricated devices. In particular, three slightly different geometries are considered and compared. The device shows the excitation of two main plasmonic resonances, called *tip-mode* and *wire-mode*, in the near IR region (at wavelengths in the range $[1, 1.3] \mu\text{m}$). The tip-mode resonance leads to a field enhancement up to ~ 16 at the antennas tips, for $\lambda \sim 1 \mu\text{m}$. Throughout the analysis, the simulated geometry is gradually adjusted in order to take into account the laser-induced reshaping phenomenon that the fabricated devices undergo during illumination. Because of this, the numerical results show a rather good matching with experimental ones for all three of the considered geometries and hence make the device suitable for

near-infrared waveforms field sampling. Furthermore, the studied device is designed in such a way that it can perform on-chip, low-energy, near-infrared, arbitrary waveforms field sampling in ambient conditions. This makes it competitive among other already available methods for field sampling.

As a second application of the nanoantennas, the integration of plasmonic nanoantennas on a SiN waveguide for CEP detection is successfully achieved. In particular, the detector is optimized for evanescent coupling to waveguide modes of a ($0.8\ \mu\text{m} \times 1\ \mu\text{m}$) SiN core and a SiO₂ cladding waveguide. In order to obtain a consistent CEP detection, the CEP slippage for a waveform travelling through a waveguide is taken into account and the correct spacing among antennas along the waveguide, in order to detect the same CEP value at each antenna, was found to be $\sim 4.5\ \mu\text{m}$ for the considered waveguide. The field distribution in the device is studied and the evanescent coupling to the waveguide is confirmed. A field enhancement up to ~ 11 can be detected at the antennas tips due to the excitation of plasmonic resonances, with a maximum at $\lambda \sim 1500\ \text{nm}$. A 10 fs FWHM pulse with central wavelength of 1550 nm and peak field of 3.1 GV/m is pumped in the waveguide and its transformation at the plasmonic antennas due to field enhancement is studied. The enhanced pulse possesses a peak field of $\sim 25\ \text{GV/m}$ and the CEP value is found to vary of $\sim 0.04\pi$ from one antenna to the next, given a $4.5\ \mu\text{m}$ antennas spacing, showing that the chosen antennas spacing is close to the optimal value. Subsequently, the optical-field photocurrent that is generated by the interaction of the enhanced pulses with the nanoantennas material is estimated by a quasi-static Fowler-Nordheim (FN) emission model, for each antenna along the waveguide. An optical-field-driven CEP-sensitive photocurrent of $\sim 45\ \text{pA}$ per bow-tie nanoantenna and a CEP sensitivity of ~ 0.004 are obtained. Finally, a power loss of around 8.3% of the total input power is estimated at each antenna, due to power absorption at the metal nanostructure and scattering at the antennas.

These features make the device suitable for time-domain CEP detection. Furthermore, the device is on-chip, waveguide-integrated, solid state and working in ambient conditions. This makes it competitive among other already available methods for CEP detection. In particular, the waveguide integration feature is important since pulse sources are going towards being completely integrated and optical signals are mainly delivered by waveguides, so the device is appropriate for potential operation within integrated photonics platforms.

Concluding, the considered plasmonic nanoantennas can be a support for the development of ultrafast technologies in several fields. In particular in the fields of time-domain spectroscopy, attosecond metrology and microscopy, frequency-comb optical sources, frequency synthesis and attosecond pulse generation. They can

also help deepen the knowledge of strong-field light-matter interaction and in the future can lead to lightwave-based petahertz electronics.

4.2 Future work

Further work is needed in order to better characterize the device and to make the devices more efficient, reliable and possibly more compact. In particular, for the waveguide-integrated bow-tie nanoantennas:

- Alternative configurations for the collection wires can be useful to reduce the antennas spacing and hence the total length of the device, making it more compact. Namely, a connection from the sides of the antennas, instead of two wires running along the waveguide, can allow for this improvement. Indeed, the antennas can be placed, for example, at half the distance needed for CEP to perform a 2π shift (so the CEP only shifts of π from one antenna to the next), if the signal collector inverts the current obtained from the antennas that detects a π shift in CEP. Indeed, a π shift corresponds to a inversion of incident waveform field and hence to current being emitted in the opposite direction. Thus, the antennas can be placed at a fraction of the spacing needed for a complete 2π shift in CEP, if the signal collector is designed accordingly. This increases majorly the device integration. The same can be done with vertical vias that penetrate the cladding from the top, in order to reach for the antennas and collect the emitted signal.
- Further studies are needed in order to design the optimal antennas disposition in order to collect enough CEP-sensitive photocurrent for shot-to-shot CEP tagging. Indeed, in the studied disposition, the waveform undergoes a $\sim 8\%$ power loss at each antenna. This means that in 10 – 12 antennas, the optical signal is lost to power absorption and scattering. This number of antennas may not be able to generate the required CEP-sensitive signal, so different dispositions may have to be considered. Possible dispositions are:
 - If the field waveform is strong enough, the signal power can be split in several waveguides with ~ 10 antennas each.
 - Two or more antennas can be placed parallel to each other at the distance along the waveguide where CEP performs a 2π shift. This would increase the emitted photocurrent, but may also increase losses due to power absorption and scattering.
- In the current configuration, the antennas are coupled on top of the waveguide core. Different antennas coupling can be investigated, for example:

- Butt coupling can be achieved if the antennas are placed in an array, as in the free-space application in ref. [23], and the waveguide that delivers the optical signal is coupled perpendicularly to the array plane.
- MIM configuration can be utilized. Indeed, if on top of the waveguide core, perpendicularly to it, is placed a multi-layered material strip (Au, insulator, Au) and the insulator layer is a couple nm thick, field enhancement at the Au lower layer can lead to electron tunnelling to the upper Au layer through the insulator.
- Finally, a slot configuration can be achieved if two Au nanowires are placed on top of the waveguide, both parallel to it. Field enhancement can lead photoemission from one wire to the other.
- Finally, in the current configuration, the antennas are immersed in SiO₂. This is not ideal for electron transmission from one tip to the other, because there's a non negligible probability of scattering with the dielectric material atoms during transfer. This can be solved by studying the same bow-tie nanoantennas on top of the waveguide core, but removing the higher portion of the cladding that covers the antennas and study this device in air or in vacuum.

Appendix A

Scripts

MATLAB Script: "pulsefilter.m"

```
1 function [Etenhance Atenhance f Eenhanceshift] = pulsefilter(t, E,  
    FEname)  
2 % This function takes an input pulse electric field waveform, and  
    produces  
3 % the electric field waveform, the envelope, the frequency vector,  
    and the  
4 % frequency-domain complex electric field, after enhancement induced  
    by a  
5 % nanostructure simulated in COMSOL.  
6 %  
7 %  
8 % Inputs:  
9 %     t —> time vector of the input pulse (requires uniform spacing)  
10 %     E —> input pulse electric field waveform  
11 %     FEname —> filename of field enhancement csv file exported from  
12 %               COMSOL  
13 %  
14 % Outputs:  
15 %     Etenhance —> output pulse electric field waveform after field  
16 %                 enhancement  
17 %     Atenhance —> output pulse envelope  
18 %     f —> frequency vector for frequency domain response, positive  
19 %         [Hz]  
20 %     Eenhanceshift —> complex electric field in frequency domain (  
21 %                     to get  
22 %                     the correct spectral phase, the time domain  
23 %                     waveform is shifted, so that time t = 0  
24 %                     corresponds to the envelope peak and is at  
25 %                     the  
26 %                     start of the time vector)
```

```

24 %
25 % Developed by: Yujia Yang, May 2020
26 %
27 % How to cite: please cite the following papers in any published work
    for
28 %           which you used this function or a modified version of
    it .
29 %
30 % (1)   Yang, Y.; Turchetti, M.; Vasireddy, P.; Putnam, W. P.;
    Karnbach,
31 % O.; Nardi, A.; Kärtner, F. X.; Berggren, K. K.; Keathley, P. D.
    Light
32 % Phase Detection with On-Chip Petahertz Electronic Networks.
33 % arXiv:1912.07130 [physics] 2019.
34 %
35 % (2)   Keathley, P. D.; Putnam, W. P.; Vasireddy, P.; Hobbs, R. G.;
    Yang,
36 % Y.; Berggren, K. K.; Kärtner, F. X. Vanishing
37 % Carrier-Envelope-Phase-Sensitive Response in Optical-Field
    Photoemission
38 % from Plasmonic Nanoantennas. Nature Physics 2019, 15 (11), 1128
    1133 .
39 % https://doi.org/10.1038/s41567-019-0613-6.
40 %
41 % (3)   Putnam, W. P.; Hobbs, R. G.; Keathley, P. D.; Berggren, K. K
    .;
42 % Kärtner, F. X. Optical-Field-Controlled Photoemission from
    Plasmonic
43 % Nanoparticles. Nature Physics 2017, 13 (4), 335-339 .
44 % https://doi.org/10.1038/nphys3978.
45 %
46 %
47 %
48 %
49 L = length(t);           % Signal length
50 dt = t(2)-t(1);        % Time vector interval
51 Ts = dt;                % Sampling period
52 Fs = 1/Ts;              % Sampling frequency
53 dF = Fs/L;              % Frequency vector interval
54 f = (-Fs/2:dF:Fs/2-dF)'; % Frequency vector
55
56 %% Fourier transform
57 Ef = fft(E);            % Frequency domain electric field
58 Efshift = fftshift(Ef); % Shift zero frequency to center
59 fshift = (-Fs/2:dF:Fs/2-dF); % Shift zero frequency to center
60
61 %% Import field enhancement from tabulated data exported from COMSOL
62 FE = csvread(FEname,5,0); % Field enhancement exported from
    COMSOL;

```

```

63                                     % data starting from row 5; this line
    of
64                                     % code can be changed depending on
    the data
65                                     % file format
66 w1 = FE(:,1);                        % COMSOL wavelength
67 freq = FE(:,2);                      % COMSOL frequency
68 FEmag = FE(:,3);                     % COMSOL field enhancement magnitude
69 FEphase = FE(:,4);                  % COMSOL field enhancement phase
70 field = FEmag.*exp(1i*FEphase);      % COMSOL complex field enhancement
71 % adding negative frequency part
72 freq2 = -flip(freq);
73 field2 = flip(conj(field));
74 % extrapolation using the grid defined by the frequency vector
75 fieldex1 = interp1(freq, field, fshift, 'linear',0); % linear
    interpolation
76                                     % and
    extrapolation,
77                                     % field
    enhancement is
78                                     % 0 for frequency
79                                     % outside the
    COMSOL
80                                     % simulated
    frequency
81                                     % band
82 fieldex2 = interp1(freq2, field2, fshift, 'linear',0);
83 fieldex = fieldex1 + fieldex2;
84
85 %% Filter with the field enhancement
86 Efenhance = Efshift.*fieldex; % Field with enhancement in frequency
    domain
87
88 %% Inverse Fourier transform
89 Etenhance = ifft(fftshift(Efenhance)); % Field with enhancement
    in
90                                     % time domain
91
92 Etenhance = real(Etenhance);          % Remove the tiny
    imaginary part
93                                     % caused by numerical
    artifacts
94
95 %% Pulse envelope using single-sided Fourier transform
96 Efshift_singleside = Efshift .* (fshift >= 0) * 2;
97 Efenhance_singleside = Efshift_singleside .* fieldex1;
98 Etenhance_singleside = ifft(fftshift(Efenhance_singleside));
99 Atenhance = abs(Etenhance_singleside);
100

```

```
101 %% Spectral response in frequency domain (positive and negative
    frequency)
102 [Amax, Amaxind] = max(Atenhance); % Find max and argmax of
    envelope
103 Etenhanceshift = circshift(Etenhance,-Amaxind); % Shift time-domain
104 % waveform to get
    the
105 % correct spectral
    phase
106 Efenhanceshift = fftshift(fft(Etenhanceshift));
107 f = fshift;
```

Bibliography

- [1] Ioachim Pupeza et al. «Field-resolved infrared spectroscopy of biological systems». In: *Nature* 577.7788 (2020) (cit. on pp. 1, 10).
- [2] Péter Dombi et al. «Strong-field nano-optics». In: *Rev. Mod. Phys.* 92.2 (2020) (cit. on pp. 1, 10).
- [3] S. B. Park, K. Kim, W. Cho, S. I. Hwang, I. Ivanov, C. H. Nam, and K. T. Kim. «Direct sampling of a light wave in air». In: *Optica* 5.402 (2018) (cit. on pp. 1, 10).
- [4] Wosik Cho, Sung In Hwang, Chang Hee Nam, Mina R. Bionta, Philippe Lassonde, Bruno E. Schmidt, Heide Ibrahim, François Légaré, and Kyung Taec Kim. «Temporal characterization of femtosecond laser pulses using tunneling ionization in the UV, visible, and mid-IR ranges». In: *Sci. Rep.* 9.1 (2019) (cit. on pp. 1, 10).
- [5] J. Itatani, F. Quéré, G. L. Yudin, M. Yu. Ivanov, F. Krausz, and P. B. Corkum. «Attosecond Streak Camera». In: *Phys. Rev. Lett.* 88.17 (2002) (cit. on pp. 1, 10).
- [6] Kienberger R et al. «Atomic transient recorder». In: *Phys. Rev. Lett.* 427.6977 (2004) (cit. on pp. 1, 10).
- [7] Sansone G et al. «Isolated single-cycle attosecond pulses». In: *Science* 314.5798 (2006) (cit. on pp. 1, 10).
- [8] A.L. Gaeta, M. Lipson, and T.J. Kippenberg. «Photonic-chip-based frequency combs». In: *Nature Photon.* 13 (2019), pp. 158–169 (cit. on pp. 2, 47).
- [9] J. Ye, L.S. Ma, T. Daly, and J. L. Hall. «Highly selective terahertz optical frequency comb generator». In: *Opt. Lett.* 22 (1997), pp. 301–303 (cit. on pp. 2, 47).
- [10] David J. Jones, Scott A. Diddams, Jinendra K. Ranka, Andrew Stentz, Robert S. Windeler, John L. Hall, and Steven T. Cundiff. «Carrier-envelope phase control of femtosecond mode-locked lasers and direct optical frequency synthesis». In: *Science* 288 (2000), pp. 635–639 (cit. on pp. 2, 47).

-
- [11] I. P. Christov, M. M. Murnane, and H. C. Kapteyn. «High-harmonic generation of attosecond pulses in the “single-cycle” regime.» In: *Phys. Rev. Lett.* 78.1251 (1997) (cit. on pp. 2, 47).
- [12] J. Schoetz, Z. Wang, E. Pisanty, M. Lewenstein, M. F. Kling, and M. F. Ciappina. «Perspective on Petahertz Electronics and Attosecond Nanoscopy». In: *ACS Photonics* 12 (2019), pp. 3057–3069 (cit. on pp. 2, 47).
- [13] A. Ryabov and P. Baum. «Electron microscopy of electromagnetic waveforms». In: *Science* 353.6297 (2016) (cit. on pp. 2, 47).
- [14] K. E. Priebe, C. Rathje, S. V. Yalunin, T. Hohage, A. Feist, S. Schafer, and C. Ropers. «Attosecond electron pulse trains and quantum state reconstruction in ultrafast transmission electron microscopy». In: *Nat. Photonics* 11 (2017), pp. 793–797 (cit. on pp. 2, 47).
- [15] Th. Udem, J. Reichert, R. Holzwarth, and T. W. Hänsch. «Absolute optical frequency measurement of the cesium D_1 line with a mode-locked laser.» In: *Phys. Rev. Lett.* 82.18 (1999) (cit. on pp. 2, 47).
- [16] H.R. Telle, G. Steinmeyer, A.E. Dunlop, J. Stenger, D.H. Sutter, and U. Keller. «Carrier-envelope offset phase control: A novel concept for absolute optical frequency measurement and ultrashort pulse generation». In: *Appl. Phys. B* 69 (1999), pp. 327–332 (cit. on pp. 2, 47).
- [17] X. Ren et al. «Single-shot carrier-envelope-phase tagging using an f-2f interferometer and a phase meter: a comparison.» In: *J. Opt.* 19.12 (2017) (cit. on pp. 2, 47).
- [18] T. Wittmann, B. Horvath, W. Helml, M. G. Schätzel, X. Gu, A. L. Cavalieri, G. G. Paulus, and R. Kienberger. «Single-shot carrier-envelope phase measurement of fewcycle laser pulses.» In: *Nat. Phys.* 5 (2009), pp. 357–362 (cit. on pp. 2, 47).
- [19] G. G. Paulus, F. Lindner, H. Walther, A. Baltuška, E. Goulielmakis, M. Lezius, and F. Krausz. «Measurement of the phase of few-cycle laser pulses». In: *Phys. Rev. Lett.* 91.253004 (2003) (cit. on pp. 2, 47).
- [20] M. Kubullek et al. «Single-shot carrier-envelope-phase measurement in ambient air». In: *Optica* 7.1 (2020) (cit. on pp. 2, 47).
- [21] T. Rybka, M. Ludwig, M. F. Schmalz, V. Knittel, D. Brida, and A. Leitenstorfer. «Sub-cycle optical phase control of nanotunnelling in the single-electron regime». In: *Nature Photon* 10.667–670 (2016) (cit. on pp. 2, 48).
- [22] W. P. Putnam, R. G. Hobbs, P. D. Keathley, K. K. Berggren, and F. X. Kärtner. «Optical-field-controlled photoemission from plasmonic nanoparticles». In: *Nat. Phys.* 13 (2017), pp. 335–339 (cit. on pp. 2, 5, 48).

- [23] Y. Yang, M. Turchetti, P. Vasireddy, W. P. Putnam, O. Karnbach, A. Nardi, F. X. Kärtner, K. K. Berggren, and P. D. Keathley. «Light phase detection with on-chip petahertz electronic networks». In: *Nat. Commun.* 11.3407 (2020) (cit. on pp. 2, 3, 5, 13, 23, 28, 32, 48, 56, 82, 83, 88–90, 96, 97, 101).
- [24] Mina R. Bionta, Felix Ritzkowsky, Marco Turchetti, Yujia Yang, Dario Cattozzo Mor, William P. Putnam, Franz X. Kärtner, Karl K. Berggren, and Phillip D. Keathley. *On-chip sampling of optical fields with attosecond resolution*. 2020. arXiv: 2009.06045 [physics.optics] (cit. on pp. 3, 10–14, 40).
- [25] M. Grishin. *Advances in Solid State Lasers. Development and Applications*. London, UK: IntechOpen, 2010 (cit. on p. 4).
- [26] Stephan A. Maier. *Plasmonics: Fundamentals and Applications*. New York, NY: Springer Science + Business Media LLC, 2007 (cit. on p. 5).
- [27] Z. Liang, J. Sun, Y. Jiang, L. Jiang, and X. Chen. «Plasmonic Enhanced Optoelectronic Devices». In: *Plasmonics* 9.859–866 (2014) (cit. on p. 6).
- [28] V. Giannini, A. I. Fernández-Domínguez, S. C. Heck, and S. A. Maier. «Plasmonic Nanoantennas: Fundamentals and Their Use in Controlling the Radiative Properties of Nanoemitters». In: *Chem. Rev.* 111.6 (2011) (cit. on p. 5).
- [29] P. Biagioni, J.-S. Huang, and B. Hecht. «Nanoantennas for visible and infrared radiation». In: *Reports on Progress in Physics* 75.2 (2012) (cit. on p. 5).
- [30] P.D. Keathley, W.P. Putnam, P. Vasireddy, R. G. Hobbs, Y. Yang, K. K. Berggren, and F. X. Kärtner. «Vanishing carrier-envelope-phase-sensitive response in optical-field photoemission from plasmonic nanoantennas». In: *Nat. Phys.* 15 (2019), pp. 1128–1133 (cit. on pp. 5, 82, 86).
- [31] R. Bormann, M. Gulde, A. Weismann, S. V. Yalunin, and C Ropers. «Tip-enhanced strong-field photoemission». In: *Phys. Rev. Lett.* 105.147601 (2010) (cit. on p. 6).
- [32] M. Schenk, M. Krüger, and P. Hommelhoff. «Strong-field above-threshold photoemission from sharp metal tips.» In: *Phys. Rev. Lett.* 105.257601 (2010) (cit. on p. 7).
- [33] M. Krüger, M. Schenk, and P. Hommelhoff. «Attosecond control of electrons emitted from a nanoscale metal tip». In: *Phys. Rev. Lett.* 105.147601 (2010) (cit. on p. 7).
- [34] P. D. Keathley, A. Sell, W. P. Putnam, S. Guerrero, L. Velásquez-García, and F. X. Kärtner. «Strong-field photoemission from silicon field emitter arrays». In: *Annalen Der Physik* 525 (2012), pp. 144–150 (cit. on p. 7).

- [35] D. J. Park, B. Piglosiewicz, S. Schmidt, H. Kollmann, M. Mascheck, and C. Lienau. «Strong field acceleration and steering of ultrafast electron pulses from a sharp metallic nanotip». In: *Phys. Rev. Lett.* 109.244803 (2012) (cit. on p. 7).
- [36] B. Piglosiewicz, S. Schmidt, J. Vogelsang D. J. Park, P. Groß, C. Manzoni, P. Farinello, G. Cerullo, and C. Lienau. «Carrier-envelope phase effects on the strong-field photoemission of electrons from metallic nanostructures». In: *Nature Photon* 8 (2014), pp. 37–42 (cit. on p. 7).
- [37] M. E. Swanwick, P. D. Keathley, A. Fallahi, P. R. Krogen, G. Laurent, J. Moses, F. X. Kärtner, and L. F. Velásquez-García. «Nanostructured ultrafast silicon-tip optical field-emitter arrays». In: *Nano Lett.* 14.9 (2014) (cit. on p. 7).
- [38] R. H Fowler and L. Nordheim. «Electron emission in intense electric fields». In: *Proc. R. Soc. Lond.* 119.173-181 (1928) (cit. on p. 7).
- [39] R. G. Forbes. «Description of field emission current/voltage characteristics in terms of scaled barrier field values (f-values)». In: *Journal of Vacuum Science Technology B* 26.209 (2008) (cit. on pp. 7, 83).
- [40] E. W. Lim and R. Ismail. «Conduction Mechanism of Valence Change Resistive Switching Memory: A Survey». In: *Electronics* 4 (2015), pp. 586–613 (cit. on p. 7).
- [41] J.-W. Han, D.-I. Moon, and M. Meyyappan. «Nanoscale Vacuum Channel Transistor, Supporting Information». In: *Nano Lett.* 17.4 (2017) (cit. on p. 7).
- [42] K. Iizuka. *Elements of Photonics, Volume II: For Fiber and Integrated Optics*. Hoboken, NJ: John Wiley Sons, Inc., 2002 (cit. on p. 8).
- [43] P. B. Johnson and R. W. Christy. «Optical constants of the noble metals». In: *Phys. Rev. B* 6.4370 (1972) (cit. on pp. 13, 50).
- [44] A. A. Maradudin, I. Simonsen, J. Polanco, and R. M. Fitzgerald. «Rayleigh and Wood anomalies in the diffraction of light from a perfectly conducting reflection grating». In: *Journal of Optics* 18.2 (2016) (cit. on p. 30).
- [45] K. Iizuka. *Elements of Photonics, Volume I: In Free Space and Special Media*. Hoboken, NJ: John Wiley Sons, Inc., 2002 (cit. on p. 49).
- [46] David R. Carlson, Phillips Hutchison, Daniel D. Hickstein, and Scott B. Papp. «Generating few-cycle pulses with integrated nonlinear photonics». In: *Opt. Express* 27 (2019), pp. 37374–37382 (cit. on p. 49).
- [47] K. Luke, Y. Okawachi, M. R. E. Lamont, A. L. Gaeta, and M. Lipson. «Broadband mid-infrared frequency comb generation in a Si₃N₄ microresonator». In: *Opt. Lett.* 40.21 (2015) (cit. on p. 50).

- [48] I. H. Malitson. «Interspecimen comparison of the refractive index of fused silica». In: *J. Opt. Soc. Am.* 55.10 (1965) (cit. on p. 50).
- [49] C. Z. Tan. «Determination of refractive index of silica glass for infrared wavelengths by IR spectroscopy». In: *J. Non-Cryst. Solids* 223.1-2 (1998) (cit. on p. 50).
- [50] H. B. Michaelson. «The work function of the elements and its periodicity». In: *Journal of Applied Physics* 48.4729 (1977) (cit. on p. 82).
- [51] J. Robertson. «Band offsets, Schottky barrier heights, and their effects on electronic devices». In: *Journal of Vacuum Science Technology A* 31.050821 (2013) (cit. on p. 82).